Doctoral Dissertation
Doctoral Program in Environmental Engineering (29th cycle)

A novel approach to rainfall measuring: methodology, field test and

business opportunity

By

Alberto Croci
******

Supervisors
Prof. Francesco Laio, Supervisor

Doctoral Examination Committee:
Dr. Luca Brocca, Referee, CNR-IRPI Perugia
Dr. Francesco Viola, Referee, Università degli Studi di Cagliari
Prof. Enrica Caporali, Università degli Studi di Firenze
Dr. Davide De Luca, Università della Calabria
Prof. Stefano Ferraris, Università degli Studi di Torino

Politecnico di Torino
2017

Declaration

I hereby declare that, the contents and organization of this dissertation constitute my own original work and does not compromise in any way the rights of third parties, including those relating to the security of personal data.

<div align="right">

Alberto Croci

2017

</div>

* This dissertation is presented in partial fulfillment of the requirements for **Ph.D. degree** in the Graduate School of Politecnico di Torino (ScuDo).

Charles M. Schultz

...to my family...

Abstract

Being able to measure rainfall is crucial in everyday life. The more rainfall measures are accurate, spatially distributed and detailed in time, the more forecast models - be they meteorological or hydrological - can be accurate. Safety on travel networks could be increased by informing users about the nearby roads' conditions in real time. In the agricultural sector, being able to gain a detailed knowledge of rainfalls would allow for an optimal management of irrigation, nutrients and phytosanitary treatments. In the sport sector, a better measurement of rainfalls for outdoor events (e.g., motor, motorcycle or bike races) would increase athletes' safety.

Rain gauges are the most common and widely used tools for rainfall measurement. However, the existent monitoring networks still fail in providing accurate spatial representations of localized precipitation events due to the sparseness. This effect is magnified by the intrinsic nature of intense precipitation events, as they are naturally characterized by a great spatial and temporal variability.

Potentially, coupling at-ground measures (i.e., coming from pluviometric and disdrometric networks) with remote measurement (e.g., radars or meteorological satellites) could allow to describe the rainfall phenomena in a more continuous and spatially detailed way. However, this kind of approach requires that at-ground measurements are used to calibrate the remote sensors relationships, which leads us back to the dearth of ground networks diffusion. Hence the need to increase the

presence of ground measures, in order to gain a better description of the events, and to make a more productive use of the remote sensing technologies.

The ambitious aim of the methodology developed in this thesis is to repurpose other sensors already available at ground (e.g., surveillance cameras, webcams, smartphones, cars, etc.) into new source of rain rate measures widely distributed over space and time.

The technology, developed to function in daylight conditions, requires that the pictures collected during rainfall events are analyzed to identify and characterize each raindrop. The process leads to an instant measurement of the rain rate associated with the captured image. To improve the robustness of the measurement, we propose to elaborate a higher number of images within a predefined time span (i.e., 12 or more pictures per minute) and to provide an averaged measure over the observed time interval.

A schematic summary of how the method works for each acquired image is represented hereinafter :

1. background removal;
2. identification of the rain drops;
3. positioning of each drop in the control volume, by using the blur effect;
4. estimation of drops' diameters, under the hypothesis that each drop falls at its terminal velocity;
5. rain rate estimation, as the sum of the contributions of each drop.

Different techniques for background recognition, drops detection and selection and noise reduction were investigated. Each solution has been applied to the same images sample, in order to identify the combination producing accuracy in the rainfall estimate. The best performing procedure was then validated, by applying it to a wider sample of images. Such a sample was acquired by an experimental station installed on the roof of the Laboratory of Hydraulics of the Politecnico di Torino. The sample includes rainfall events which took place between May 15th, 2016 and February 15th, 2017. Seasonal variability allowed to record events characterized by different intensity in varied light conditions.

Moreover, the technology developed during this program of research was patented (2015) and represents the heart of WaterView, spinoff of the Politecnico di Torino founded in February 2015, which is currently in charge of the further development of this technology, its dissemination, and its commercial exploitation.

Contents

List of figures

List of tables

Chapter 1

Introduction

Since ancient times, precipitation measuring has always had a fundamental role in man life. In fact, levels of rivers, available water volumes, the flood discharge and lean, and the levels of natural reservoirs and groundwater depend on it.

In addition to the just mentioned aspects, precipitation measurement allows a proper management by the Civil Defence for the prevention and protection from landslides and flash flooding.

Furthermore, it is closely linked to agriculture because the weather conditions and the quality of soil determine the type of crop, treatments, time of sowing and harvesting.

The most common measurement techniques (Strangeways, 2010, Sene, 2013) are to this day rain gauges, disdrometers, weather radars and satellites (the state of the art is briefly described in Chapter 2). These four instruments are complementary in many aspects; they provide information at different spatial and temporal scales; moreover, weather radar and satellite both need at ground measures from rain gauges and/or disdrometers.

Unfortunately, the actual quality of the rain gauge networks is, on a global scale, totally unsuitable to intercept and describe rainfall events (Tapiador et al., 2010).

To improve the spatial detail of at-ground precipitation patterns we propose a novel technique based on the quantitative detection of rain intensity from images,

i.e. from pictures taken in rainy conditions. The method, described in Chapter 3, is fully analytical and based on the fundamentals of camera optics.

A pioneer example of camera-based disdrometer is represented by the Illinois State Water Survey raindrop camera (Jones and Dean, 1953; Jones, 1992) which directly measures the dimensions of falling precipitation particles. Another experiment which uses three adjacent nearly collinear Hasselblad cameras with 60 mm film is the HYDROP experiment (Desaulniers-Soucy et al., 2001). This instrument simultaneously triggers the cameras to reconstruct the three-dimensional raindrop positions and size distributions using stereo-photography. All these experiment rely on the use of ad-hoc apparatus while we propose to use commercial low-cost cameras or webcams to retrieve rain rate measures.

The work presented in this thesis also tries to respond to one of the relevant research questions raised by the IAHS Scientific Decade 2013 – 2022 discussion forum (Montanari et al., 2013): "*How can we initiate the development of new measurement techniques?*" Few papers exist that share our objective of intensifying the spatial rain gauging density relying on unconventional monitoring methods. Cord and Aubert (2011) propose to exploit cars as moving rain gauges using wipers velocity as a proxy of rain intensity. Rabiei et al. (2013) present another interesting application towards the detection of rain through the use of in-vehicle sensors. Their results show that a high number of (possibly inaccurate) measures provide more reliable areal rainfall estimations than a lower number of (presumably precise) measurements.

We totally share this perspective and, to lower the costs of in-situ monitoring networks, we underline the necessity to resort to crowdsourcing (i.e. the practice of obtaining services by soliciting contributions from a large group of people). In this respect, the method we propose is prospectively applicable to crowdsourced pictures of rain (acquired with smartphone cameras and shared in real time) in an extensive way. Following the same trail - towards the collection of hydrologically relevant data from citizens - Overeem et al. (2013b) outline the possibility of crowdsourcing urban air temperatures from smartphone battery temperatures. Interesting perspectives are also provided by the use of digital cameras to retrieve snow cover characteristics (Paraika et al., 2012) and by the exploitation of cell phone signals to retrieve rainfall intensity (Messer et al., 2006; Leijnse et al., 2007; Overeem et al., 2011 and 2013a). The potential of all these methods is yet to be completely deployed. The rapid technological advancements in smartphone features and the massive penetration of smartphone technologies (in developing countries as well) are expected to draw tremendous benefit on the possible developments. In fact, the evolution in mobile phone and smartphone camera features (in terms of sensor size, number of pixels, focal length etc.) from the year

2000 (when the first mobile phone with a camera was commercialised) to date is glaring (see e.g., www.ericsson.com/mobility-report). Extrapolating this trend allows one to gain confidence in the possibility of effectively and extensively gauging rain with images gathered by smartphone cameras.

Based on this whole range of new opportunities we focused on two main topics:

- understand strengths and the weaknesses of traditional instruments which currently represent our benchmark to rain rate measurement;
- investigate the literature in the field of computer vision applied to rain removal, noise reduction and feature detection.

With regard to the first point, the greatest shortcoming of rain gauges is that, despite they represent the most common instrument and have been used for over a century, they are still characterized by inherent limitations and approximations in rain rate measurement. The main cause of these approximations is related to the dimensions of the rain gauge (that somehow also represent the overriding reason of its spreading). In scientific literature there are many published works that analyze the effects of the modest size of the sampling area ($A<0.05$ m^2) showing that two rain gauges in the same site do not produce the same precipitation measures due to the intrinsic variability of rain itself (Krajewski et al., 2003). The small size of the sampling area is the cause of an even more significant approximation in windy condition (Nešpor & Sevruk, 1999; Rodda and Dixon, 2012); condition that typically occurs in case of extreme and short-term events, which are particularly interesting for hydraulic engineers and are usually characterized by the presence of strong turbulence.
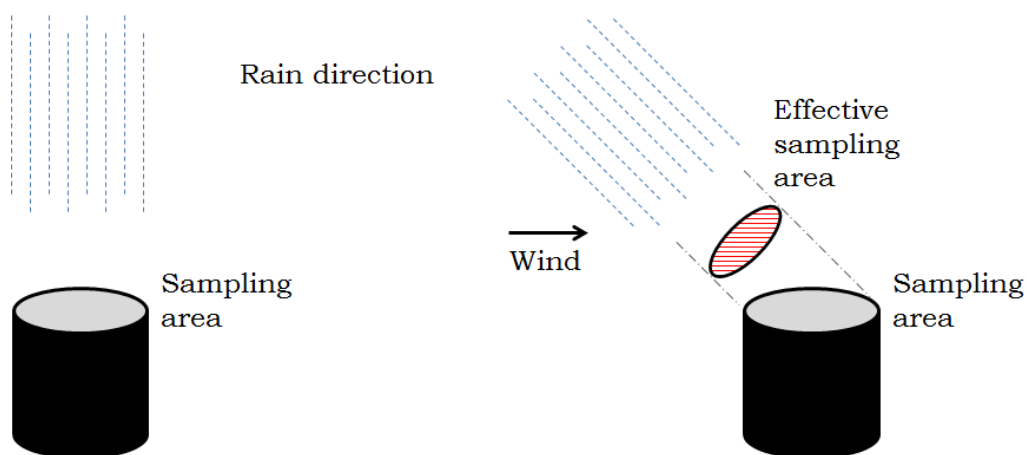
Figure 1.1 - Reduction of catchment area in windy conditions. In these case the effective sampling area is represented by the projection of the sampling area on a plane orthogonal to the falling direction of rain

Even considering negligible the turbulence effects (although this assumption is clearly not realistic), in windy condition there is another effect which contributes to amplify the measure inaccuracy. In these cases in fact the effective sampling area is represented by the projection of the catchment area un a plane orthogonal to the falling direction of rain (see Figure 1.1).

There are also several studies (Habib et al., 2001) that have correlated the accuracy of rain gauges to time scale (time window used for integration), bucket size and sampling resolution (that is correlated with the acquisition frequency). These works has shown that increasing the time scale leads to a better performance of the rain gauge. As said, time scale is strongly related to the capability of the instrument to intercept a sufficient amount of raindrops to describe the event; Figure 1.2(*a*) shows that this effect is much more evident in case of less intense rain rates but also affects the heavy rain events.
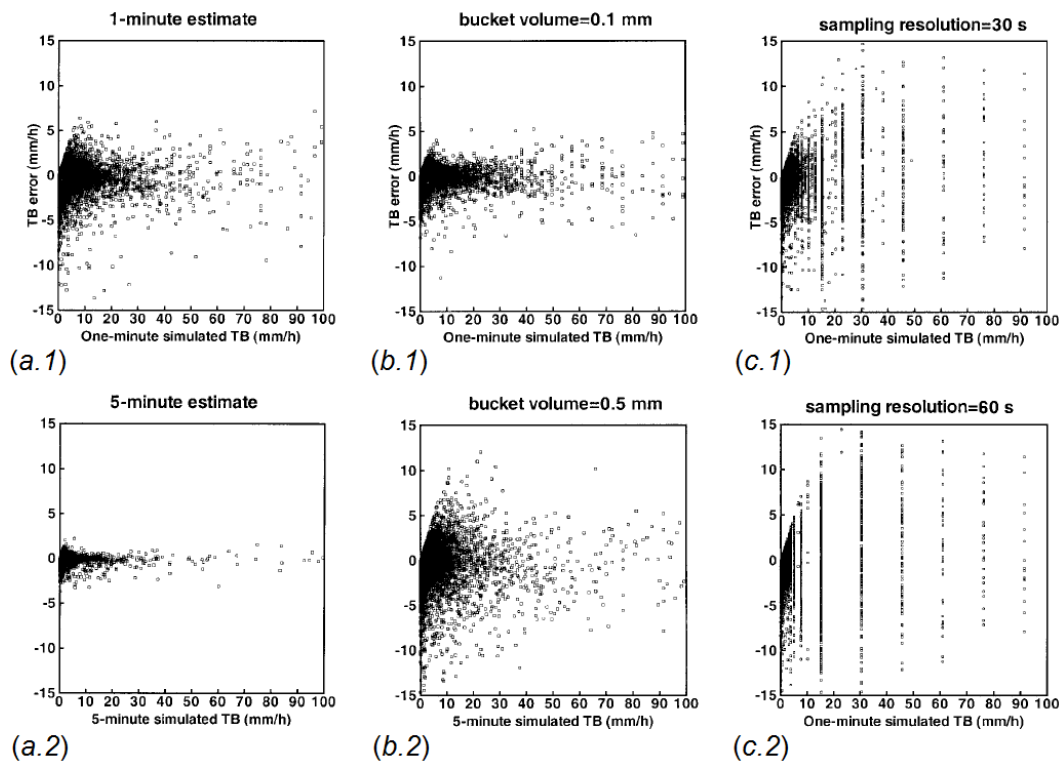
Figure 1.2 - Tipping-bucket error for two simulation: (*a*) 1 and 5 min time scales (5 s sampling resolution and bucket size of 0.254 mm); (*b*) 0.1 mm and 0.5 mm bucket sizes compared with 0.254 mm one; (*c*) 30 s and 60 s sampling resolutions (compared with 5 s resolution) (Habib et al., 2001)

Similarly, as shown in Figure 1.2(*b*), a smaller bucket size (in the same conditions of time scale and sampling resolution) produces the improving of the intensity estimation, due to its higher sensitivity to rain changes.

The last parameter considered is the sampling resolution. In many of the operational networks, the gauges usually operate at a very coarse sampling resolution. Sampling with higher rates would led to more expensive data acquisition systems and larger data storage requirements (Habib et al., 2001). Figure 1.2(c) shows the comparison between 5 s and 30 s of sampling resolution (*c*.1) and between 5 s and 60 s of sampling resolution (*c*.2). The errors in the rain intensity estimation increases for all the spanned intensities and, furthermore, the higher sampling resolutions give a less accurate description of the event.

A further aspect which must be taken into account is the procedure used, to date, to calibrate and determine the class of each rain gauge. According to World Meteorological Organization (WMO) the calibration is made by introducing in the rain gauge a known amount of water and verifying the correspondence between the expected number of oscillations of the bucket, obtained dividing the input volume by the bucket size, and the total number of oscillations counted at the end of the test. The difference between these quantities determines the class of accuracy of the instrument (WMO, Annex 1.D of Chapter 1, Part I, 2008). This procedure is strongly in favour of the pluviometer since it eliminates the most relevant causes of inaccuracy , i.e. the small size of the catchment area and the turbulence effects.

The problems described here do not affect only the rain gauges, but are also present for disdrometers (see Figure 1.3). These kind of instruments are characterized by an even smaller sampling area (sampling area<0.005 m^2) and need very high time scales to describe a rain event (Upton et al., 2008).
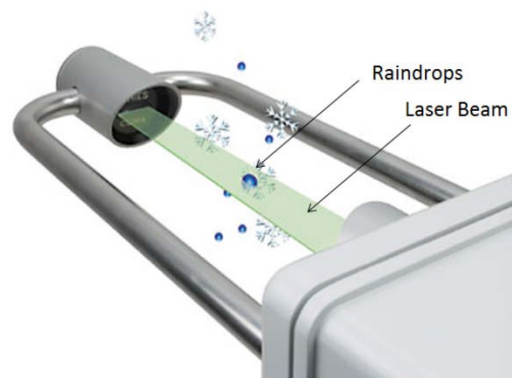
Figure 1.3 - Schematic of optical disdrometer (Kathiravelu et al., 2016)

From a instrumental point of view, these are the main reasons which led us to seek a new method to measure rain rate, but the essential inspiration, as said, came from studies about computer vision. In these works the main goal was to remove, or at least reduce, the noise in videos and photos caused by the presence of rain

and snow. In literature there are many scientific articles from research groups dealing with this issue by applying very different approaches. More or less sophisticated methods have been investigated in order to identify and remove rain signal in post processing, restoring the image in the areas characerized by the presence of raindrops (Garg and Nayar, 2007; Bossu et al., 2007). In other cases attempts have been made to correlate the rain visibility to the camera parameters set in the process of image/video acquisition. In this way it has been possible to determine (Garg and Nayar, 2007) the relations between rain visibility and the main camera parameters to properly set them causing a strong reduction, or complete removal, of noise. In Figure 1.4 is shown how raindrops visibility (*a*) decreases when exposure time increases, (*b*) increases with the F-Number rise, reaching saturation for the highest values of F-Number and (*c*) it has a minimum for near focus distances, a maximum for intermediate focus distances (which depends from the other acquisition parameters) and then it stabilized for the highest focus distances.
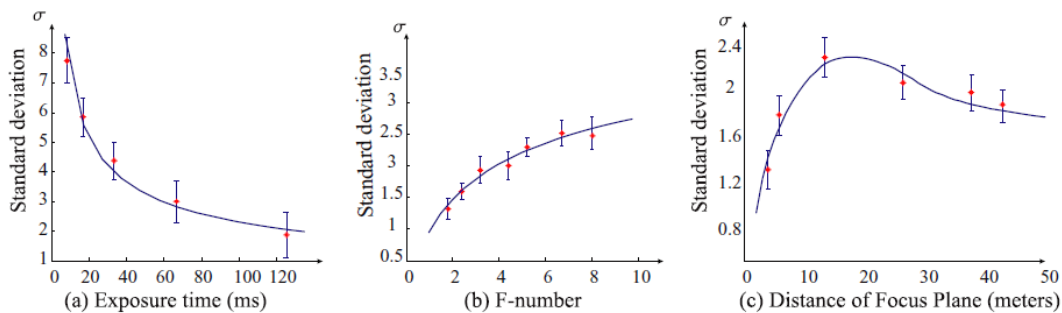
Figure 1.4 - Experimental verification of the analytical model that relates visibility of rain σ to camera parameters (Garg and Nayar, 2007). The solid curves show σ, the red marks show the mean values of the measured σ and the error bars show the uncertainty in measurement. (*a*) σ as a function of exposure time T. (*b*) The visibility dependence on aperture size (F-number). (*c*) Dependence of visibility on distance of the focus plane z_0

The knowledge of the existence of optimal settings of the camera parameters capable of reducing and minimizing rain visibility, has been a strong input in the present work. In fact, moving in the opposite direction we have been able to determine some ranges in the parameters to enhance raindrop visibility and make the drop detection easier (Allamano et al., 2015). These options are described in detail in Chapter 3.

Another important step to detect and select rain in an image is about the background subtraction. Always within computer vision there are many works, which are not strictly related to the rain removal/detection, about background subtraction methods. As for rain detection, these methods can be very different in terms of physical approach, computational burden, elaboration time etc., but the

main purpose is the creation of a reference image (background) to detect moving objects (Friedman and Russel, 1997; Stauffer and Grimson, 1999; Zivkovic and van der Heijden, 2006; Alawi et al., 2013). In this thesis we tested different background subtraction methods which are described in Chapter 3 and Chapter 4.

Chapter 2

State of the art

In Chapter 1 the rain gauge has been introduced as the fundamental means for measuring at-ground precipitation. The total number of gauges across the Earth ranges from a few thousand, which are available in near real time, to an estimated hundreds of thousands if amateur gauges are included. If we take all the Global Precipitation Climatology Centre available gauges (67000 accordingly to Schneider et al., 2014) and represent for each of them a 5 km radius surrounding region, less than 1% of the Earth's surface will be represented (Kidd et al., 2014). Note that a region of influence with a 5 km radius can be unrealistically large to describe the spatial variability of short-duration rainfall (Tapiador et al., 2010), while indeed the region of influence of rainfall increases for longer aggregation intervals (e.g., daily rainfall). Berne et al., 2004, report on the fact that *"hydrological applications for urban catchments of the order of 1000 ha require a temporal resolution of about 5 min and a spatial resolution of about 3 km. For urban catchments of the order of 100 ha, it becomes a resolution of about 3 min and 2 km, that common operational networks or radars cannot provide"*. In this respect, it is worth noting that investment in monitoring networks is generally decreasing, not only in the developing world, but also in developed countries (Harmanciogammalu et al., 2003; Lorentz and Kuntsmann, 2012).

To bridge the gap between the discrete information provided by the rain gauge network and the real spatial dynamics related to the precipitation fronts, one possibility is coupling remote (e.g., satellite and radar) precipitation measures with gauge precipitation observations. Since the operation requires working at the

interface between very different families of data, referred to various control volumes, the combination of the various signals may turn out to be less effective and more complicated than one would expect, in particular when short-duration rainfall is considered (e.g., AghaKouchak et al., 2010; Brocca et al., 2014).

2.1 RAIN GAUGE

The rain gauge is the fundamental means for measuring at-ground precipitation. Besides being used for specific applications (e.g., agricultural) even at an amateur level, it is an important part of a weather typecasting. Different type of rain gauges exist and are here described.

2.1.1 Manual rain gauge

The manual rain gauges require the presence of an operator for recording the measurement. It is estimated (Sevruk & Klemm, 1989) that more than 50 different types of manual rain gauges are currently in use. They generally are of cylindrical shape, with constant diameter, open at the top; the water is conveyed inside of an inner container, and it is manually measured with a graduated instrument. The operation is repeated at regular time intervals, typically daily.

2.1.2 Pluviometer of intensities

The pluviometer of intensities (or Jardi's pluviometer) is a tool that measures the average intensity of rainfall in a certain interval of time.

It consists of a rotating drum that rotates at a constant speed, dragging a graduate sheet of cardboard, which has the time at the abscissa while the y axis indicates the height of rainfall in mm of rain (see Figure 2.1). This height is recorded with a pen that moves vertically, driven by a buoy, marking on the paper the rainfall over the time (the cardboard sheet is usually daily).

While the rain falls the funnel collects the water into the container and raises the buoy; this mechanism makes the pen arm raising and marking the cardboard accordingly. If the rainfall is constant, the water level in the container remains the same and the pen draws a horizontal line, proportional to the actual rain rate. When the pen reaches the top edge of the recording paper, it means that the buoy is at its highest level leaving the tip of the conic needle in a position that uncovers the regulating hole and the instrument is recording the maximum intensity it is able to measure. If the rain suddenly decreases, emptying the container, a steep

slope line is recorded and if the rain stops it can reach the bottom of the cardboard.
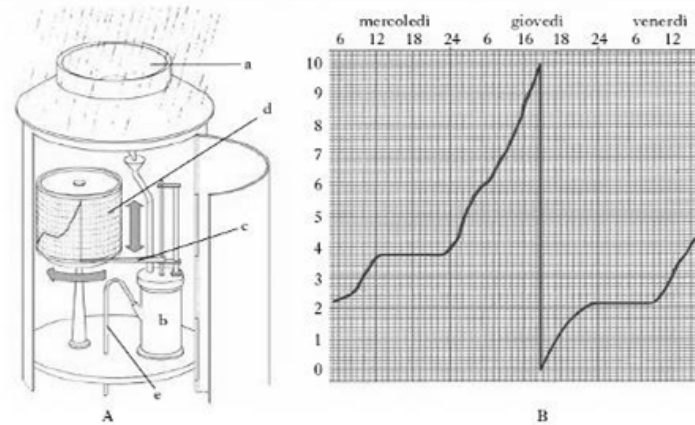
Figure 2.1 - Scheme of a pluviometer of intensities (A) and a possible trend of precipitation (B) (http://www.treccani.it/enciclopedia/pluviometria/)

2.1.3 The tipping bucket rain gauge

The tipping bucket rain gauge, Figure 2.2, consists of a funnel that collects the precipitation into a small bucket that can contain a calibrated amount of water (usually 0.1 mm or 0.2 mm). It is generally installed about 2 meters high above the ground to avoid any disturbances caused by the presence of nearby objects. Furthermore, for higher altitudes, the measure is undermined by the winds; the speed of the wind increases with altitude, and in windy conditions the water does not fall at right angles to the inlet surface. This is equivalent to using a smaller diameter mouth (see Figure 1.1), and leads to systematic underestimation.

Figure 2.2 - Internal trays of a Davis tipping bucket rain gauge

The tipping bucket rain gauge guarantees rather fast and accurate measures. The accuracy depends on the instrument calibration and rainfall intensity; in fact, it will underestimate the amount of the precipitation with increasing errors if the rainfall intensity increases, especially over 50 mm per hour (Humphrey et al., 1997). In fact, in case of very heavy rainfall events, tipping buckets tend to underestimate the amount of rainfall by 35%.

The tipping buckets rainfall estimation errors are related to (UK Environment Agency 2004):

- presence of the wind: 2-10%;
- evaporation: 0-4%;
- rain gauge mechanism: 2-7% (Adami and Da Deppo, 1986).

Even if this kind of instrument can record measures every few seconds, it is preferred to average the rainfall amount collected over a period of a minute to improve accuracy (Habib et al., 2001).

As said, the operating principle is very simple: raindrops are collected by the funnel and conveyed to the bucket (see Figure 2.3) so that the weight of the water inside the upper bucket makes it fall down and raises the other bucket in order to repeat the process. Every time the bucket oscillates, a magnet activates a Reed switch sending a signal to the datalogger. The datalogger memorizes the time of each pulse. Many different algorithms exist in literature to convert the above mentioned epochs in rain intensity and their accuracy strongly depends on the rain gauge settings (described in Chapter 1). As we saw, time scale, bucket size and sampling resolution play a significant role in determining the measure accuracy. For our purposes, we chose a very simple method (described in Section 5.2 and graphically in Figure 5.4) to determine rain rate with a 1 minute time scale
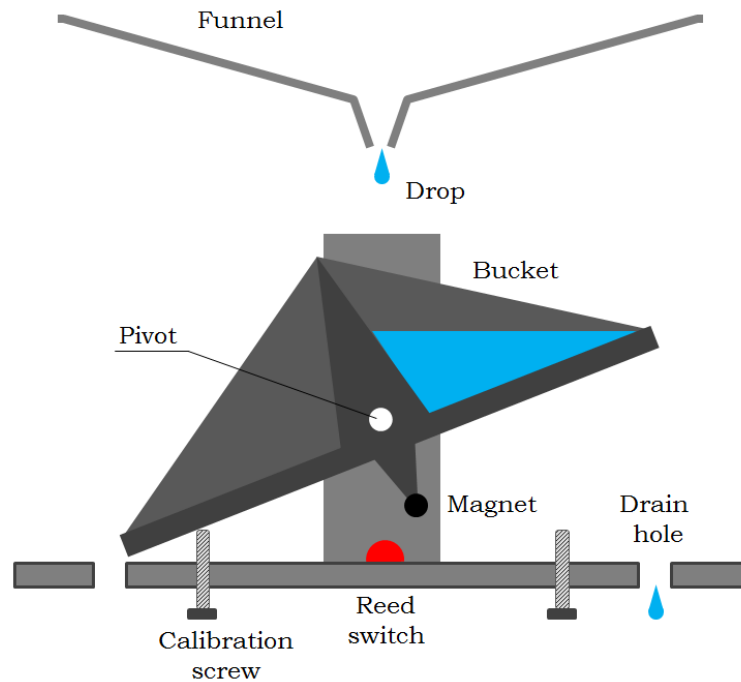
Figure 2.3 - Scheme of a tipping bucket rain gauge

2.1.4 Weighing precipitation gauge

A weighing-type precipitation gauge consists of a storage bin, which is weighed to record the mass. Certain models measure the mass using a pen on a rotating drum (see Figure 2.4), or by using a vibrating wire attached to a data logger. The advantages of this type of gauge over tipping buckets are that it does not underestimate intense rain, and it can measure other forms of precipitation, including hail and snow. These gauges are, however, more expensive and require more maintenance than tipping bucket gauges.
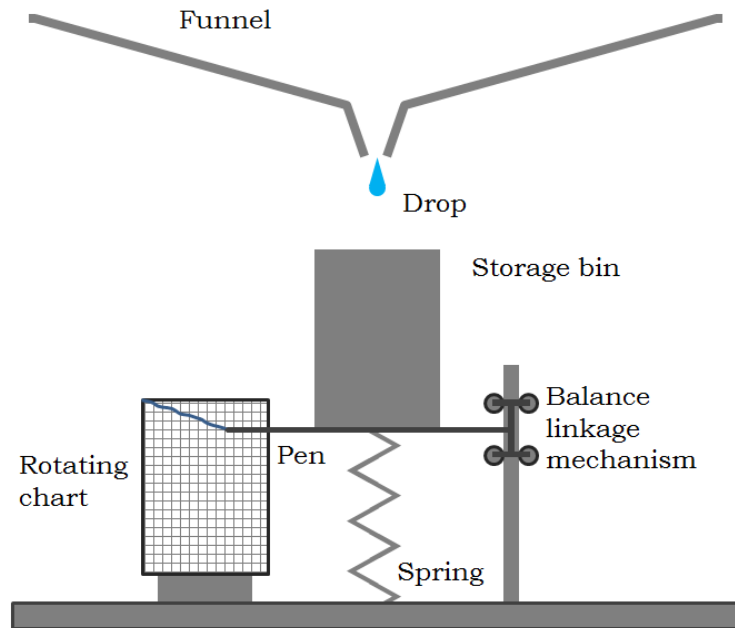
Figure 2.4 - Semplified scheme of a weighging rain gauge

As for tipping bucket gauges, the raindrops are collected by the funnel and conveyed to a storage bin. This bin is connected to the structure by means of a roller support that allows vertical movements and a spring which determines its displacements. While water level raises inside the bin, its weight increases leading to a lowering of the bin itself. This movement is automatically registered by a pen that marks on the graduate paper the rainfall over the time. Even though these kind of gauges are able to better describe rain events, their price and the required maintenance have restricted their spreading to research and monitoring centers.

The weighing-type recording gauge may also contain a device to measure the quantity of chemicals contained in the location's atmosphere. This is extremely helpful for scientists studying the effects of greenhouse gases released into the atmosphere and their effects on the levels of the acid rain. Some Automated Surface Observing System (ASOS) units use an automated weighing gauge called the AWPAG (All Weather Precipitation Accumulation Gauge).

2.2   DISDROMETER

Disdrometers are instruments that can measure the diameter and speed of raindrops. They can be divided into two groups according to the physical principle they are based on: optical and impact-type disdrometers.

2.2.1 Optical disdrometer

The PARSIVEL (PARticleSIzeVELocity) optical disdrometer uses a laser sensor to measure precipitation. The instrument is made up of a transmitter and a receiver placed opposite each other at a few tens of centimeters distance depending on the model. The transmitter unit generates a laser beam that is converted into electrical signal from the receiving unit (Figure 2.5) . The passage of a drop of water obscures a part of the laser beam causing a decrease in the energy read by the receiver dependent on the drop size. Analyzing the captured signal, depending on the difference between emitted energy and received energy, the instrument can define the diameter of the particle.

In addition, by measuring the particle permanence time within the laser beam, it is possible to determine the rate of fall.
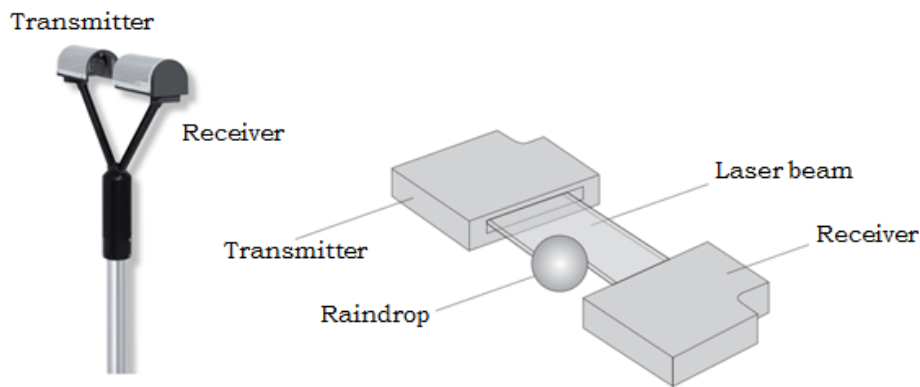
Figure 2.5 - Parsivel disdrometer and schematic description of the effect of the passage of a raindrop

This kind of instrument is able to detect 32 different diameter classes (0.05 mm to 25 mm) and speed (0.062 m/s to 24.5 m/s). The main source of error in an optical disdrometer is caused by the non-perpendicularity of the raindrop to the laser beam due to the wind. When rain particles do not perpendicularly hit the laser beam, laboratory experiments have shown that the concentration of large diameters ($D>3$ mm) increases as the fall speed decreases.

2.2.2 Impact-type disdrometer

The impact-type disdrometer (Figure 2.6) is a tool that correlates the vertical moment of a drop of rain that hits the sample surface with its diameter. The function that binds these two sizes, reported in Equation [2.1] , is valid under the assumption that the drop impacts the sensor at its own drop speed.

$$U = 0.94 \cdot D^{1.47} \qquad\qquad [2.1]$$

where U, which is the magnitude of the pulse, is expressed in Volt and D in mm.

The magnitude of this pulse is measured by a processing unit able of distinguishing 20 dimensional classes between 0.3 mm and 5.5 mm. The instrument stores the number of drops detected for each class for each sampling interval.
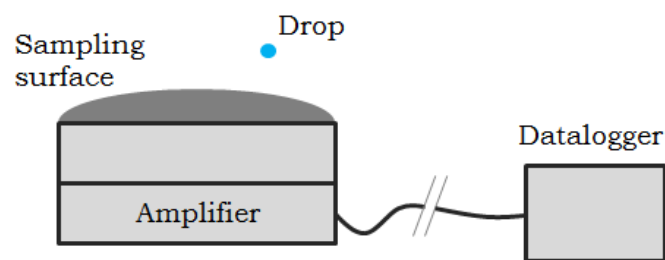
Figure 2.6 - Simplified operational scheme of an impact disdrometer. For each drop that strikes the surface the diameter is determined by a datalogger that receives an electrical signal from an amplifier. This signal is then analyze to correlate each peak with a corresponding drop diameter

Since the disdrometer is sensitive to environmental noise, during intense rain events its threshold tends to increase and drops belonging to the smaller classes (0.5 mm) are not detected. In Figure 2.7 this effect is shown during an intense event (Nystuen et al., 1995).
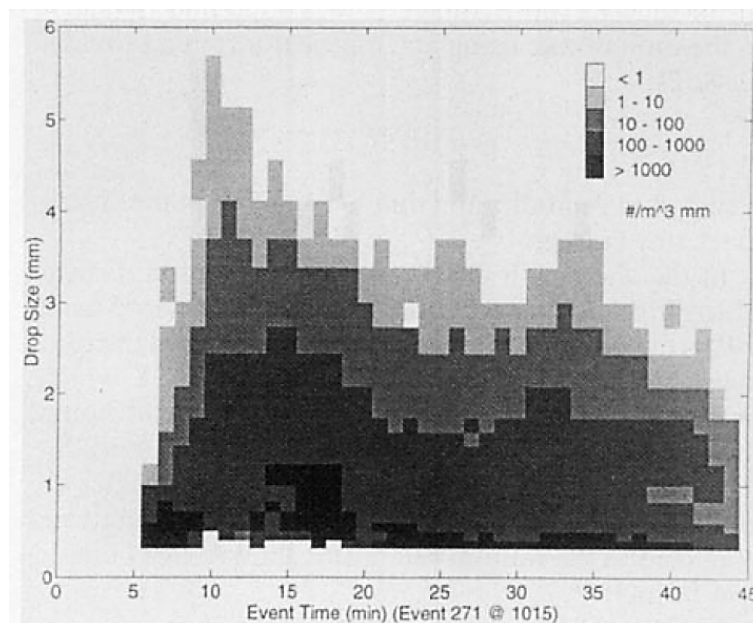
Figure 2.7 - Diametri di pioggia registrati da un disdrometro (Nystuen et al., 1995)

2.3   WEATHER RADAR

Weather radar, Figure 2.9, also called Weather Surveillance Radar (WSR) and Doppler Weather Radar, is a type of radar used to locate precipitation, calculate its motion, and estimate its type (rain, snow, hail etc.). Modern weather radars are mostly pulse-Doppler radars, capable of detecting the motion of rain droplets in addition to the intensity of the precipitation. Both types of data can be analyzed to determine the structure of storms and their potential to cause severe weather.

A typical weather radar has three main components:

1. the transmitter, which generates short pulses in the microwave frequency portion;
2. the antenna, which focuses the transmitted energy into a narrow bean;
3. the receiver, that collects the backscattered radiation from the targets that intercept the transmitted pulses (Battan, 1973).

Weather radars send directional pulses of microwave radiation. The wavelengths of 1÷10 cm are approximately ten times the diameter of the droplets or ice particles of interest. This means that part of the energy of each pulse will bounce off these small particles, back in the direction of the radar station. Although with limitations due to the earth orography (as shown in Figure 2.8) and type of emitted radiation, a single radar can characterize regions of more than 250 km radius (Sene, 2013).
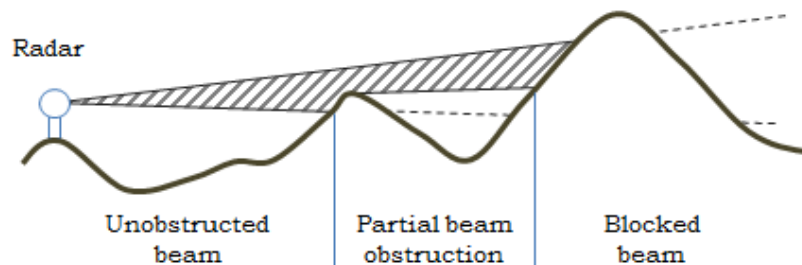
Figure 2.8 - Example of orographic obstruction to weather radar beams

Although the radar does not provide direct measures of rainfall fields, it is possible to estimate rainfall rates from the radar reflectivity measures, which are related to the presence of water.

Figure 2.9 - Typical radar station for meteorological and civil purpose

Rainfall rate and radar reflectivity are linked by the Drop Size Distribution (DSD), as recognized by Marshall and Palmer (1948). The use of standard diameter distributions leads to a power law relation between the radar reflectivity factor Z (mm^6/m^3) and the rainfall rate R (mm/h):

$$Z = a \cdot R^b \qquad\qquad\qquad [2.2]$$

where *a* and *b* are coefficients related to the DSD. The Equation [2.2], known as Z-R relationship, is inherently indeterminate, the coefficients *a* and *b* are usually estimated through an empirical approach, based on the comparison of radar and rain gauge data (e.g., Marshall and Palmer, 1948; Joss and Waldwogel, 1970).

Table 2.1 - Variability of coefficients *a* and *b* for the Z-R relationship

Precipitation type	Author	a	b
Stratiform	Marshall et al., 1955	200	1.60
Stratiform	Delrieu et al., 2000	242	1.43
Cevennes DSD	Delrieu et al., 1991	362	1.40
Convective	Joss and Waldvogel, 1968	300	1.50
Convective	Sekhon and Srivastava, 1970	300	1.35
Convective	Bouilloud et al., 2009	533	1.36

The estimation procedure is characterized by a high level of uncertainty, as can be recognized by the wide variety of coefficient values (see Table 2.1) collected in Battan (1973), Raghavan (2003) and Doviak and Zrnic (2006). A variety of papers highlights the variability of *a* and *b* according to the type of event (Tokay and Short, 1996; Bringi et al., 2003) and, during the event itself, in time and space

(Smith and Krajewski, 1993; Lee and Zawadzki, 2005; Chapon et al., 2008). Even with measured drop size distributions, recorded over a physically homogeneous period, the instrumental noise related to small sampling effect and the observational noise, due to the drop sorting effect, can lead to Z-R relationships which are only true in a statistical sense (Lee and Zawadzki, 2005).

2.4 WEATHER SATELLITES

The artificial satellites which orbit around Earth have found wide applications in the field of meteorology. Through satellite images information about ground temperature, type, height and temperature of the clouds, humidity, reflectivity, land cover, clouds amount of water precipitation intensity is obtained.

Information about precipitation is, in general, rarely used in regions that have a good coverage by the radar observations, which have the best space-time resolutions.

The satellite measurement has, however, some limitations. In particular, input precipitation accuracy decreases in snow/ice-covered surface regions and at higher latitudes with especial climatology.
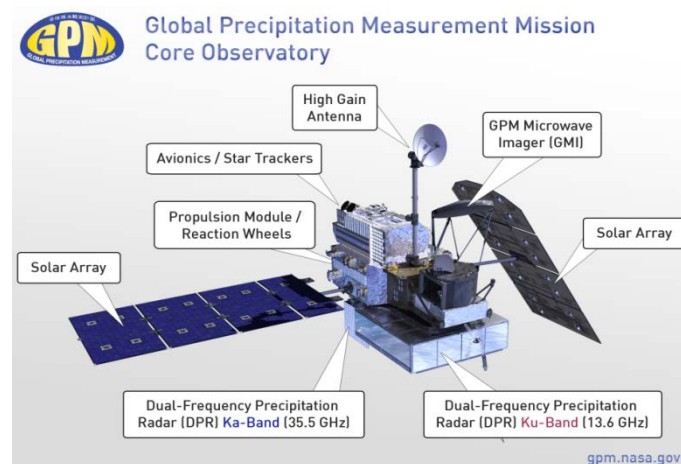
Figure 2.10 - Diagram of the GPM Core Observatory (from https://pmm.nasa.gov/gpm/flight-project/core-observatory)

Geostationary satellites, typically provide images every 15 to 30 minutes with a spatial resolution of 1 to 4 km (Sene, 2013). Due to the resolution, the information is qualitative and does not capture the variability of precipitation phenomena, nor spatial or temporal. Satellites in polar orbit, much closer to the Earth's surface (800÷1000 km compared with about 36000 km of geostationary satellites) and

moving relative to it, may provide better resolutions. The most relevant Satellite Missions have been designed and developed by NASA.

The sensors measure reflected and emitted radiation from ground, atmosphere and clouds. Specifically, they affect the area of electromagnetic spectrum that goes from visible to microwaves (see Figure 2.11 and Figure 2.12).

The measure of precipitation from space has been unclear for many years. The launch of the TRMM (Tropical Rainfall Measuring Mission) mission in 1997, now replaced by the GPM (Global Precipitation Measurement) mission in 2014 (both under the aegis of NASA), changed the perspective.

TRMM was designed to estimate, in the tropics and subtropics, heavy to moderate rain. GPM, instead, can measure every kind of precipitation, from light (less than 0.2 mm/h) to heavy rain and even solid precipitation like snow, due to the large range of frequency. All new data are obtained using an international satellite constellation. These missions also introduced for the first time the cloud radar.

Although TRMM has five instrument on board, the precision of the radar and the radiometer on GPM Core Satellite guarantee the best quality media that can be obtained from a measure from space.

With this upgrade, NASA also increase the spatial coverage. TRMM can only measure in tropical and subtropical regions (between 35°N and 35°S). GPM data, instead, cover a region between 65°N and 65°N. With a specific algorithm we can extend data from 90°N to 90°S.
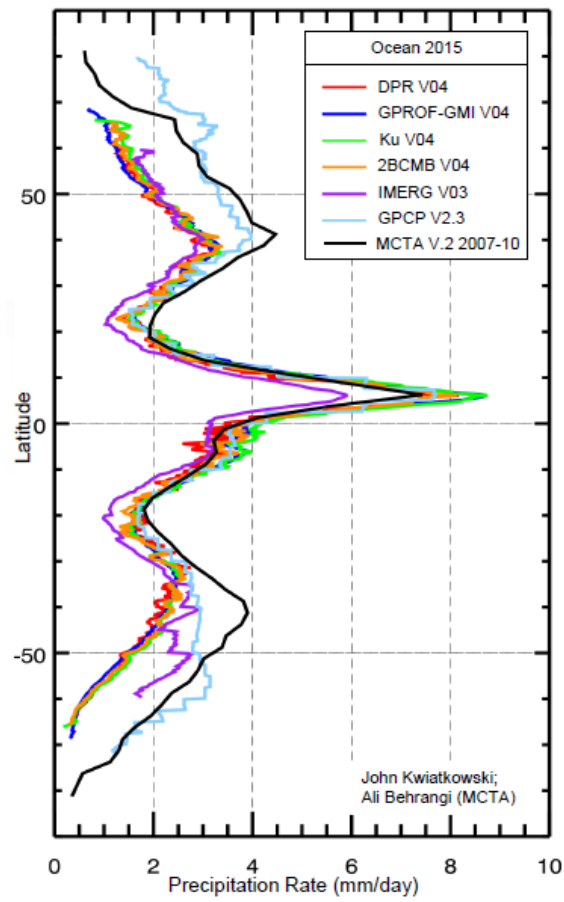
Figure 2.11 - Comparison between different levels of accuracy of NASA satellite measures and rain gauges measures (cyan line) on water surfaces
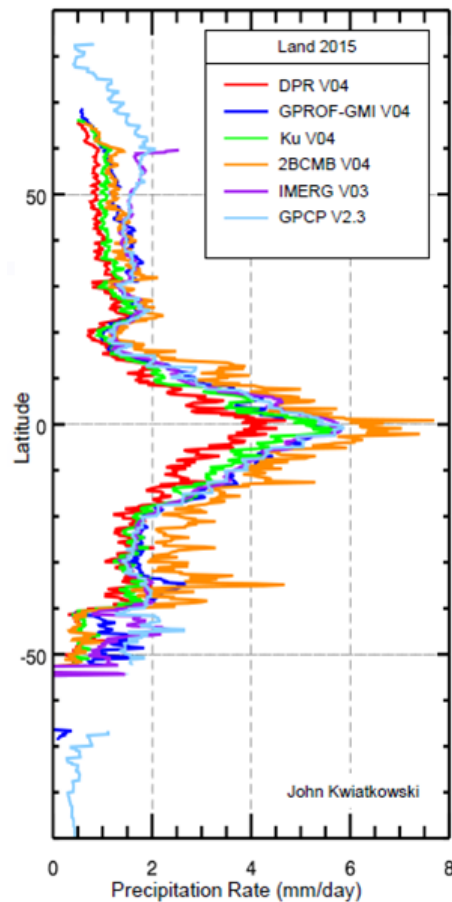
Figure 2.12 - Comparison between different levels of accuracy of NASA satellite
measures and rain gauges measures (cyan line) on land surfaces

Precipitation estimation products, usable for real time application, are now
available on a global scale every 4-5 hours. As described for the weather radar, to
determine quality measures, the satellite system need to be calibrated through at
ground measures (i.e., from a network of rain gauges). After few months from the
acquisition, Nasa gives free access for research purposes (the level 3 of the NASA
GPM data, that is the most detailed and elaborated one, is actually posted after 3
months from the acquisition).

2.5 INSTANT RAIN RATE

To improve the spatial detail of at-ground precipitation patterns a novel technique
based on the quantitative detection of rain intensity from images, i.e. from
pictures taken in rainy conditions (e.g., Figure 2.13), is here proposed. The
estimated intensity and the relative uncertainty is obtained by analytical means

and, as will be seen (Chapter 3), has the theoretical foundation in the principles of optics and photography.

The above technique is currently (2015) patent pending under the name of Instant Rain Rate - also known as IR^2 - (Allamano et al., 2015) and heads a start-up, WaterView, that takes care of its commercial development (see Chapter 6.4).

Among measuring instruments of on the ground precipitation, IR^2 technology aims to be an alternative to the rain gauge.

Figure 2.13 - Photographic image can be IR^2 technology input datum

Chapter 3

Instant rain rate technology - IR^2

In Chapter 1 and Chapter 2 we briefly described the main reasons why a large amount of at-ground measures (highly detailed in space and time) is crucial for a good description of precipitation patterns and for the calibration of weather radars and satellites relationships. In order to reach this goal, in this work, a new methodology to determine rain rate from video and images taken in rainy conditions is presented. The method is fully analytical and based on simple principles of optics and photography and is patent pending under the name of Instant Rain Rate (Allamano et al., 2015).

This kind of technology can be integrated with the existing rain gauge network providing a high detailed layer of new rain measures allowing:

- a better calibration of radar and satellite data;
- a better description of rain event that leads to a better performance of forecasting models;
- a faster response in case of urban and flash floods;
- a better management of water and treatments for agricultural purposes;
- an upgrade of safety conditions of car users.

The possible impacts of this kind of technology are many and involve a wide range of application field. In Chapter 6.4 are described some of the possible applications as explored by WaterView, a small company that is taking care of the commercial development of the technology.

The idea behind this method is quite simple and starts considering a camera observing a volume of falling raindrops. The effect is that raindrops produce sharp intensity changes in pictures and videos. Rain visibility strongly depends on camera parameters (see Figure 1.4 and Garg and Nayar, 2007). For instance, it is rather easy to verify that, at short exposure times (~ 0.001 s), rain appears in the form of stationary drops (see Figure 3.1(*a*)). At normal exposure times (i.e., 0.015 s) instead, due to their fast motion, raindrops produce blurred rain streaks (Figure 3.1(*b*), see also Schmidt et al., (2012)) because they typically stay at a pixel for a time that is far less than the exposure time. In the following, drop velocity is assumed to be equal to the drop terminal fall speed in still air (see Beard, 1976 and citing articles for details) as described in Paragraph 3.3. Under this assumption, the streak length varies as a function of the exposure time and drop diameter. For drops of 3 mm, we expect that the streak length will vary from 8 mm to 120 mm for exposure times in the range 0.001 to 0.015 s.

a)   *b*)
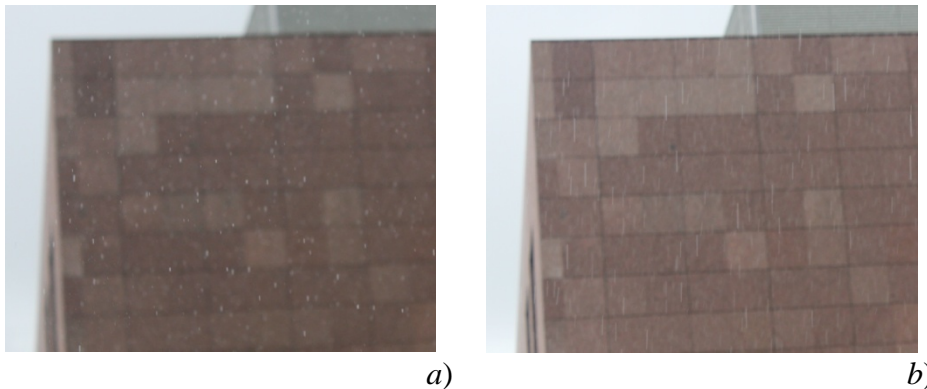
Figure 3.1 - Rain appears in the form of (*a*) stationary drops at short exposure times (te = 0.001 s); and in the form of (*b*) rain streaks at normal exposure times (te = 0.015 s)

Different rain streaks will have different width, length and intensity, depending on drop characteristics and camera parameters. The challenge here is to demonstrate that streak characteristics can be exploited to quantitatively derive drop size, drop velocity, and rain rate.

The main steps of the method are explained in the following sections, including:

- drop detection;
- blur effect removal;
- estimation of the drop velocities;
- drop positioning in the control volume;
- rain rate estimation.

3.1 DROP DETECTION

The starting point for our reasoning is the ray diagram shown in Figure 3.2, where z_0 is the focus distance, f is the focal length, z is the distance of the object (A, B or C) from the lens and f_1 is the distance of the sensor from the lens. The lens equation expresses the relation among f, f_1, and z_0.
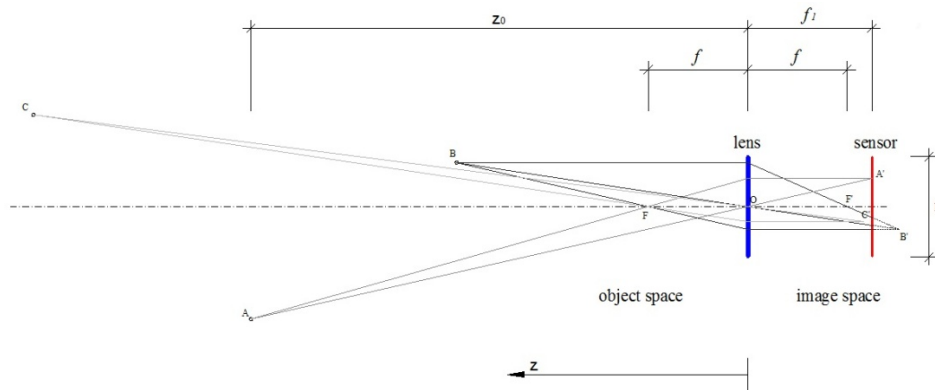
Figure 3.2 - Ray diagram. Shown are the focus distance z_0, the focal length f, the distance of the object (A, B or C) from the lens z and the distance of the sensor from the lens f_1

Candidate rain pixels are found by referring to triplets of frames, i.e. pictures taken at three adjacent time steps (*j-1*, j and *j+1*). The brightness intensity I ($0 \le I \le 255$) at each pixel in the frame *j* is compared with the corresponding pixel intensity within and between the frame *j-1* and *j+1*. If the background remains stationary in the frames, then the conditions

$$I(j) - I(j\text{-}1) > S_1 \qquad \& \qquad I(j) - I(j\text{+}1) > S_1 \qquad\qquad [3.1]$$

can be used to detect candidate drops with reference to the *j-th* image, S_1 being a threshold that represents the minimum change in intensity due to a drop. The conditions in equation [3.1] are both to be met in order to select real drops. In fact, we have found that pixels that meet just one of the two conditions cannot always be associated to raindrops but to random noise in the image (i.e., apparent particles or irregular borders).

The isolation of candidate rain pixels along a focused rain streak (for the case of out-of-focus streaks see the following section 3.2) allows to detect:

- the number of candidate raindrops within the gauged volume by counting the number of streaks;
- the drop diameter, D_P (in pixels, as indicated by the subscript "*P*"), by setting it to the average width of the streak (see Equation [3.5] for the variation of pixel dimension with z);

- the drop velocity, which is proportional to the ratio of the net streak length to the exposure time (t_e).

The net streak length is obtained by subtracting one drop diameter D_P to the vertical component of streak length L_P (in pixels), or simply streak length in the following, as it appears on the image. In fact, the velocity of a moving object is proportional to the distance covered in a time step by a fixed point of the object; considering the raindrop center as the fixed point, this will cover L_P - D_P pixels in a time t_e, while the total length of the streak will be L_P, because the drop occupies $D_P/2$ pixels above the drop center, and $D_P/2$ pixels below it.

For non-stationary backgrounds, e.g. vegetation with leaves moving in the wind, Equation [3.1] is not effective to detect candidate drops. In this case the subtraction of two frames does not guarantee the removal of the false positives created by the visual effects of light interaction with moving surfaces. False positives could be detected with specific post-processing algorithms that, for instance, verify the presence/absence of sub-vertical preferential directions ascribable to the effect of rain streaks. Specific algorithms exist from the computer vision community to separate raindrops from other moving objects, for example for raindrop removal in traffic-control videos (e.g., Garg and Nayar, 2007).

3.2 BLUR EFFECT

The appearance of rain in pictures is significantly affected by blur. The blur effect is caused by a cone of light rays from a lens not coming to a perfect focus when imaging a point source. The optics behind the formation of the blur circle is sketched in Figure 3.3 as a function of the aperture diameter (A), for objects lying behind, within and before the focus plane.

The diameter of the blur circle (or circle of confusion, $c_P(z)$, in pixels) is obtained by dividing the diameter of the auxiliary blur circle C by the magnification factor f_1/z_0. C is obtained via similar triangles as $C = A\dfrac{|z - z_0|}{z}$. The blur circle in the image plane can hence be written as $c = A\dfrac{|z - z_0|}{z} \cdot \dfrac{f_1}{z_0}$, which exemplifies the dependence of the blur magnitude on z, z_0, f_1 and A. By setting $z = z_0$ in the expression for c, one obtains that the blur effect is null on the focus plane. The magnitude of the blur in pixels ($c_P(z)$), to be compared with the drop diameters and streak lengths, is obtained as

$$c_P(z) = \frac{c \cdot H_P}{h} = \frac{A|z - z_0|}{z} \cdot \frac{f_1 \cdot H_P}{z_0 \cdot h} \qquad [3.2]$$

where H_P is the image height in the focus plane (in pixels) and h is the sensor height in millimeters (see Figure 3.2).
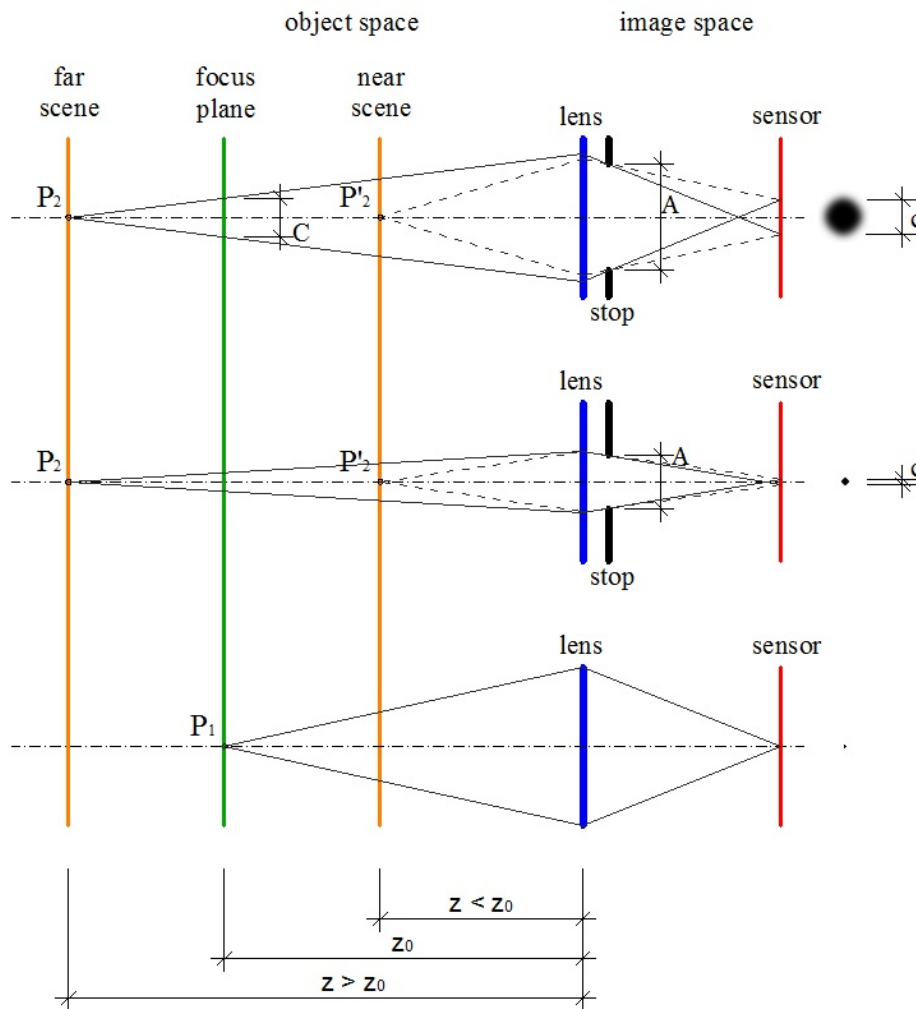
Figure 3.3 - Lens and ray diagram for an out-of-focus object (P_2 and P_2', respectively before and behind the focus plane) and a focused object (P_1). Shown are the blur circle c and auxiliary blur circle C in the focus plane

Blur affects both D_P and L_P of out-of-focus drops, by fictitiously enhancing their size of a quantity $c_P(z)$. $D_{P,b}$ and $L_{P,b}$ identify the blurred diameters and blurred rain streak lengths, respectively. Hence, when observing a volume of rain with a camera, one detects the "true" diameters and streak lengths of drops belonging to the focus plane. For out-of-focus drops, instead, only the corresponding blurred

quantities may be directly inferred from the picture. Moreover, the blur effect critically interacts with the effect of the threshold S_1 in equation [3.1]: in fact, the blur acts on the drop projection on the image as a moving-average filter, changing the brightness pattern due to a drop from a sharp discontinuity (blue dashed line in Figure 3.4) to a smooth, trapezoidal-shaped pattern (continuous line in Figure 3.4).
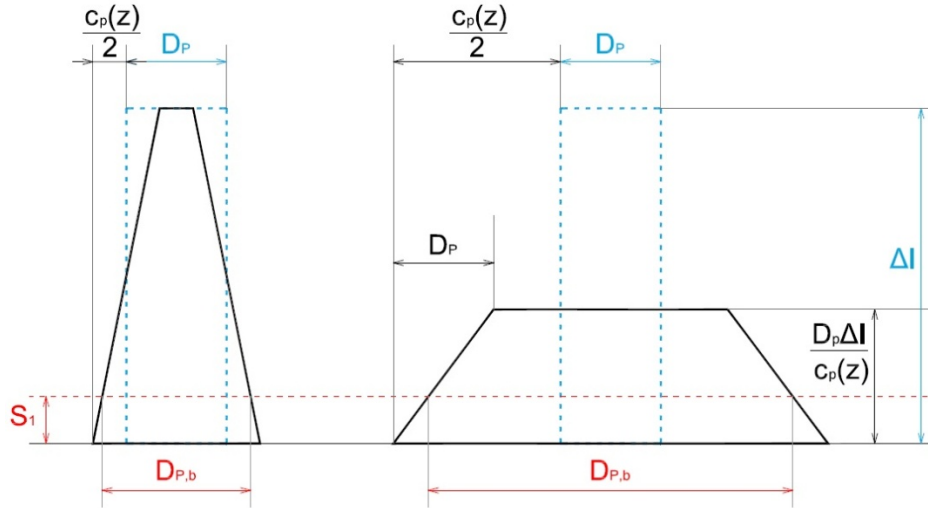
Figure 3.4 - Blur effect on the brightness pattern of a drop. The dashed blue lines indicate the sharp brightness discontinuity produced by a focused drop (D_P is the real drop diameter, ΔI is the maximum positive brightness impulse due to a drop). The smooth, trapezoidal-shaped patterns are the blurred brightness patterns typical of out-of-focus drops ($c_P(z)$ is the magnitude of the blur in pixels). The red line represents the threshold filter in Equation [3.1], with $D_{P,b}$ being the drop diameter as it appears in the blurred (and filtered) image. On the left hand side the case of a slightly out-of-focus drop. On the right hand side the case of a severely out-of-focus drop

The drop detection algorithm in turn acts as a further threshold filter (red dashed line in Figure 3.4) on the blurred projection of the drop. As a result of the combined effect of these two filters, the relation between blurred and real drop diameter and streak length can be obtained from simple geometrical reasonings (see Figure 3.4), producing

$$\begin{cases} D_P = D_{P,b} - c'_P(z) \\ L_P = L_{P,b} - c'_P(z) \end{cases}$$

[3.3]

where $c'_P(z) = c_P(z) \cdot \left(1 - \dfrac{2S_1}{\Delta I}\right)$ and ΔI is the maximum positive brightness impulse due to a drop (we have assumed $\Delta I = 50$ after inspection of rain images). Note that, in the presence of blur, drops that are either very small or very distant

from the focus plane may produce small brightness variations in the image, which may be undistinguishable from the random noise. This effect, in Figure 3.4, would generate trapezoidal patterns whose height falls below the threshold S_1. This is the reason why, in the following, limit values are imposed for the distance from the focus plane and drop size to be considered.

From the image analysis one is thus able to obtain $D_{P,b}$ and $L_{P,b}$ values; to obtain D_P and L_P one should solve the system of equations [3.3]; however, in this system there is a third unknown quantity, which is the distance from the lens z. One more equation is thus needed to position the drops at the right distance z from the lens and infer the blur magnitude.

3.3   DROP VELOCITY ESTIMATION

To set the third equation we rely on the estimates of the drop velocity (v) derived from the ratio of the net streak length (calculated as $L_P - D_P$ multiplied by the pixel dimension $d_P(z)$ to express it in millimetres, see below) to the exposure time. We set the estimated drop velocity v to be equal to the drop terminal speed (Villermaux and Eloi, 2011), $\sqrt{\dfrac{4}{3}\dfrac{\rho}{C_D \cdot \rho_a \cdot 1000} g \cdot D}$, where C_D is the drag coefficient, which is approximately equal to 0.5 for a sphere, ρ is the water density, ρ_a the air density and g is the gravitational acceleration. The terminal speed is also a function of the drop diameter, being $D = D_P \cdot d_P(z)$. The diameters and streak lengths are expressed in millimetres, while other variables are in IS units. Note that falling raindrops reach their terminal speed in a few meters distance (see van Djik et al., 2002; Testik et al., 2011). The equivalence between the two expressions for drop speeds reads:

$$\frac{(L_P - D_P) \cdot d_P(z)}{t_e \cdot 1000} = \sqrt{\frac{4 \cdot \rho \cdot g \cdot D_P}{3 \cdot C_D \rho_a \cdot 1000} \cdot d_P(z)} = \sqrt{21.62 \cdot D_P \cdot d_P(z)} \qquad [3.4]$$

The dependence on z is expressed through D_P and L_P (see Equation [3.3]) and through the variation of the pixel dimension d_P with the distance z of the object from the lens, expressed as (see Figure 3.2):

$$\frac{h}{f_1} = \frac{H(z)}{z} = \frac{H_P \cdot d_P(z)}{z} \quad \Rightarrow \quad d_P(z) = \frac{h}{f_1 \cdot H_P} z \qquad [3.5]$$

In the following we assume Equation [3.4] to be valid for all drop diameters. Evidence exists, however, that very small drops (e.g., D ≤ 0.5 mm) may assume super-terminal speeds as the result of larger drops' fragmentation (Montero-

Martinez et al., 2009; Larsen et al., 2014). In this study we do not consider this phenomenon because very small drops play a minor role in the rain rate estimation (see Leijnse and Uijlenhoet, 2010).

3.4 DROP POSITIONING AND CONTROL VOLUME DEFINITION

Drop positioning along the dimension z, i.e. moving away from the lens, represents one of the most challenging aspects of the methodology, since we need to infer the third dimension from an intrinsically two-dimensional information (the image). The position of the drops in z is obtained by substituting Equation [3.5] in Equation [3.4] and solving the system of Equations [3.3] and [3.4], where the unknowns are D_P, L_P and z. The equation in z to be solved, in squared form, hence results:

$$\alpha^2 z^2 = \beta \cdot z - \gamma |z - z_0|$$ [3.6]

where:

$$\alpha = \frac{L_{P,b} - D_{P,b}}{t_e \cdot 1000} \cdot \frac{h}{f_1 \cdot H_P},$$

$$\beta = 21.62 \frac{D_{P,b} \cdot h}{f_1 \cdot H_P},$$

$$\gamma = 21.62 \frac{A}{z_0} \left(1 - \frac{2S_1}{\Delta I}\right).$$

Four analytical solutions in z are obtained: two $z > z_0$ (z_1 and z_2) and the other two for $z < z_0$ (z_3 and z_4). An example of these four solutions is shown in Figure 3.5 in relation to the two terms of Equation [3.6]. Note that the figure is meant to be a scheme to explain the solution of Equation [3.6]. The drop we used is characterized by a large diameter ($D = 4.5$ mm), to improve graphical readability. We show that the solutions z_2 and z_3 do not respect their existence boundaries (being $z_2 < 0$ and $z_3 > z_0$ respectively) and are hence classified as non-admissible. z_1 and z_4, instead, fall within their respective domains of existence, z_1 and z_4 being positioned at $z > z_0$ and $z < z_0$, respectively. The fact that two solutions remain valid implies that drops cannot be univocally collocated within the sampled volume; we thus admit that two different positions in z, and hence two different diameters D, may exist that satisfy the system of Equations [3.3] and [3.4].
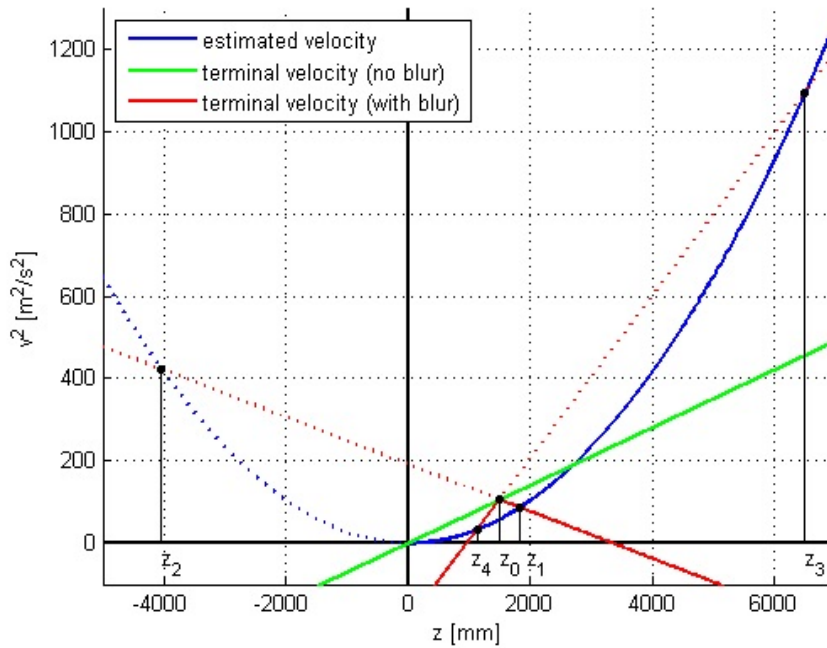
Figure 3.5 - Graphical scheme of the solutions of Equation [3.6]. In blue the quadratic curve relative to the left hand side term of Equation [3.6], in red the piecewise linear behaviour of the right hand side term of Equation [3.6], in green the squared terminal velocity without the effect of blur

Before making a decision between z_1 and z_4, an additional filter is set: the depth of the sampled volume is constrained between $(2/3) z_0$ as a lower bound and $2 z_0$ as an upper bound (see Figure 3.6). In fact, a point feature in $(2/3) z_0$ or in $2 z_0$ would produce a blur circle in the focus plane $C = A / 2$. This condition, in some cases, allows one to flag as unlikely one of the two solutions and to identify the other solution as the best one.

The sampled volume V (i.e., the volume of the truncated pyramid with bases in $(2/3) z_0$ and $2 z_0$, Figure 3.6) can be computed as a function of the image dimensions in pixels, H_P and W_P, and of the width of the volume section at $z = 2 \cdot z_0$,

$$V = \frac{52}{81}\left(z_0 \frac{W_P}{H_P} H_1^2 \right)$$ [3.7]

Despite the confinement of the sampled volume, two admissible solutions z_1 and z_4, and hence two admissible diameters $D(z_1)$ and $D(z_4)$, still exist for the majority of drops.

Non univocal cases of drop positioning can be further reduced by constraining drop diameters: we assume that drop diameters larger than 6 mm and smaller than 0.5 pixel are very unlikely to occur, the first being a physical limit that is currently found in the literature (see, among others, Ulbrich, 1983; Montero-Martinez et al., 2009), the latter deriving from the very low variations in pixel brightness induced by drops occupying less than half of the pixel. Observe that we just flag as unlikely diameters greater than 6 mm (to avoid gross errors due to very near drops or streaks aggregation), while we are aware that super-large drops may occasionally occur in nature (e.g., Hobbs and Rangno, 2004).These conditions help to discern the most likely solution between z_1 and z_4, and to univocally attribute N_{1u} drops to z_1 and N_{4u} to z_4, with $N_{1u} + N_{4u} < N$, where N is the total number of detected raindrops.
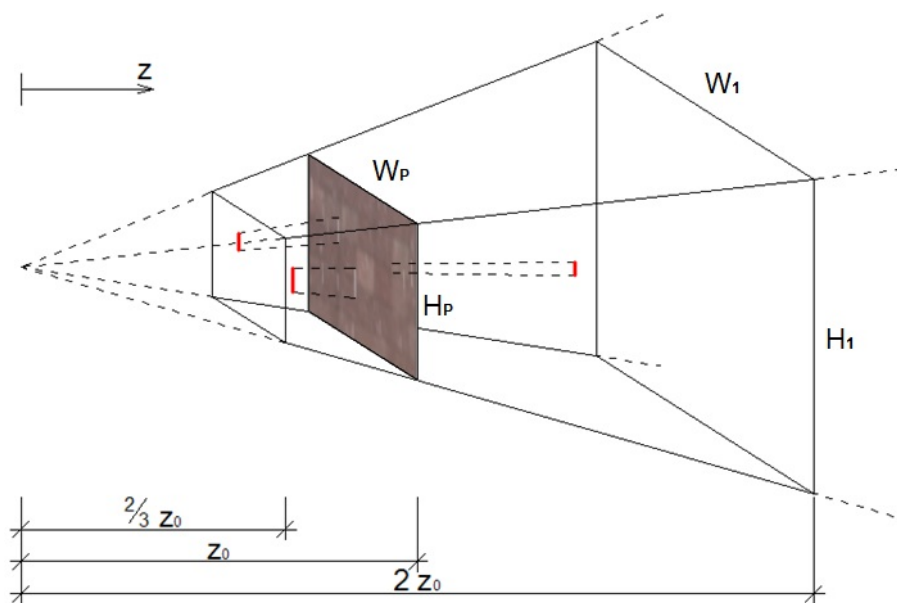
Figure 3.6 - Sampled volume V as a function of z_0 (i.e. distance of the focus plane from the lens). H_P and W_P are the image dimensions in pixels, and W_1 and H_1 are the height and width of the volume section at $z = 2z_0$, respectively

To disentangle the remaining $N-(N_{1u} + N_{4u})$ cases of ambiguous drop positioning, we adopt a pragmatic approach: we decide to attribute drops to z_1 and z_4 randomly, by determining the probability to fall before (i.e. in z_4) or behind (i.e. in z_1) the focus plane. We compute the probability P_1 for a drop to fall in the volume behind z_0 as the ratio between the volume of the truncated pyramid with bases in z_0 and $2z_0$ and the total sampled volume V. P_4, i.e. the probability for a drop to fall in the volume before z_0, is computed accordingly as $P_4=1–P_1$. The number of drops N_{1a} attributed to the volume behind z_0 is hence computed as

$$N_{1a} = P_1 \cdot N - N_{1u} \qquad\qquad [3.8]$$

Conversely, the number of drops N_{4a} attributed to the volume before z_0 is obtained as

$$N_{4a} = (1 - P_1) \cdot N - N_{4u} \qquad\qquad [3.9]$$

For each ambiguously positioned drop, a random number q is sampled from a uniform (0, 1) distribution. If the sampled value $q < N_{1a} / (N - N_{1u} - N_{4u})$ the drop is attributed to z_1, otherwise to z_4. We have verified with Monte Carlo simulations that this random attribution algorithm only marginally affects the rain rate estimation.

3.5   RAIN RATE COMPUTATION (WITH UNCERTAINTY)

For each picture P_j, the rain rate R_{P_j} (in mm/h) is computed under the hypothesis of spherical raindrops with diameters D_i, and terminal speeds v_i. Each drop is assumed as responsible of a quota R_i of the total rain rate of the image, so that R_{P_j} can be written as

$$R_{P_j} = \sum_{i=1}^{N} R_i = \sum_{i=1}^{N} \frac{1}{6}\pi \cdot D_i^3 \cdot v_i \cdot \frac{3.6 \cdot 10^{-3}}{V} \qquad\qquad [3.10]$$

where N is the total number of drops in the image, $\frac{1}{6}\pi \cdot D_i^3$ is the volume of the i-th drop (in mm^3), v_i is the (terminal) velocity of the drop (in m/s), and V the total sampled volume (in m^3).

A measure of the uncertainty associated with the estimate of R_{P_j} can be obtained to complement Equation [3.10]. The distribution of the rain rate quota due to a single-drop $p_R(R)$ can be derived from the distribution of diameters, given that R and D are related through a monotonically increasing relation,

$$R(D) = K \cdot D^{7/2} \qquad\qquad [3.11]$$

where K is a multiplicative constant and the term $D^{7/2}$ can be factorized as the drop volume ($\propto D^3$) times the drop speed ($\propto D^{1/2}$). On this basis one can express the first and second order moments about the origin of the single-drop rain rate as:

$$M_{1,R} = \int_0^\infty R \cdot p_R(R)\,dR = \int_0^\infty R(D) \cdot p_D(D)\,dD = K\,\frac{105\sqrt{\pi}}{16}\,\overline{D}^{7/2} \qquad [3.12]$$

and

$$M_{2,R} = \int_0^\infty R^2 \cdot p_R(R)\,dR = \int_0^\infty R^2(D) \cdot p_D(D)\,dD = 5040 \cdot K^2 \overline{D}^{\,7} \qquad [3.13]$$

where the derived distribution theory is applied to set the equivalence between the term in R and the term in D. For simplicity, the drop diameters are assumed to be exponentially distributed, with average value $\overline{D}$ (see Marshall and Palmer, 1948 and Kostinski and Jameson, 1999 for a discussion on the validity of this assumption).

Since the number N of drops is approximately Poisson-distributed (see Kostinski and Jameson, 1997 and Uijlenhoet et al., 2006), R_P can be modelled as a compound Poisson process (Benjamin and Cornell, 1970), with coefficient of variation

$$CV_{R_P} = \frac{\sqrt{N \cdot M_{2,R}}}{N \cdot M_{1,R}} \cong \frac{6.15}{\sqrt{N}} \qquad\qquad [3.14]$$

where CV_{R_P} is the coefficient of variation of the rain rate of the image. Note that the results obtained from Equations [3.14] are intended as indicative of the order of magnitude of the uncertainty associated with the estimate of R_{P_j}; deviations from the assumption of exponentially distributed diameters and Poisson distributed numbers of drops affect the result in Equation [3.14], see Section 3.6.

Since CV_{R_P} is rather large, given that N is typically between 100 and 1000 (as shown in the following section), the uncertainty inherent in the estimation of R_P may be rather large as well. We thus propose to derive the rain rate by averaging the results from sets of ten independent images. The final rain rate is hence written as:

$$R_t = \frac{\sum_{j=1}^{10} R_{P_j}}{10} \qquad\qquad [3.15]$$

with associated coefficient of variation $CV_{R_t} = 1.93/\sqrt{N}$, obtained by dividing Equation [3.14] by a factor $1/\sqrt{10}$.

The method described so far is amenable of quasi-unsupervised applications. The method, in fact, is characterized by one parameter only: the brightness threshold S_1 and in the next section the effect of varying S_1 on the resulting drop size distributions, number of raindrops and rain rates (with uncertainty) is shown.

3.6   APPLICATION AND VERIFICATION

In this section the results of the application of the method to real rain events are shown. The analyses in particular concern four rain events (E) which occurred in Torino (Italy) in November and December, 2014. In Chapter 5 the best performing method, determined as a combination of the procedures described in Chapter 3 and Chapter 4, has been applied to a longer sample of rain events in order to determine its accuracy.

To reduce the turbulence effects due to the presence of other buildings the measuring site is located on a large roof terrace. In order to fix the pictures' background a camera (Canon EOS 550D) is positioned on site mounted on a tripod and is shielded from direct raindrop splashing. Since the optical axis of the camera is horizontal, raindrops are perceived as sub-vertical streaks in the image. A tipping-bucket rain gauge (Davis) measures the benchmark rain rates (R_g).

In Table 3.1 the structure of the events' database is summarized. We define a time window of one-minute length; within the interval three sets of ten pictures are acquired; each set lasts for about six seconds. In order to explore the sensitivity of the method to different exposure times and sampled volumes, the camera acquisition parameters are varied among the intervals. The complete information about the camera parameters that were set for picture acquisition is reported in Appendix A (Table A.1. See Allamano et al., 2015). Each row in the table refers to a one-minute time interval. The database contains 104 elements (minutes) in total.

We chose a one-minute time interval because it is comparable with the temporal resolution of the manual rain gauge. In this respect, it is worthwhile to be noted that, since the measurement resolution of the tipping bucket rain-gauge is closely related to the size of the tipping rain collector (typically 0.2 mm), the minimum intensity that a rain gauge can perceive is 12 mm/h. As a consequence, the rain gauge is intrinsically unable to provide reliable measures on short time intervals in the presence of moderate rain intensities and requires to extend the acquisition window in order to collect a sufficient amount of water. Intensity measures lower than 12 mm/h, with temporal resolution of one minute, are hence the result of post-analysis algorithms, commonly provided by the producer as closed source software (Habib et al., 2001).

Table 3.1 - Shown are, for each gauged event, the camera acquisition parameters (focal length f, F-number, exposure time t_e, focus distance z_0), the sampled volume V, the number of minutes of acquisition for each event and the maximum, minimum and average rain intensity registered by the rain gauge during the event

Event	Intervals	Focal length [mm]	F-number	Exposure Time [s]	Focus Distance [m]	Volume [m^3]	R_g [mm/h]		
							min	max	mean
04/11/2014	36	55	F/5.6 F/6.3 F/7.1	$\frac{1}{160}, \frac{1}{200}, \frac{1}{250}$	1.5, 2.0	~0.9 ~2.1	2.3	14.0	5.6
11/11/2014	15	55	F/5.6 F/6.3 F/7.1	$\frac{1}{160}, \frac{1}{200}, \frac{1}{250}$	2.0	~2.1	1.8	7.0	4.2
17/11/2014	18	55	F/5.6 F/6.3 F/7.1	$\frac{1}{160}, \frac{1}{200}, \frac{1}{250}$	1.5, 2.0	~0.9 ~2.1	1.3	6.0	2.8
01/12/2014	35	55	F/5.6 F/6.3	$\frac{1}{160}, \frac{1}{200}$	2.0	~2.1	3.2	38.2	9.3

We performed drop detection on triplets of pictures [*j-1*, *j*, *j+1*], including boundary triplets, e.g. we consider picture #1 adjacent to picture #10 and #2. Candidate drops are detected according to Equation [3.1]. The brightness threshold S_1 is varied between 3 and 10. Figure 3.7 shows an example of the resulting images before and after applying the drop detection algorithm. The results refer to different values of S_1. It can be notice that higher thresholds lead to more definite drop profiles but, otherwise, may tend to underestimate the number of drops.
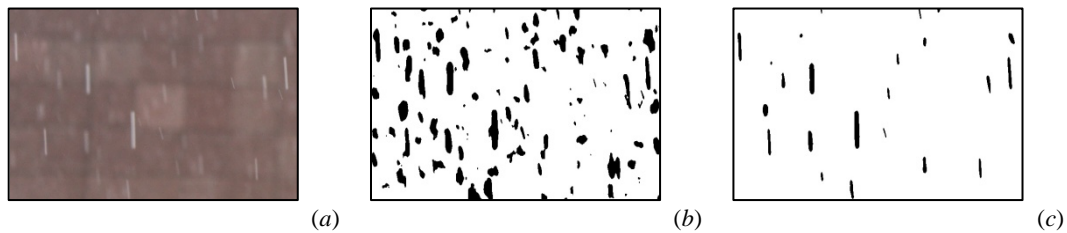
Figure 3.7 - Drop detection: (*a*) original picture and detected drops after application of the brightness threshold filter, with (*b*) $S_1 = 3$, (*c*) $S_1 = 10$. The image refers to a portion of Figure 3.1(*b*)

To detect the number (*N*) of candidate raindrops within the gauged volume the number of streaks are counted toward the isolation of adjacent rain pixels along a rain streak. Since for higher thresholds only the brightest pixels are retained, *N* significantly depends on the value of the threshold S_1. Figure 3.8 exemplifies this dependency for every set of one acquisition interval. The behavior is similar for all the sets. For each set of ten pictures we obtain ten different estimates of the number of drops, one for each picture of the set, by applying the drop detection procedure. For each set and for each S_1 value, $N(S_1)$ is then obtained as the average number of drops over the ten pictures, as described in Section 3.5. Figure 3.8 refers to a sampled volume of $V = 2.1$ m^3.

Once the drops are detected, the diameters D_P are inferred as the average number of pixels covered by the streak width over the streak length, for each drop. By multiplying D_P by the pixel dimension $d_P(z)$ the diameters *D* in millimeters are then obtained. In practice, since d_P is dependent on *z*, this operation requires to assign a position to each drop, performed as described in Section 3.4.
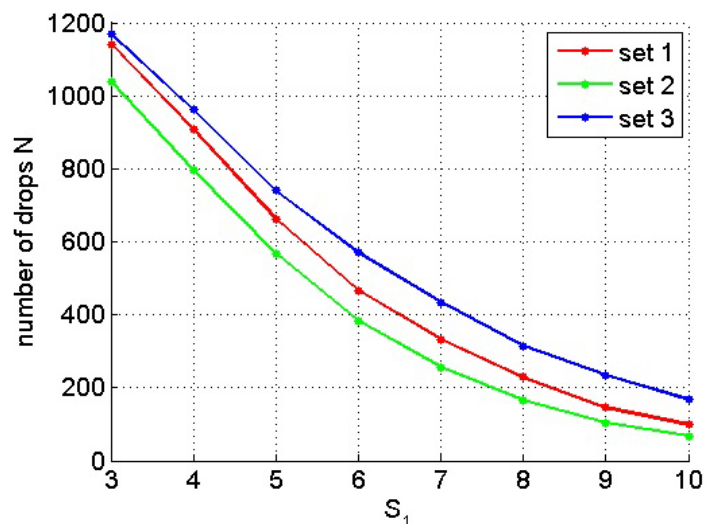
Figure 3.8 - Number of raindrops N as a function of the brightness threshold S_1

In Figure 3.9 the exceedance probabilities of the diameters $1 - P_D(D)$, where $P_D(D)$ is the drop size distribution that we obtain for the event examined in Figure 3.8 are reported. Panel (*a*) exemplifies the variations of the drop size exceedance probabilities for a specific picture and varying thresholds S_1. In panel (*b*) the variability of the diameter distribution throughout a set of ten pictures is instead shown.

(*a*)   (b)
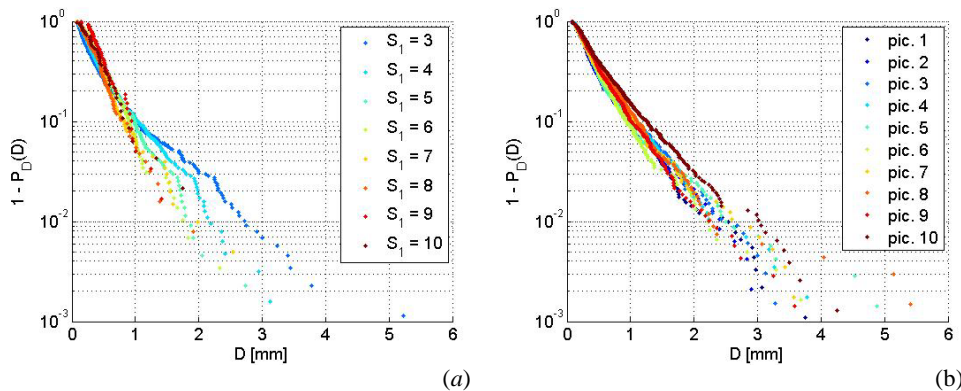
Figure 3.9 - Drop size exceedance probabilities. In panel (*a*) the variations of the drop size exceedence probability for a specific picture and varying thresholds S_1 are shown. Panel (*b*) exemplifies the variability of the diameter distribution throughout a set of ten pictures

The shapes of the distributions reported in Figure 3.9 are reasonably consistent with the exponential drop size distributions documented in the literature (Marshall and Palmer, 1948; Villermaux and Bossa, 2009). For *D*<1 mm deviations from the theoretical shapes may be found. These deviations are partially to be ascribed to the methodology. In fact, in some cases, the method fails the detection of the smallest droplets, due to the combined effect of blur and threshold filtering (see Section 3.2). However, other methods (e.g., Ulbrich, 1983; Villermaux and Bossa, 2009) recognize the uncertainty of the distribution regarding small drops.

The tails of the distribution show a significant spread for large diameters (e.g. *D*>4mm). This variability may be partially due to the hypothesis of spherical drops, which may be questionable for larger drops (see, among others, Beard et al., 2010). Future analyses will aim at assessing the impact of this assumption on the rainfall rate estimation.

According to Equation [3.10], it is necessary to assign a position z_i and a diameter D_i to each drop *i* of the image *j* in order to evaluate the rain rate R_{P_j} on single pictures. The intensities R_{P_j} are then averaged to estimate R_t for each set of pictures. As discussed in Section 3.5, the averaging allows one to reduce the uncertainty. In Figure 3.10(a), an example of rain rate estimates obtainable with

the method is shown. Each curve is evaluated on one set of ten pictures and refers to the values assumed by R_t for varying thresholds S_1. The curves are inversely proportional to the brightness threshold. In fact, the curves decrease for increasing values of S_1. The filled bands around the curves are obtained as $R_t \pm \sigma_t$, where the standard deviation σ_t is calculated as $1/\sqrt{10}$ times the standard deviation of the ten R_{P_j} values. The resulting band width is generally in good accordance (slightly larger) with the results shown in Section 3.5. Deviations are probably ascribable to non-exponential drop size distributions and to epistemic uncertainty.

To choose the brightness threshold, in order to finalize the method and to obtain an estimate of the rain rates within the one-minute interval, we compare the reference rain rate R_g measured by the manual gauge with the curve obtained by averaging the three $R_t(S_1)$ values. Since the rain gauge measures refer to one-minute intervals while the picture sets are representative of very short time intervals (lasting 6 seconds each), this further averaging is essential. An example is shown in Figure 3.10(b), where the threshold $S_1 = 5$ is identified as the most appropriate one to match the measures of the camera with the measures of the gauge.

(*a*)   (*b*)
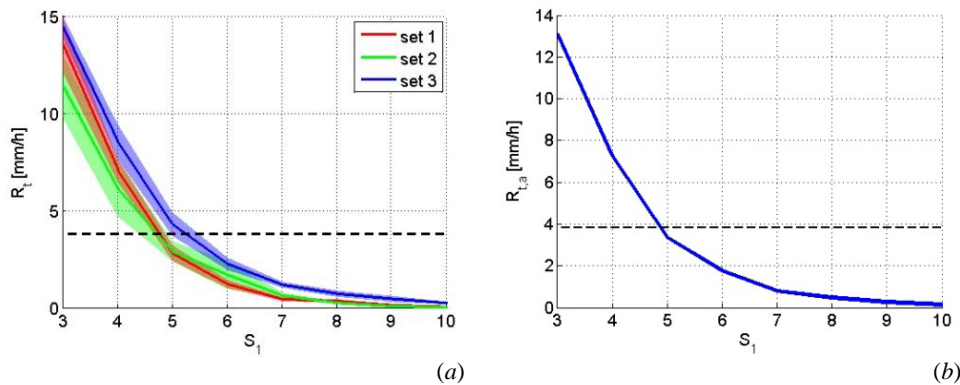
Figure 3.10 - For varying values of the brightness threshold S_1, shown are: (*a*) the estimated values of R_t over the five sets of the event $E=1$, $J=2$; (*b*) the average estimated rain rate compared with the rate measured by the reference rain gauge.

For each one-minute interval, we evaluated the optimal S_1 values. The results are reported in Appendix A, column $S_{1,opt}$ (Allamano et al., 2015). For this application, we used a rather wide range of camera parameters. As a consequence, some of the pictures (in particular those with low z_0 and t_e values) turned out to be rather dark. We notice that the quality of the rain rate estimate significantly decreases when the average brightness falls below 90 (in a 8 bit scale that goes from 0 to 255). Because of this, we decided to limit our analyses to the sub-

sample of 64 minutes with average brightness greater than 90. The mean absolute percentage error (MAPE), root mean square error (RMSE) and bias are calculated for the whole sub-sample and then for each parameter combination and brightness threshold. We obtain MAPE=0.4, RMSE=3.72 mm/h, bias=0.90 mm/h for the sub-sample, while the best performing parameter combination occurs for S_1=5, with higher exposure times (1/160 s) and greater focus distances (z_0=2m), as shown in Figure 3.11. This combination allows one to select pictures with longer streak paths (more robust against the detection procedure) and greater sampling volumes (more drops, more statistically sound estimates). Note that $S_1 = 5$ allows one to minimize the three statistics at the same time: MAPE = 0.26, RMSE = 3.01 mm/h and bias = -1.16 mm/h. In the Appendix A (Allamano et al., 2015) we report, for each one-minute interval, the rain rates estimated with fixed $S_1 = 5$ ($R_{t,S_1=5}$). In Figure 3.11(*b*), an indication of the uncertainty associated with the measures of the tipping bucket rain gauge, estimated as $\sigma_{Rg} = 135 \cdot R_g^{-0.8}$ (Habib et al., (2001)), is shown.
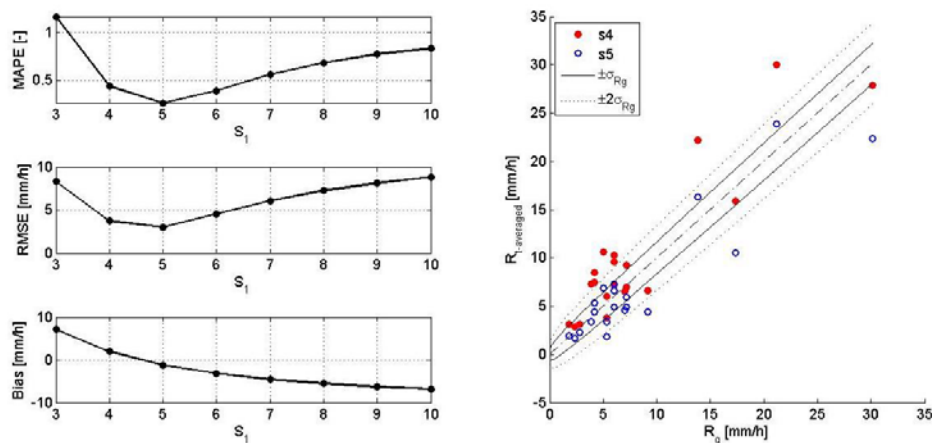
Figure 3.11 - Left-hand side graphs: Dependence of MAPE, RMSE and Bias on S_1. Right-hand side graph: Scatter plot relating the values of R_t (averaged over the one-minute interval) with R_g. Different dot colors refer to different values of the threshold S_1. Solid and dotted lines are traced respectively as $R_g \pm \sigma_{Rg}$ and $R_g \pm 2\sigma_{Rg}$

3.7 DISCUSSION

In this Chapter we have introduced a technique for measuring rainfall, based on the estimation of instantaneous rain rates from pictures of rainy scenes.

The image processing technique is described, and consists of five phases: i) drop detection, ii) blur effect removal, iii) estimation of the drop velocities, iv) drop

positioning in the control volume, and v) rain rate estimation. The idea of a camera-based rain gauge was already in the paper by Garg and Nayar (2007) However, the practical implementation was only sketched there, and seemingly lacked essential features as the drop positioning in the control volume. Also other steps of the method, including for example drop detection and blur removal, are treated here with a different approach, explicitly targeted at rain intensity estimation rather than at rain removal from images and videos.

The quality of the results of the image processing strongly depends on the settings of the camera during the shooting. Image acquisition, in fact, requires the camera parameters to be properly set in order to capture sufficiently large at-focus volumes and appreciable raindrop streaks. Hence, to obtain proper pictures, the two most influencing camera parameters to be set are the focus distance (z_0) and the time of exposure (t_e). We have found that good results are obtained with $z_0 \cong 2000\,\text{mm}$ and $t_e = 1/160\text{s}$.

The strength of the method resides in its parametric parsimony. In fact, only one parameter (i.e. the brightness threshold S_1 adopted for drop detection) has to be set to obtain a rain rate estimate. The application to four rain events that occurred in Torino (Italy) allows us to identify the optimal settings for the camera and the best value of the brightness threshold S_1.

In Chapter 5 is described the application of the method, modified in accordance with the results obtained in the Chapter 3 and Chapter 4, to a bigger sample of photographs.

Chapter 4

Advances and improvements to the IR^2 method

As described in Section 3.6, the IR^2 method has some limitation as a result of the light conditions and the camera parameters. Therefore we had to reduce our sample from 104 minutes to 64, and then to 20. In this section we explore some possible alternatives to extend the sample again. These changes are applied to the 20 minutes sample to make the comparison with the original method easier. The open issues about the procedure described in Chapter 3 are about drop recognition. The presence of noise and false positives in drop detection affects both rain rate estimation accuracy and running time. In most cases the drops, so far represented as distinct entities, are fragmented and noisy (Figure 4.1(a)) and have jagged contours and empty areas inside them (Figure 4.1 (b)).
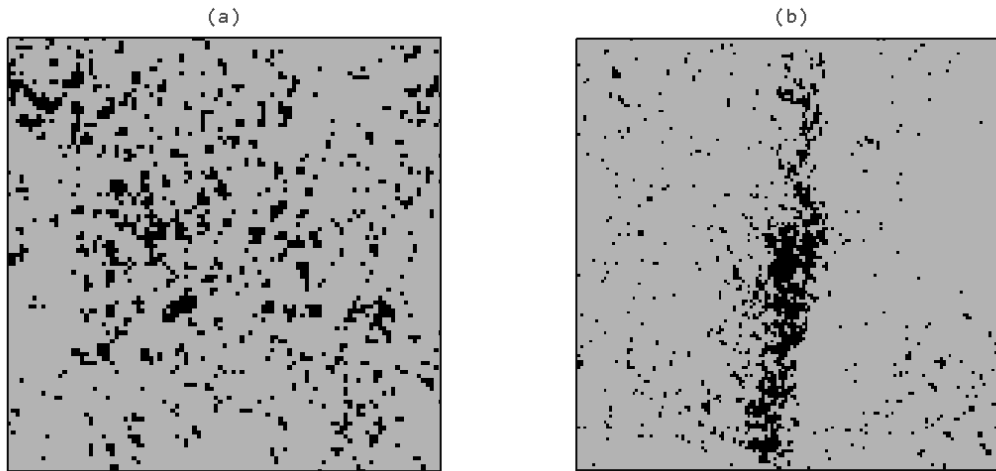
Figure 4.1 - Masks with the potential drops (black) which highlight the noise problems (*a*) and fragmentation (*b*).

To overcome the aforementioned problems, a step of pre-processing, which acts on the scene images, or post-processing, which acts on the output masks of the identification algorithms, is required.

In this Chapter we will analyze separately these two issues which are connected and, hence, the solution of the first can be in many cases of help for the other one. Furthermore, since the comparison between successive pictures (*j* with *j+1* and *j-1*) determines an average information loss equal to 10% due to the presence of drops in contiguous frames, in the following sections we will also describe and present the results of an alternative method for drop detection.

In particular, in the following we will re-analyze:

- background subtraction method;
- drops reconstruction through mono and bi-directional dilation filter;
- denoise through minimum intensity filter (Section 4.3.1);
- denoise through shape filter using fixed and adaptive threshold (Section 4.3.2);
- sequential drop detection (Section 4.4).

4.1   BACKGROUND SUBTRACTION METHOD

The method here proposed is based on the idea of drop identification by difference with the background using all the ten frames of each set, instead of only three (see Section 3.1). All the 10 pictures are taken in a few seconds time window. The method is based on the concept that each pixel bracket the

background, except for those pixel occupied by a drop. In Figure 4.2 we represent the typical behavior of the intensity *I*, with varying images *j*.
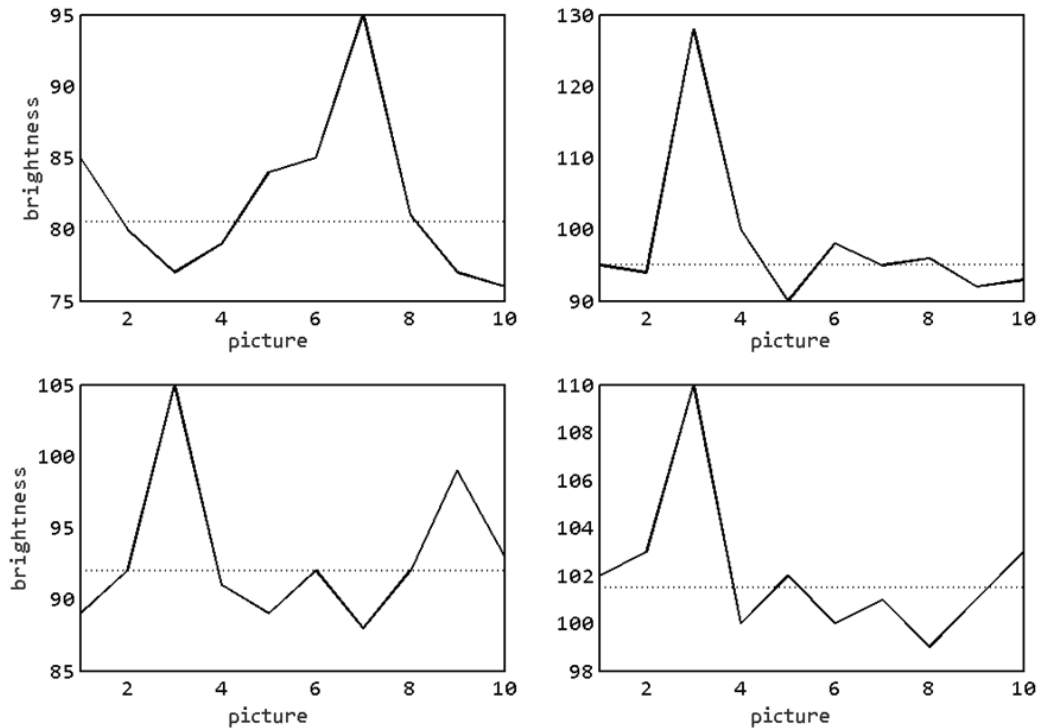
Figure 4.2 - Pattern of brightness for 4 pixels randomly chosen, for all the images (10) of a set. The peaks correspond to images in which the pixels delivers a drop. The median value is represented by the dotted line

Except slight variations due to changes in environment light or noise, the intensity values are almost constant. However, in those frame in which the pixel is crossed by a drop, the intensity *I* is significantly higher. Excluding these outliers is, hence, the way to reconstruct the background. The main steps of the method are explained in the following, including:

- identification of the ten pictures belonging to the set used to reconstruct the background;
- extraction of the ten values corresponding to the intensities of the pixels in the ten pictures;
- estimation of the median value. This statistic is useful to exclude outliers in each series;
- creation of a new image in which each pixel, is characterized by the median values obtained before. This image represents the scene background.

The method requires that the ten pictures are taken with the same shot. However, in case of minor differences, it is possible to use alignment algorithms to restore the view. In Figure 4.3(*a*) the background reconstruction as the median of a ten pictures set is shown. If a larger number of pictures were considered, the estimate would have been more accurate, but this would be too binding about the methodology which aim to give a real time estimation of the rain intensity. Moreover, using a larger number of frames, would lead to generation of gross error due to changes in light conditions.
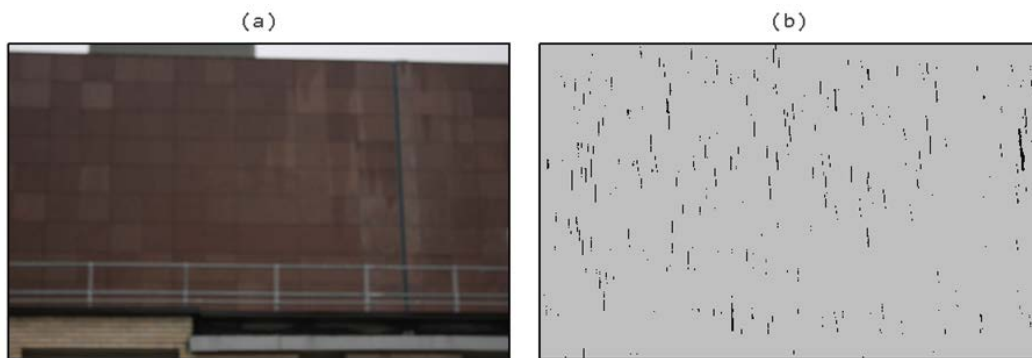
Figure 4.3 - (a) Pixel by pixel background estimation as the median of a ten pictures set.
(b) One of the ten subsequent masks, with $S_1=5$

If we call *BG* the image representing the background (Figure 4.3(*a*)) and *I(BG)* its intensity values, the pixels in the image *j-th* are then identified as drop (Figure 4.3(*b*)) if they meet the following condition:

$$I(j) - I(BG) > S_1 \qquad\qquad [4.1]$$

4.1.1   Comparison with the original method

Compared to the standard methodology, the background subtraction allows one to reduce the underestimation due to the drops that occupy the same area in subsequent frames. Moreover, since the procedure estimates the background just once for all the ten pictures set, the computational time is strongly reduced. In many cases, a lower sensitivity to noise and an improvement in the shape of drops is also observed.
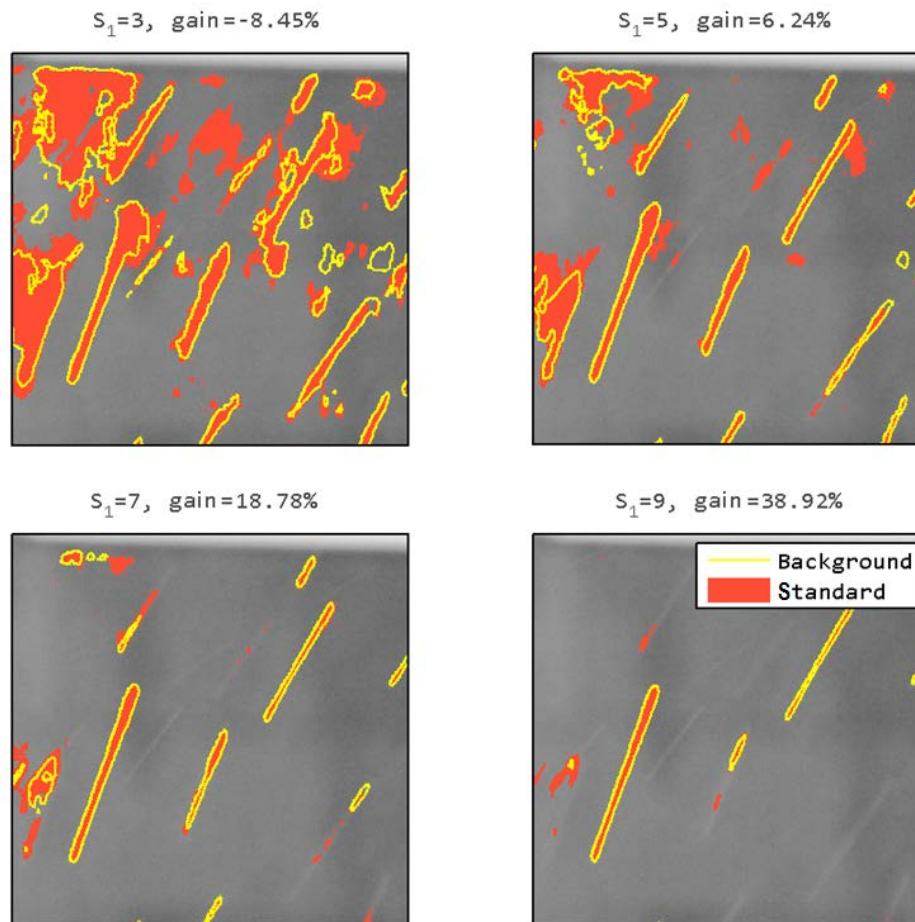
Figure 4.4 - Comparison between the standard and the background subtraction method for different sensitivity thresholds (3,5,7,9). For lower thresholds the background subtraction implies a loss of detected regions, probably due to lower noise sensitivity

In Figure 4.4 the results obtained with the background subtraction method and the standard method are shown. For every image the number of pixels detected by the two methodologies was calculated. The background subtraction method leads to a reduction of the total number of recorded pixels for low threshold values (eg., $S_1=3$). In fact, with low thresholds noise can be confused with signal, while the background subtraction method seems to be less sensitive to noise. With gradually higher thresholds, the proposed methodology leads to an increase of the detected pixels, due to the fact that the original method is affected by underestimation related to the presence of drops in the contiguous images. Both effects are certainly positive and lead to prefer, in the first analysis, this method to the previous one.

4.2   DROPS RECONSTRUCTION

If no filters are used many of the identified drops seems to be split or composed by fragmented components. To better evaluate the precipitation rate, the algorithm was implemented to consider each snippet as a drop in its own right. The proper diameters and terminal velocity are assigned to each drop. Due to intrinsic reasons, the total contribution of the snippets cannot be equal to the contribution of the fully identified drops. Hence, the tiny snippets are eliminated. To this purpose, noise reduction techniques (see Sections 4.3.1 and 4.3.2. See also Seo et al., 2007 and Gayathri et al., 2012 for more details on the topic) or a posteriori filters that exclude unlikely drops (see Sections 4.3.1 and 4.3.2) can be introduced in the algorithm.

Another way to solve the aforementioned problem consists in using the median filter, also useful for the noise reduction. The filter dimensions facilitate the reconstruction if they resemble those of the drop; specifically, it may be useful to use high filters other than wide ones. In this way, the intensities are mediated along the vertical direction.
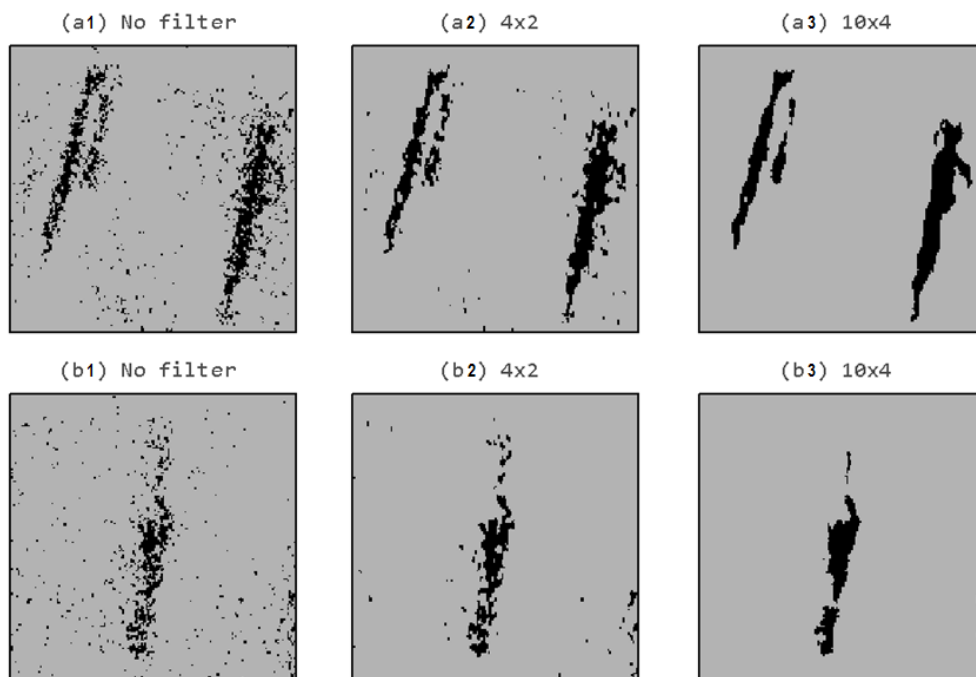

Figure 4.5 - Masks made by applying a $S_1=5$ threshold. Comparison between the original method (*a*1, *b*1) and the application of a small (*a*2, *b*2) and large (*a*3, *b*3) median filter to different images (*a* and *b* rows)

Figure 4.5 shows the masks obtained by applying the original method (Figure 4.5 (*a*1) and (*b*1)) and using median filters of different sizes (Figure 4.5 (*a*2-3) and (*b*2-3)). It is noted that for a good reconstruction of some drops it is necessary to apply very large filters (Figure 4.5 (*a*3)), while in other cases (Figure 4.5(*b*3)) increasing the size of the filter may result in the separation of the droplet into two or more fragments.

4.2.1   The 2D dilation filter

The dilation filter is part of the operations that modify the morphology of the forms of an image. In the specific case of a binary image, in which it is possible to identify the connected and isolated regions from the background, the filter has the effect of zooming in each region, extended its contour of a certain amount of pixels.

This filter is conceptually very similar to the median filter, in fact the intensity of each pixel in the filter depends on the intensity of the same pixels in the original image and the intensities of all the pixels around it (function of the filter dimensions):

- a matrix (called core or kernel) is first defined, whose dimensions determine the extent and intensity of the dilation in the final image;
- for each pixel, the intensity values of the neighboring pixels are extracted by using the kernel size. In the case of a 3×3 matrix, the reference set is formed by the pixel value of the investigated pixel and by the values of the 8 surrounding pixels;
- the maximum of the values of the just-sampled intensity-set are calculated. This corresponds to the correct value;
- the correct value is set for all pixels of interest in the filtered image;
- the operation is repeated on all the input image.

The algorithm has interesting implications when applied to binary images (0-1 images). In fact, the regions marked as potential drops (1) are dilated in all directions depending on the shape of the kernel matrix.

The dilation filter has proven effective in reconstructing the broken droplets, formed from a large number of small and independent regions: each region is enlarged, and this in fact binds it to the adjacent regions. Depending on the setting and on the identification of the drop, the result can be very similar to the original drop (as it is perceived by the eye). To do this, one needs to apply the filter in post-processing to the mask containing the drops identified by the drop-detection

algorithm. Figure 4.6(a) shows an unfiltered image with a compound drop and Figure 4.6(b) shows the same image filtered by a dilation rectangular filter.
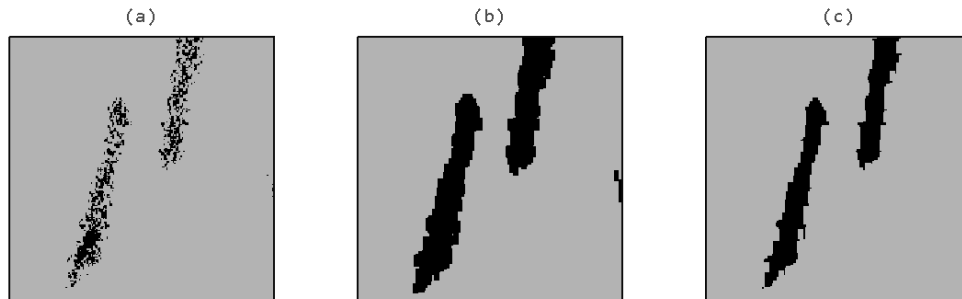

Figure 4.6 - (a) Original mask made from S_1=5. (b) filtered mask with filter dilation 8×4. (c) As (b) with 8x4 erosion filter

Since the size of the drops are enlarged compared to those perceived in the input image we apply to the image already dilated (Figure 4.6 (b)) a filter with the opposite effect, specifically, an erosion filter. It is identical to the dilation filter, but the intensity assigned to the pixels is the minimum of the values recorded in its neighborhood; the resulting effect is to streamline the forms on a binary images. After having applied the dilation (Figure 4.6 (b)) and the erosion (Figure 4.6 (c)), the shape of the drop is very similar to the desired one. In fact, the internal disconnections, once closed by the first filter, are not re-opened by the second one. However, it is necessary that the distance between the fragments is smaller than the extension of the filtering matrix.

It is noted that the filter should be applied to masks that have already been deprived of noise. Otherwise, each noise pixel can be enhanced by the expansion and expanded to become relevant. Another problem associated with this approach is the possible union (as a result of the dilation filter) of the drops of water which are instead disjoint.

4.2.2 The 1D dilation filter

The filter can be made more efficient by taking into account the fact that the drops, represented in their fall as streaks, have a preferential direction. In first approximation, this can be done using filters which are elongated on the vertical direction (higher than wide), assuming that streaks are vertical; it is true, however, that the wind can change the fall of the drops to an inclined direction. For this reason, we assume that all the streaks within the image have a common direction. To account for this effect, dilation filters whose structural elements are lines with a pre-defined inclination, instead of rectangular matrices, can be applied. The

shape of the structural elements (kernel) determines the neighborhood of the pixel to be considered at the time of the re-assignment of the intensity value. A linear structural element acts along segments of fixed length and orientation. For example, when dilating a black image (0), but with a white pixel (1) in its interior, this white pixel is extended to form an inclined segment which length depends on the structural parameters.

The idea is then to filter in post-processing the mask containing the fragmented drops with a linear scheme, whose inclination is obtained as the average direction that the drops have in the picture. A possible approach to the problem is the following:

- the droplet form is recovered through the identification procedures, possibly de-noising the image in post-processing;
- the mixture is filtered with an algorithm that reconstructs the fragmented droplets, even in a rough way by a median filter of large size;
- the average (or the median) slope α of the resulting droplets is determined;
- a dilation directional filter with α inclination angle is applied to the initial image. The extension, i.e. the length of the segment, has to be calibrated.

In Figure 4.7 the results are shown. To avoid that the expansion influences the perceived length, an erosion filter with the same extension parameters and the same inclination α is applied a posteriori.

Compared to the rectangular dilation (see Section 4.2.1) filter, it is observed that in this case it is possible to go towards more extension without particular aberrations in the result and fragments of very distant drops can be joined together. The directionality of the filter also reduces the problem of unwanted unions between adjacent droplets, which characterizes the rectangular dilation filter. The efficacy of the operation, by contrast, decreases for drops whose inclination is very different from the average inclination.


Figure 4.7 - (a) Original mask made from $S_1=5$. (b) Filtered mask with large directional filter with l=15 pixels. (c) The previous picture after application of an erosion filter of the same size

Figure 4.8 shows a comparison between the three main reconstruction techniques analyzed: the median filter, the rectangular filter and the directional expansion. The advantage of the latter is in the length of the structural elements; for pictures captured at 18 megapixels one can apply directional filters with l=35 pixels without major negative consequences, while it would be deleterious to use 35×35 matrix (or similar) in the first two cases.
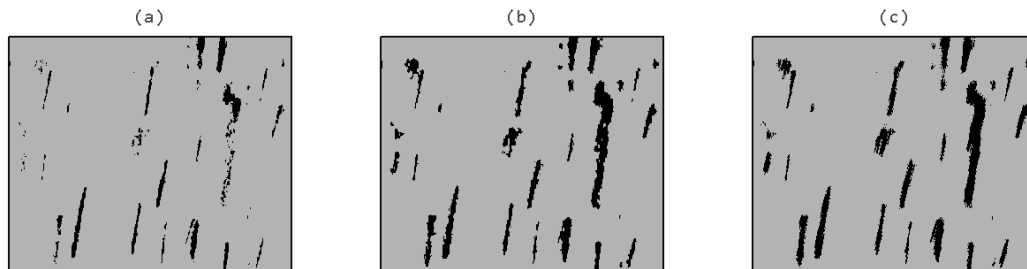

Figure 4.8 - Masks from S_1=5, de-noised and then treated: (a) with the median filter 15×10; (b) with the dilation filter 8×4 followed by the erosion filter; (c) with the directional expansion filter, with l=35 pixels, followed by the erosion filter

4.3 DENOISE

The drop detection methods produce a binary image (or mask) as a result, that highlights the drops on the scene, eventually cleared by the noise and free of fragmentation. IR² is now expected to analyze each drop and determine its diameter, length, speed, position; finally, the contribution in terms of precipitation intensity (mm/h) can be estimated.

Before proceeding, however, it is useful to study the identified drops to highlight possible further problems. Specifically, it is possible to observe unlikely drops:

- for their form: the identification algorithm, especially with low thresholds, can extract very irregular shapes that have no meaning from the physical point of view, and are not attributable to drops. True drops that crossed the scene are hidden behind these forms. However, we must not keep these droplets as such, because the next steps would assign them fictitious diameters and lengths;
- for their size: too small or too large. In the process of speed estimation, IR² already takes into account the exclusion of drops larger than 6mm, the limit beyond which they tend to separate, and drops smaller than half a pixel, the characteristic that practically makes them invisible to the camera. It is thus sensible to remove these drops before they are analyzed, to improve computation efficiency.

Excluding non-behavioral drops has two benefits. On the one hand, it is possible that the filtering has positive effects on precipitation intensity estimate, making it more accurate; on the other hand, the filtering reduces the total number of droplets to be analyzed and makes the subsequent operations less onerous from a computational point of view. The timely execution of the estimate is a key parameter to IRR, considering the high temporal resolution needed.

This section covers the possible criteria under which to select or exclude the potentially false drops (PFD) from the set of drops that will be analyzed. The presence or absence of the PFD depends on the identification method and its parameters. In the following, unless otherwise indicated, we will refer to masks:

- obtained with the IR^2 method;
- processed with a median filter 5×3 for a surface noise reduction;
- non-treated for the fragmentation of the regions.

4.3.1   Denoise through minimum intensity filter

Many PFD, be they true drops or artifacts generated by the picture noise, do not significantly contribute to the final result in terms of precipitation intensity, which is calculated by the equation [10] as the sum of the contributions of the individual drops. While not influencing the result, these PFD negatively affect the calculation procedure making it slower than necessary.

We aim at identifying the PFD in advance to avoid unnecessarily calculations. Strictly speaking, this is impossible, because in order to define an insignificant drop one must first determine its contribution, which is precisely the task we would like to avoid since it has a computational burden. However, it is possible to calculate the contribution of each PFD in an approximate manner.

The main issue lies in cleaning up the diameter and vertical length (in pixel) of the blur component, $c_P(z)$, and convert the resulting values, D_p and L_p, in millimeter. In fact, $c_P(z)$ and $d_P(z)$ require knowledge of the distance from the lens, z, which is not a priori known and is the most complex step from the methodological point of view, because it identifies a third dimension not present in the two-dimensional image. To estimate z it is necessary to solve a quadratic equation under various assumptions and choose a solution among the four possible solutions.

The filtering criterium presented here circumvents the problem of the third dimension by calculating in advance the contribution of each drop as if it were placed at a known distance equal to two times the distance from the plane of

focus, z_0, which is the distance that maximize the drop contribution. This distance corresponds to the bottom of the sampling volume, the truncated pyramid wherein drops are visible. For droplets placed at z = 2z_0:

- the conversion factor $d_P(z)$ is maximum because the distance from the chosen lens is the maximum possible;
- the diameter of the circle of confusion $c_P(z)$ is easily calculated and this facilitates the intensity estimation from the computational point of view.

Under these conditions, it is safe to discard the PFD that, even if they were placed at the distance that maximizes the contribution, do not contribute significantly to rainfall intensity. The contribution of each droplet is estimated by assuming that it travels at its terminal velocity.

It can be assumed that the resulting contribution is the maximum that a drop of that size can provide, thus excluding the PFD whose contribution does not exceed a minimum threshold in terms of rainfall intensity ($i_{lim} = 10^{-4}$ mm/h). These PFD would impact marginally on the result, but would significantly slow down the procedure. The remaining drops are then analyzed according to the original method, i.e. by searching their position in the z space and their actual contribution.

Figure 4.9 shows the results of the filter application. We observe that a significant reduction of the number of drops does not imply any loss of accuracy. For example, with $S_1 = 4$ the MAPE is 0.3 both with and without the filter, while the number of drops decreases from $2.5 \cdot 10^4$ to 10^3.
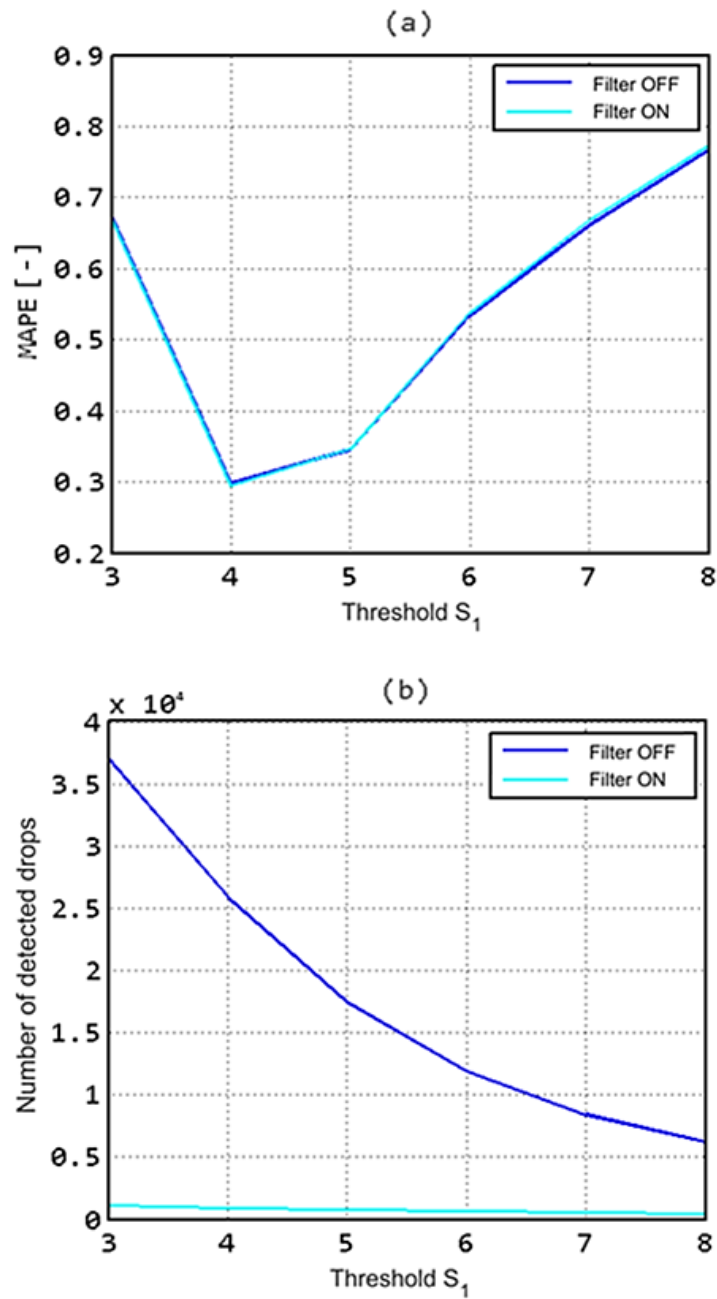
Figure 4.9 - Comparison between the applications of the method with and without selection for the intensity contribution. It is shown (a) the mean absolute error on the rain rate measure and (b) the average number of detected drops as a functions of the threshold S_1

4.3.2   Denoise through shape filter

Another parameter that can potentially separate the drops of irregular contours is the concavity. We expect that clearly identified droplets present themselves as convex strips, without indentations (Figure 4.10(a)); conversely, artifacts, noise and clusters of droplets exhibit concavity (Figure 4.10(b)).
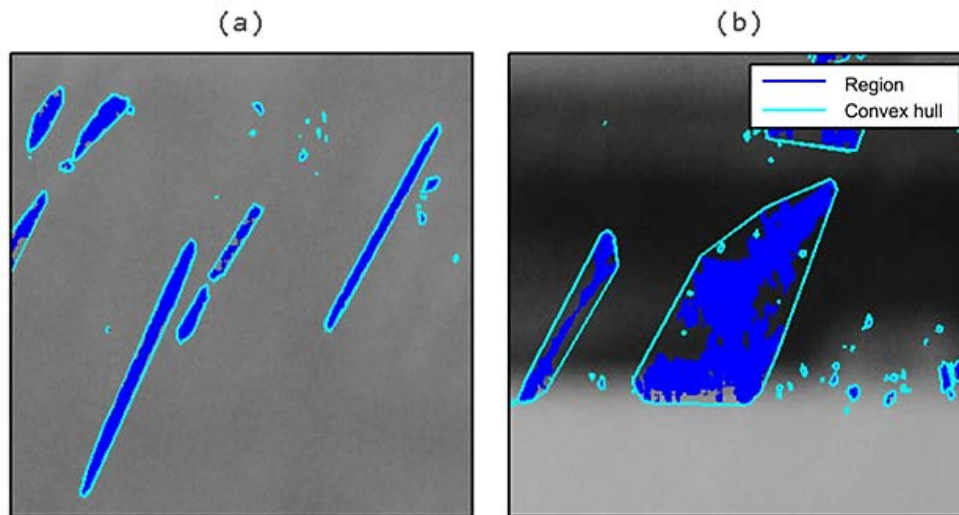

Figure 4.10 - Very regular (a) and irregular regions (b), surrounded by their convex hull

To highlight the concavity of a region a geometric instrument called convex hull is useful. It represents the smallest convex set that contains each region. Note that for convex regions, the envelope coincides with the region itself. Otherwise, for regions with concavity, the envelope occupies a larger area. Figure 4.10 shows how more concave regions, such as droplets with irregular contours and recesses, have significantly smaller area than the area of their convex hull; viceversa regular regions, such as well-identified drops, have an area which practically coincides with that of the envelope. Hence, it is possible to numerically quantify the convexity or concavity of a region and the parameter that can quantify this kind of irregularities is the ratio of the area of the region (drop or presumed drop) to the area of its convex envelope, $r = A_r/A_i$. r is between 0 and 1: it tends to 1 in case of convex regions; it tends to 0 for very irregular regions. Through r it is hence possible to quantify the tendency of a region to the concavity or the convexity.

4.3.2.1 Fixed threshold

We define a threshold, r_S, such that the drops with $r < r_S$ are excluded (Figure 4.11).
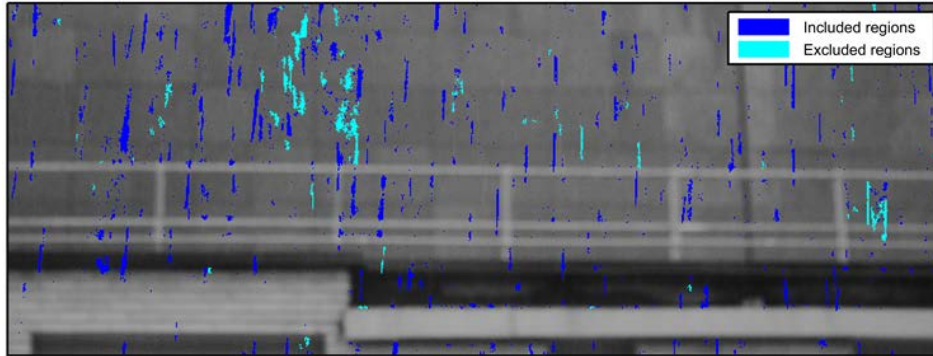

Figure 4.11 - Masks with S$_1$=5, with included and excluded regions due to the application of a threshold $r_s = 0.6$

The obtained results strongly depend on the threshold, r_S, and from the recognition threshold S_1. Note that they also depend on the image processing algorithms performed on the image itself.

The droplets reconstruction has a great influence on the best threshold, r_S, to be used: if the fragments were joined, the drops are in media more convex and approaching $r = 1$; in the other case, the fragmented drops are much more irregular and tend to lower r and, hence, a non-adequate r_S threshold could discard all the drops.

The results in Figure 4.12 show that the selection does not have a particularly beneficial effect on the number of drops (*b*) to be analyzed; at the same time it slightly improves the accuracy of the method on some S_1 thresholds (*a*). The data presented, however, is qualitative: in fact, the improvement may be sensitive to the calibration of the r_S parameter.
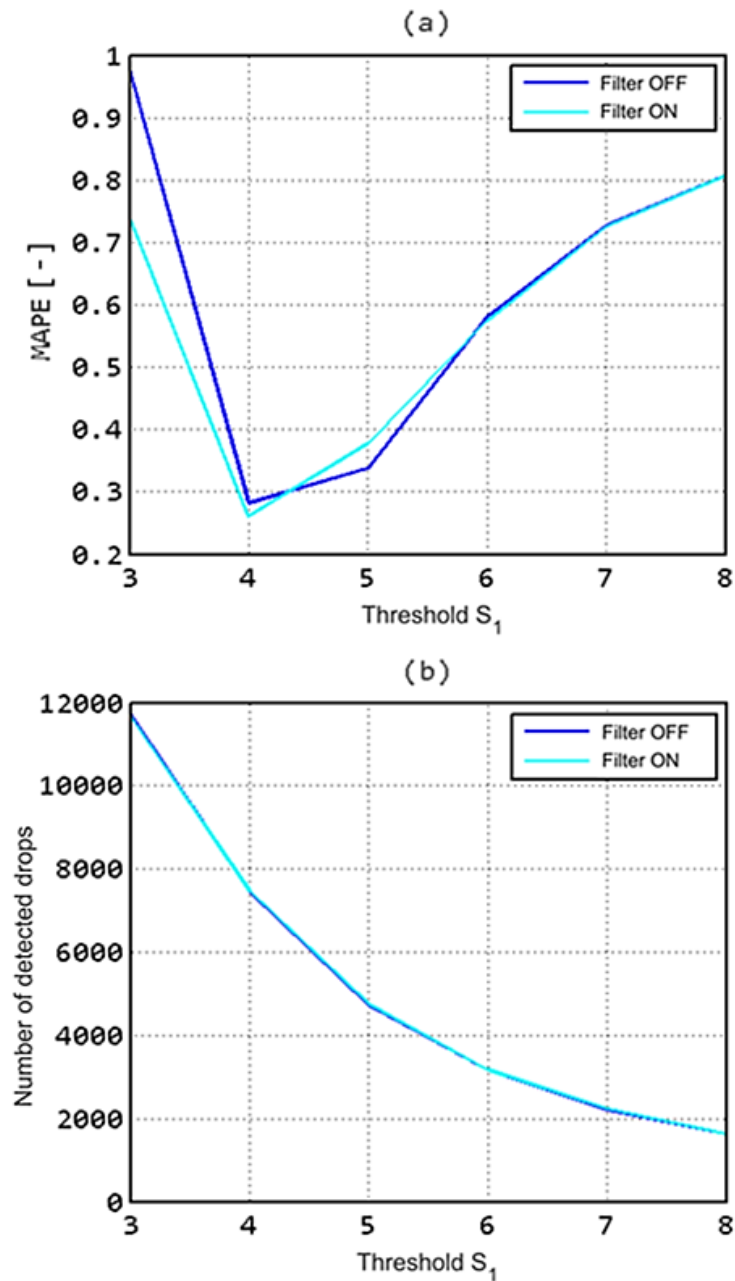
Figure 4.12 - Comparison between the applications of the method with and without filter for convexity with fixed threshold, $r_s = 0.45$. They show (a) the mean absolute error, and (b) the average number of drops detected, as a function of the sensitivity

4.3.2.2   Selection with adaptive threshold

The above-described selection criterium can be improved. In primis, r_S should be adapted to the identification sensitivity, quantified by S_1. Specifically, if the

identification with low S_1 values, drops (including the real ones) tend to be more irregular, and it would be appropriate relaxing r_S to avoid eliminating too many drops; if the identification is more selective (high S_1) the drops are better defined and regular and, therefore, r_S may be more restrictive. The regularity of drops distributions is also affected by the extent of the precipitation. In fact, the algorithm identifies generally well-defined drops in situations of light rain, while regions are noisier and more agglomerates of adjacent drops are seen in case of higher intensity. The average value of r in the masks depends on external factors of different nature and this makes it difficult to find r_S values that work well in all cases.

In this regard, we tested the use of adaptive thresholds, both with respect to the identification sensitivity and the intensity of the rain. To adapt r_S to the image corresponds to using a percentage approach, i.e. defining the parameter q, the percentage of regions that will be discarded in any single image according to their convexity ratio r. More in details, the steps include:

- to analyze the image with a given threshold of sensitivity S_1 and to identify the possible drops;
- to determine for each drop its convexity ratio r;
- to determine the frequency distribution of r in the image;
- to determine r_S as the q-th quantile, that is the threshold which separates the fraction q of less regular drops from the fraction $1 - q$ of more regular drops;
- to exclude the drops with $r > r_S$.

Since the drops tend to be more irregular for high rainfall intensity, it is observed that r_S varies as a function of the identification sensitivity and of the image type (Figure 4.13). The distributions, and therefore the most appropriate q value to obtain a certain r_S, are strongly influenced by the presence of noise that occurs as agglomerates of a few pixels, mostly very regular, without concavity, and that are grouped in correspondence of $r \cong 1$. In the absence of a good cleaning algorithm, noise particles can become dominant over the other, invalidating the selection criterion. In conclusion, the method gives good results with regard to improving accuracy, limited to certain thresholds S_1 (Figure 4.14). The effect is more evident if comparing the results with the previous criterion, wherein the r_S threshold is fixed a priori.
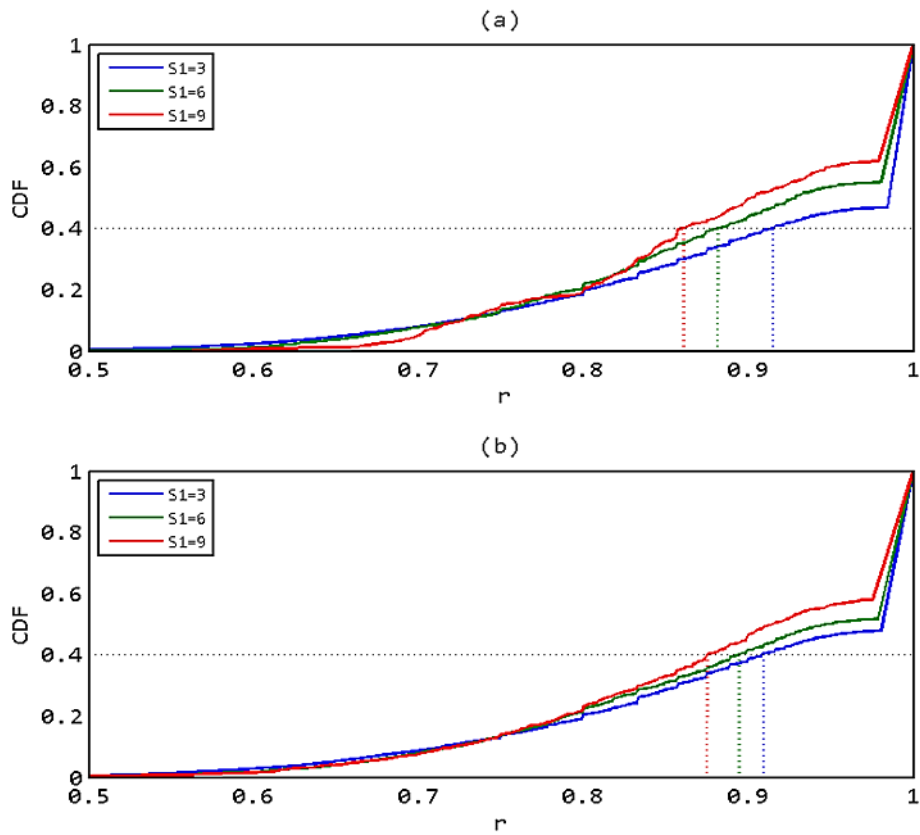
Figure 4.13 - Cumulative Distribution Function of the convexity ratio *r* for images (a) in low-light conditions and (b) intense precipitation, for different thresholds of sensitivity S_1. The *q*-th quantile varies with the threshold S_1 and the image type
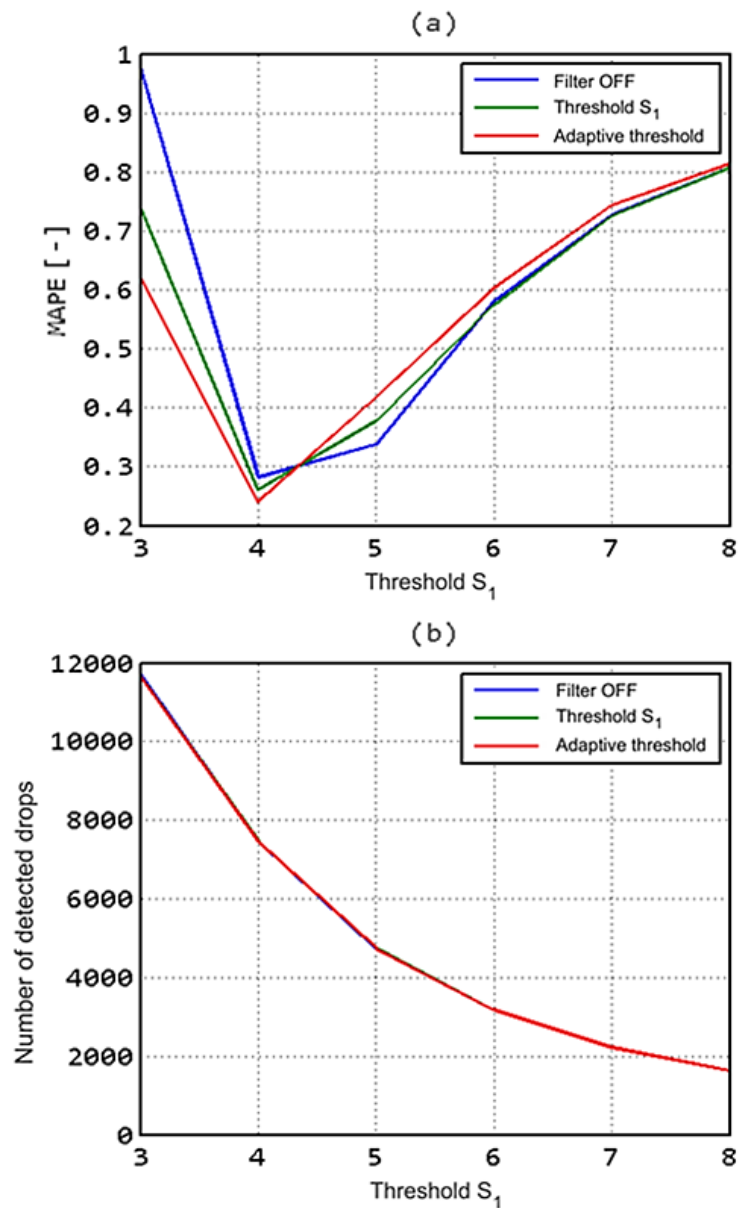
Figure 4.14 - Comparison between the applications of the method with fixed threshold filter ($r_s = 0.45$), and with adaptive threshold filter ($q = 0.005$). (a) the mean absolute percentage error and (b) the average number of drops detected, depending on the sensitivity

4.4 SEQUENTIAL DROP DETECTION

In the previous sections we have seen which criteria one should adopt to select the most irregular regions and exclude them from the processing. However, the

appearance of a region strongly depends on the sensitivity of the identification method, quantified by S_1: in fact, less selective identification procedures (lower thresholds) tend to produce an higher number of drops but many irregular drops, while higher thresholds tend to detect few regular drops. In general, we observed that:

- low thresholds capture well the least noticeable drops, very similar to the background, but disturbs the shape of the most clear drops;
- higher thresholds, corresponding to a lower sensitivity, capture well the most clear drops, but ignore the other.

The most obvious solution is to seek a compromise, such as a S_1 threshold that captures a good number of drops with regular appearance. The less regular drops, then, can be excluded with a posteriori filters. This approach has two negative consequences:

- it neglects the less visible drops, which may be identified by raising sensitivity ($S < S_1$);
- it accepts very irregular drops, which could be better identified by decreasing the sensitivity ($S > S_1$).

In particular, the exclusion is deleterious because it also acts on agglomerates of drops, which in higher thresholds are seen as distinct and regular drops. In Figure 4.15, for example, $S_1 = 9$ returns drops that in $S_1 = 3$ would be irregular, while the latter, being more sensitive, returns drops that in $S_1 = 9$ are absent. Excluding irregular regions in low thresholds neglects drops that for higher thresholds are well defined.
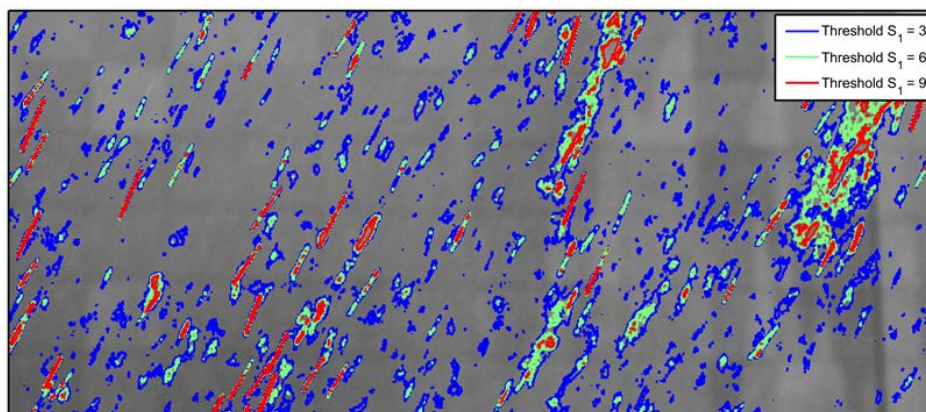

Figure 4.15 - Advantages and disadvantages of different sensitivity thresholds. With low threshold, many irregular drops are seen; with high thresholds, fewer very regular droplets are detected

Reasoning in the reverse sense, the regularity of a region provides information on the best sensitivity needed to identify the corresponding drop. This can be useful for an identification method that exploits regions that came from all the sensitivity thresholds rather than trying to find a compromise. The idea is hence to collect from each threshold the drops it better identifies, that is, the more regular ones. We proceed as the steps below:

- starting with a very sensitive threshold (e.g., $S_1 = 3$) the highest number of drops is detected;
- among the identified drops, the most regular ones are selected, stored into a drop database and deleted from the image;
- the remaining irregular regions are excluded, but, instead of completely discarding them, they are re-analyzed with a slightly less sensitive threshold (e.g., $S_1 = 4$);
- a new set of drops is obtained; the most regular ones, as described before, are stored and deleted from the image, while all the irregular ones are processed again with a less sensitive threshold;
- the process continues iteratively unless the highest threshold is reached (e.g., $S_1 = 10$).

This procedure allows one to extract the best from each sensitivity threshold, avoiding overlapping and producing a consistent final set. The regularity criterion used to analyze the drops and determine their acceptability can be the convexity ratio r, calculated as the ratio between the area of the region and the area of its convex hull.

The result is an image that does not depend on S_1, which collects regions from all sensitivity thresholds. By applying this procedure, the identification method is somehow unrelated to S_1 (except for the minimum and maximum thresholds) but depends on a new parameter that is the convexity ratio r.
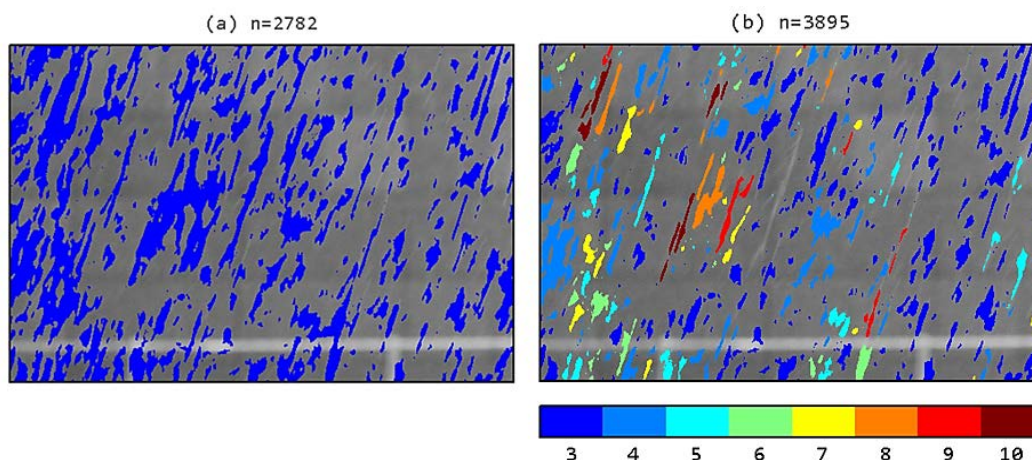
Figure 4.16 - Final masks and total number of drops n. (*a*) Image investigated with $S_1 = 3$. (*b*) Image investigated with sequential method with fixed threshold ($r_s = 0.45$) between the sensitivity $S_1 = 3$ and $S_1 = 3$

Figure 4.16 shows a classical acquisition with threshold $S_1 = 3$ and the same image processed by the described iterative method (in the following called as sequential drop detection) by collecting the best drops for each cycle and investigating the others in the subsequent thresholds. On the one hand, the method captures the least visible regions (thanks to the contribution of the lowest and most sensitive thresholds); on the other hand, separates overlapped drops in their components (thanks to the highest and less sensitive thresholds).

The possible selection approaches are:

- choosing a fixed threshold r_s, so that drops with $r > r_s$ are accepted and stored, while the remaining ones are observed at higher thresholds;
- an adaptive threshold is used, defining the percentage q of drops that, for a certain picture and for a given threshold, should be investigated at higher thresholds because are presumably irregular.

In both cases, the method is dependent on a single parameter, r_s or q, replacing the original parameter S_1. The adaptive threshold, as described above, allows to adapt the threshold of irregularity to the features of the analyzed image, to the precipitation intensity captured, to light conditions and to the sensitivity threshold S_1.

Figure 4.17 describes the dynamics of the sequential method by setting the adaptive threshold $q = 0.5$, starting from the threshold $S_1 = 3$, and investigating step by step six thresholds (from $S_1 = 3$ to $S_1 = 8$). Each graph represents the cumulative distribution of parameter r of all the detected drops. Increasing the

threshold makes the drops excluded from the previous step much more regular at the new step and we can always detect a sub-sample of acceptable drops.

Applying the sequential method, each threshold S_1 contributes to the final result. In particular, the lower thresholds have a greater impact on both number of drops and rainfall estimation as Figure 4.18(a) and Figure 4.18(b) show. An important aspect is that the contribution of higher thresholds is not negligible for both number of drops and rain rate.
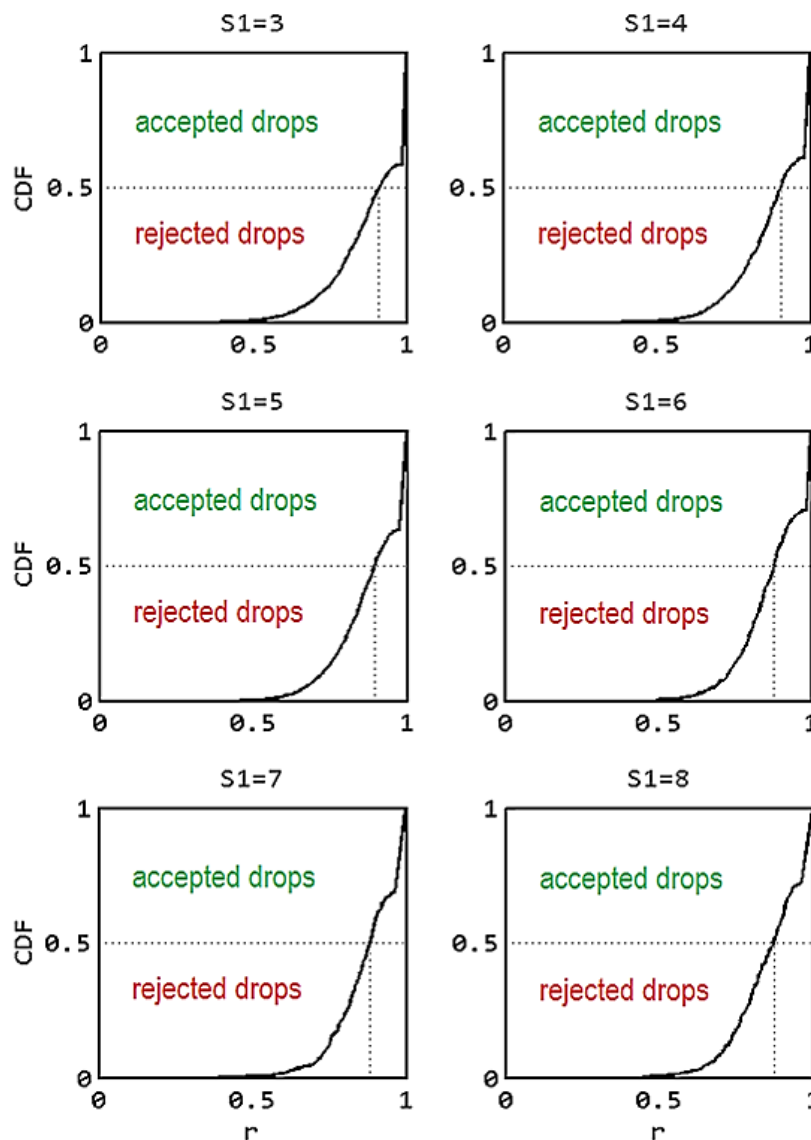

Figure 4.17 - Cumulative Distribution Function of the convexity ratio *r* during iterations of the sequential method. The dotted line indicates the *q* value and the corresponding threshold r_s as the intersection between the CDF and the *q* value. As the algorithm

proceeds, a percentage of the drops rejected with a threshold become acceptable analyzing the image with a new threshold
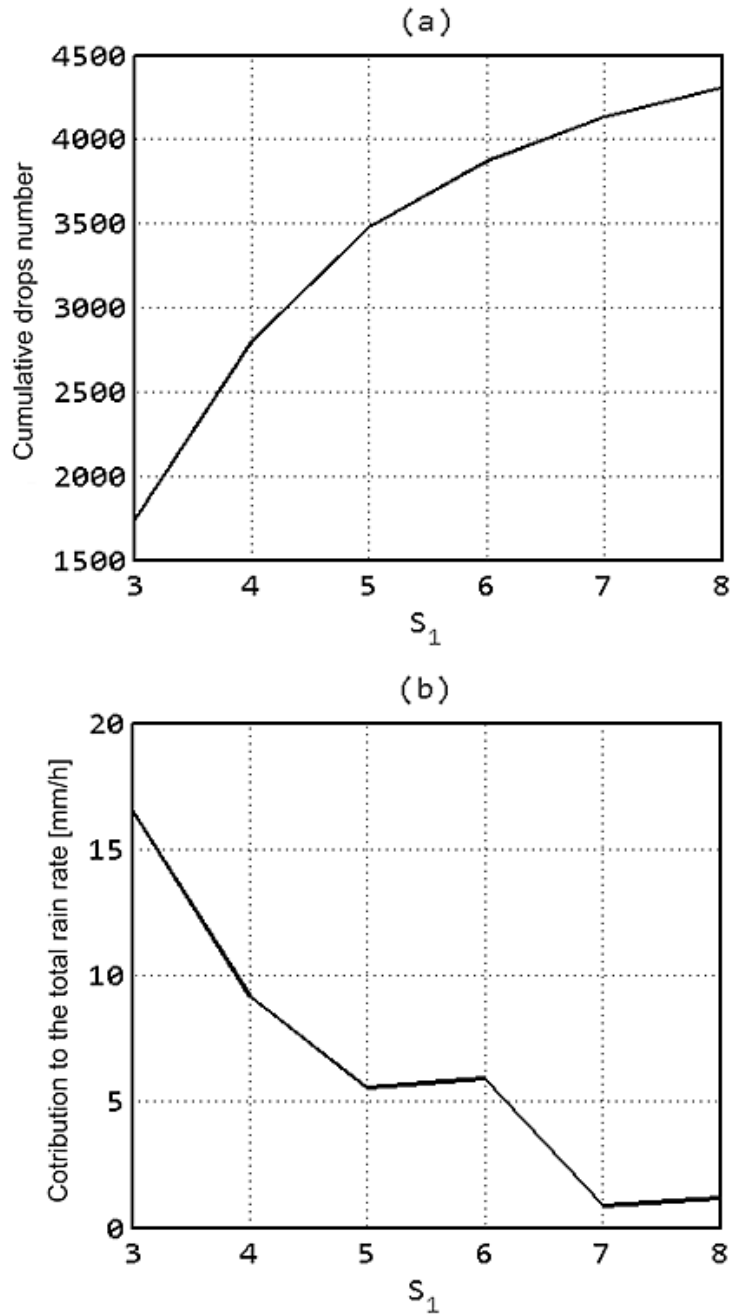
Figure 4.18 - Contributions of each threshold during the iterations of the sequential method. (*a*) Cumulative frequency distribution of the number of droplets accepted. (*b*) Contributions to the intensity of drops associated with each threshold

4.5   DISCUSSION

In this Chapter, some possible improvements to the IR^2 method algorithms were considered in order to enhance the accuracy of the method itself and, at the same time, trying to reduce the time required for processing. These modifications are introduced at different steps of the procedure, which in any case keeps intact its methodological bases (Chapter 3). In each one of the previous procedures, in fact:

- the instrument allows one to get a measure for each pictures, taking advantage of information from photographs taken immediately before or after;
- the shorter measure involves the acquisition of a set of 10 images that help to identify drops and reduce the estimation uncertainty: the final measurement is the average of the 10 measurements individually obtained from each photo;
- it is necessary, with more or less elaborate methods (Chapter 3.1 and Chapter 4), to identify the drops represented in each image, that is to produce a binary image, the mask in which the values 1 identify pixels that frame a drop, and the values 0 identify background pixels;
- the mask and the starting images are treated using image processing algorithms in order to reduce the effect of noise, fragmentation of the drops, etc.;
- the drops are analyzed one by one from a geometric and cinematic point of view by looking for the balance between the conditions established by the camera's optics and the speed of the drop itself;
- the sampling volume surveyed by the photographs has the shape of a pyramid trunk;
- the rain rate estimation referring to each image is the sum of the contribution of all drops detected in the analyzed image.

The investigated changes are different in character, sometimes they are methodological, sometimes purely computational and, as we saw, do not necessarily lead to an accuracy improvement.

4.5.1   The best configuration

As a result of the procedures described in the previous Chapters, we have chosen to apply the solution that has demonstrated the best performance in terms of the ratio between computational costs and improved estimation accuracy to a continuous series of photographs. Chapter 5 will detail this application, which will be characterized by the following settings:

- subtraction of the median background (Section 4.1);
- denoise with a median filter (Section 4.2);
- identification of drops with sequential procedure (Section 4.4);
- drop selection based on minimum intensity contribution (Section 4.3.1).

By adopting the sequential detection method, the convex filtering concept described in Chapter 4.4 enters in the droplet identification phase.

Briefly, the sequential identification consider to extend iteratively to all sensitivity thresholds S_1 (in the assessment phase from $S_{1,start} = 3$ to $S_{1,end} = S_{1,start} + 7$) and extract from each threshold the drops considered acceptable by their convex ratio r (see Section 4.3.2). The drops selected by each threshold are then collected to compose the final mask, which contains every real drop in its best possible representation (i.e. framed by the most appropriate sensitivity threshold). The parameter to determine the goodness of a detected drop is the coefficient q that, as described in Section 4.3.2.2 and 4.4 represent the percentile of detected drops considered as not acceptable. The value of q is a priori fixed, but the corresponding r_S convexity threshold varies with the image quality, the scene luminosity, the threshold of sensitivity and with the precipitation conditions.

The result in Figure 4.19 are no longer dependent on the sensitivity threshold, which is absorbed in the iteration phase, but only by the parameter q. The optimal parameter, for the analyzed sample is $q = 0.7$ and gives an average accuracy of 46%. This value is calculated on an extended sample (with respect to the one described in Figure 3.11), excluding the darkest images characterized by an average brightness smaller than 90 but not by putting any constraint on the camera parameters. This way, the considered sample is composed of 64 minutes versus the 20 minutes of Figure 3.11 one.
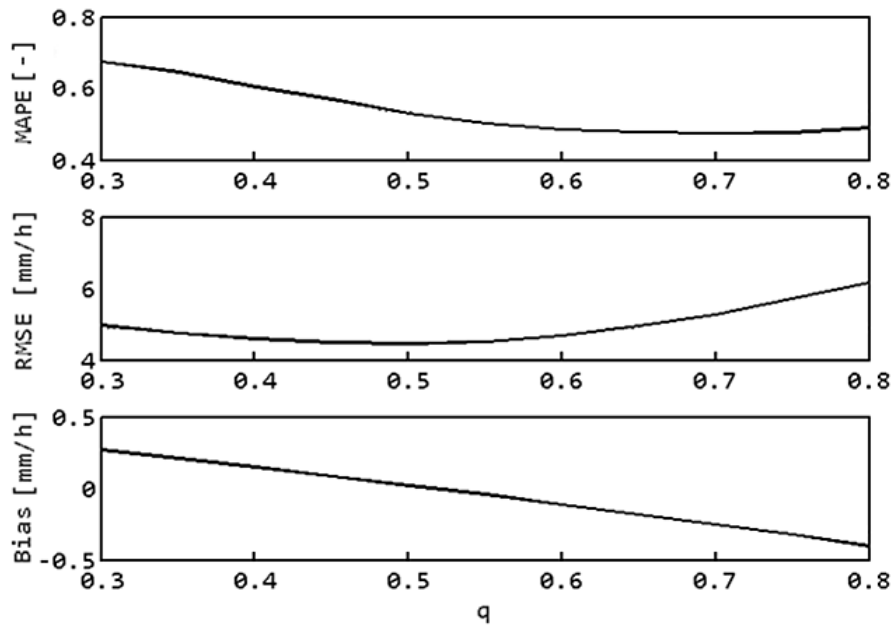
Figure 4.19 – MAPE, RMSE and Bias respect to the *q* parameter
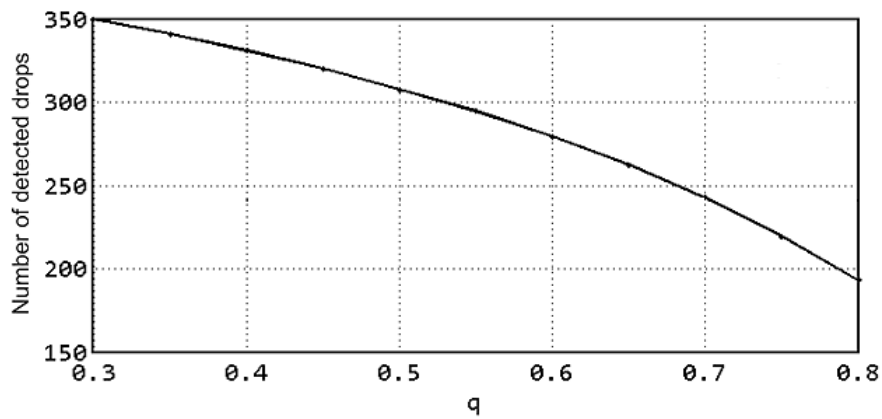
Figure 4.20 - Number of detected drops, as a function of the sensitivity parameter *q* in the best configuration

Chapter 5

Extended validation

Based on the analysis described in the previous Chapters, the method that appeared to be more effective both in terms of computational burden and accuracy of the rain rate estimation, is the standard method with some improvement. These changes concern the background subtraction, which is now made by subtracting a median reference image to the analyzed image, the presence of a minimum intensity filter to delete smallest droplets and noise and the selection of the drops using the application of sequential thresholds with an acceptance value of 70% (see Section 4.5). Once these methodological choices have been made, the procedure has been applied to a series of data coming from a multisensorial station that was installed on the roof of the Laboratory of Hydraulics of the Politecnico di Torino.

In this application, as previously done with the variations to the method described in Chapter 4, we focus our attention on the estimation of rainfall intensity (on a one minute time interval) to the detriment of the drop size distribution. The rationale for this choice lies in the creation of WaterView, start-up and spin-off of the Politecnico di Torino. This company started a commercialization process of the products described in the present work, and in order to do so required to focus on those aspects that were more relevant from a marketing perspective. The reasons behind the creation of the company, together with a description of the work done by its founders with the support of the Politecnico di Torino and of the Polytechnic's Incubatore di Imprese Innovative (I3P), can be found in Chapter 6.4.

The station is made up by a unit for the control of the different instruments, which are a Raspberry Pi board, a reflex camera, a camera module Raspberry Pi, and a Davis rain gauge (see Figure 5.1). The three sensors recorded continuously from May 15th, 2016, and the data analyzed refer to the time span spreading from May 15th 2016 to February 15th 2017. The data collected have been saved on a cloud, to allow a quick access, while the pictures and a backup of all the data are saved on an hard disk linked to the control unit.
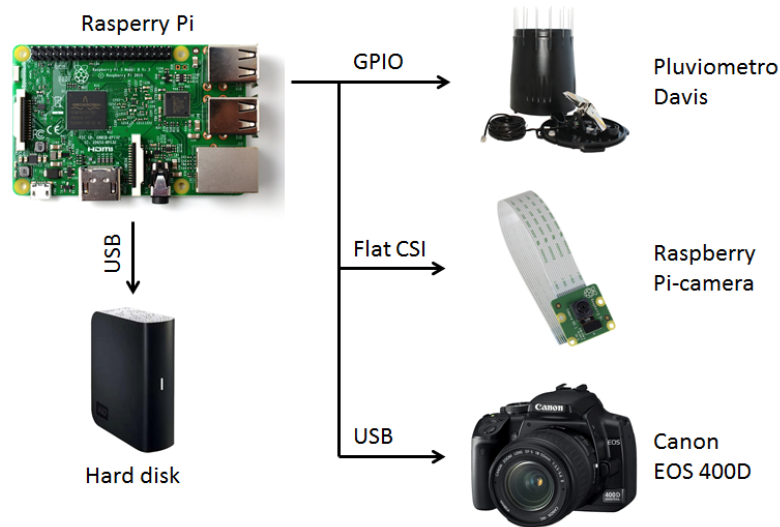
Figure 5.1 - Framework of the functioning of a measurement station

In its final configuration, the instruments listed above have been inserted inside a protective metallic box, as shown in Figure 5.2. Figure 5.2 and Figure 5.3 highlight the presence of a halogen headlamp used for a preliminary analysis of the interaction between punctual light and rain visibility. These studies will not be presented as part of the present research work, but will be part of future developments. In the same way, images and results deriving from the pictures acquired via the camera module Raspberry will not be discussed in this thesis.
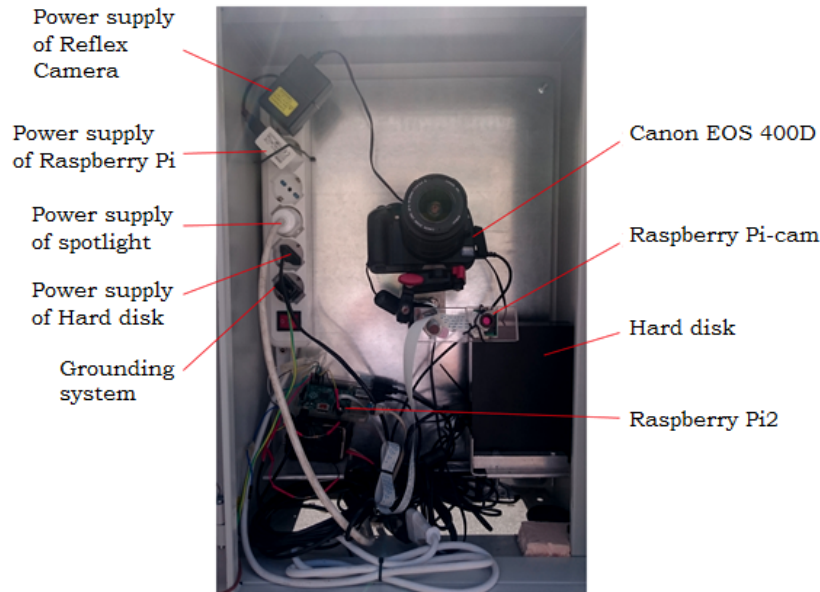
Figure 5.2 - Inside of an assembled measurement station

Figure 5.3 - A scene framed by the Reflex camera. The presence of the headlamp allowed to take pictures during night time, therefore helping in the development of a technology similar to the one described in this thesis, but which can be applied to low light conditions

5.1 THE CONTROL UNIT

The task of managing and controlling the station has been entrusted to the Raspberry Pi2, a small computer single-board (85 x 56 mm) with an elevated calculating potential and the possibility of having multiple connections to different types of sensors, thanks to an input/output interface called GPIO (i.e.,

General Purpose Input/Output). The board is also characterized by extremely low energy consumption, which allows a non-stop functioning even without any cool-down system as in other computers. The board has been created to support softwares based on Kernel Linux. More specifically, the distribution used for the Raspberry Pi is called Raspian.

The main characteristics of the Raspberry Pi are listed below:

- CPU: 900 MHz quad-core ARM Cortex.A7;
- RAM: 1 Gigabyte;
- USB 2.0 ports: 4;
- IN/OUT ports: 40 GPIO;
- Power source: 5V, 800mA.
- Memory: micro SD.

The advantages of these type of boards lie in their being extremely cheap, with an interface that can easily work with several instruments, and very common. The last aspect is what allows vast communities of developers and enthusiasts who, by sharing their own experiences, play a role in helping develop the desired applications.

In the next section, the connections between Raspberry Pi and the different peripheral devices linked to it will be described and defined, to explain the functioning and the management of the central unit.

5.2 THE BENCHMARK: DAVIS RAIN GAUGE

The rain gauge and the Raspberry are linked through the RJ-14 wire, which comes with the instrument itself. The central unit will need to constantly analyze the logic signal input by the rain gauge, and record in a log file the time and date of each oscillation recording, which means each time the weighbridge swings over the Reed switch. The log file will have as many rows as the number of oscillations registered, and for each row there will be the date related to each swinging.

Based on the information in the log file, rain intensity will be estimated, by imposing that the rainfall intensity between two consecutive oscillations is constant. Based on this principle, the intensity between each oscillation pair will be calculated simply by dividing the data that represents the amount of water millimeters in the bucket (i.e., 0.2 mm, as per the instrument datasheet) for the amount of time between one oscillation and the previous one.

Based on this temporal irregular diagram, the average rainfall intensity per minute will then be calculated, based on evenly spaced 1-minute timespan. Figure 5.4 describeS the estimate procedure of intensity per minute.
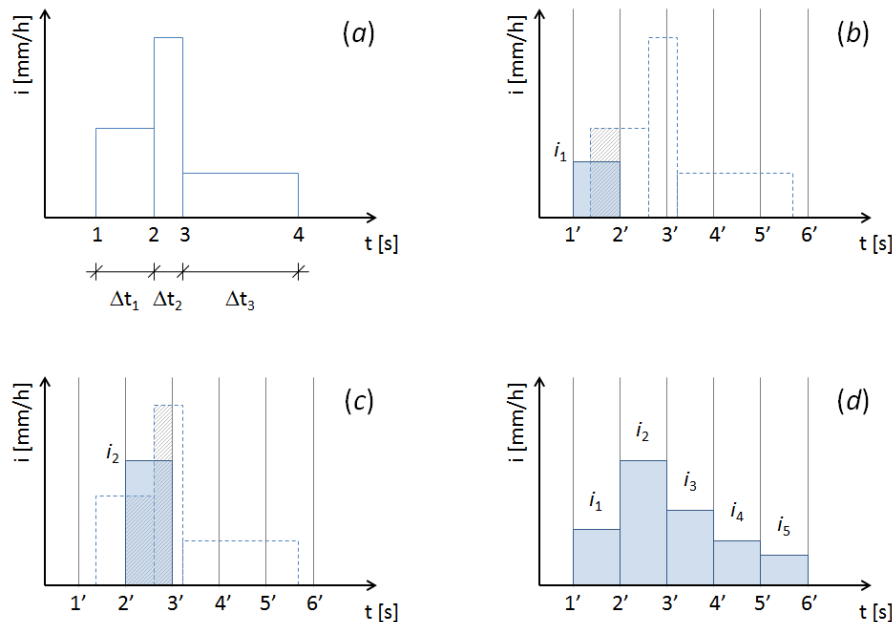

Figure 5.4 - Representation of the phases of determination for the rainfall intensity per minute, based on the temporal information for each oscillation. (*a*) definition of the intensity of the rain for each: i(t) = 0.2/Δt mm/h; (*b, c*) division of the timespan in evenly spaced 1-minute intervals and calculation of the average rainfall intensity per minute, equal to the contribution in the single minute per se; (*d*) construction of the average intensities (i_j) for the whole event

5.3   THE REFLEX CANON EOS 400D

The connection between the Canon Reflex EOS 400D and the Raspberry board takes place through a USB port. the camera is controlled and managed through the software gPhoto2, which allows the acquisition of a pre-established amount of images during the minute, by setting the acquisition parameters. In the present case, the chosen number was set to 12 images per minute. This number is smaller than what has been described in the Chapters focusing on the procedure, and the rationale behind its choice is the aim of prolonging the camera's life, which in this phase was acquiring images continuously. The parameters to capture images, on the other hand, have been set in accordance with the results described in Chapters 0 and 0, in order to maximize rain's visibility. The parameters were as follows:

- Focal length: 55 [mm]

- F-Number: f/5.6
- Exposure time: 1/160 [s]
- Focus distance: 2000 [mm]

5.4   ANALYSIS OF THE RESULTS

Following the application of the method described in Chapter 3 and Chapter 4 to the images acquired by the measurement station described above, the intensity values of rainfall per minute were calculated, for the time spanning between 15/05/2016 and 15/02/2017. Only a few moments were not present in the time span, and this was due to some short moments during which the station had to be switched off to allow maintenance. Overall, in the time span observed, there have been about 1200 minutes of rain during the daytime. Recognition of these periods required calculation of the ephemeris of sunrise and sunset for the chosen site, knowing latitude and longitude (45° 03' 45.2" N, 7° 39' 36.0" E), to which a shift of 1.5 hours was then applied to ensure conditions of sufficient light even during cloudy weather conditions. Figure 5.5 briefly shows the effect of the shift applied over one day.
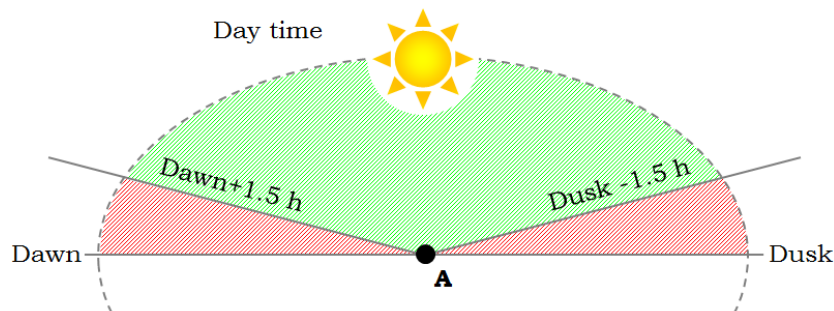
Figure 5.5 - Application of a 1.5-hour shift to sunrise and sunset times, calculated for the generic site A

Furthermore, images were also collected at night time and in snowfall conditions in the month of December. The minutes that fall in these latter categories were manually deleted from the database used in the current application, but will be used for future applications.

Differently from what has been described in section 4.4, in the current application the aim was to search for the drops by applying a succession of thresholds (i.e., only 5) that was reduced compared to the previous 8 ones (i.e., from threshold 3 to threshold 10), but increasing the value of the maximum applied threshold to 24. From this point onwards, whenever the S_1 will be referred to, it will be to indicate that a sequential selection of drops has been applied to an image cleaned of its

background, starting from S_1 and getting up to S_1+4 (e.g., $S_1 = 5$ means to apply a sequential selection spanning from threshold 5 to 9).

For each S_1 threshold (i.e., the starting value of the thresholds sequence) the measurements obtained applying the new method are rr_{IRR} and the measurements obtained through the rain gauge are rr_g. Given these specifications, the intensities per minute and five error statistics have been calculated. These are:

- *MAPE, Mean Absolute Percentage Error*:

$$MAPE = \frac{1}{n}\sum_{i=1}^{n}\left|\frac{rr_{IRR,i}-rr_{g,i}}{rr_{g,i}}\right|$$

- *MAE, Mean Absolute Error*:

$$MAE = \frac{1}{n}\sum_{i=1}^{n}\left|rr_{IRR,i}-rr_{g,i}\right|$$

- *RMSE, Root Mean Squared Error*:

$$RMSE = \sqrt{\frac{1}{n}\sum_{i=1}^{n}\left(rr_{IRR,i}-rr_{g,i}\right)^2}$$

- *R^2, Coefficient of determination*:

$$R^2 = 1 - \frac{\sum_{i=1}^{n}(rr_{IRR,i}-rr_{g,i})^2}{\sum_{i=1}^{n}(rr_{g,i}-\overline{rr_g})^2} \quad \text{with} \quad \overline{rr_g} = \frac{1}{N}\sum_{i=1}^{n}rr_{g,i}$$

- *Bias*:

$$Bias = \frac{1}{n}\sum_{i=1}^{n}(rr_{IRR,i}-rr_{g,i})$$

Figure 5.6, Figure 5.7 and Figure 5.8 show the comparisons between measurements obtained through the application of the IR^2 method, and those deriving from the rain gauge. A first glance will highlight how the use of the sequential thresholds allows for good stability in results' quality, with a few issues of underestimation in those events that are more intense for the lower and higher thresholds. This is due to a loss of the signal in the phase of drops individuation because on the one hand at lower thresholds the method has a tendency not to correctly separate the groups of drops, which are then deleted without reaching the minimum contribution filter. On the other hand, at higher thresholds the lost signal is the one of the smaller drops, as they are categorized as background noise and therefore deleted.
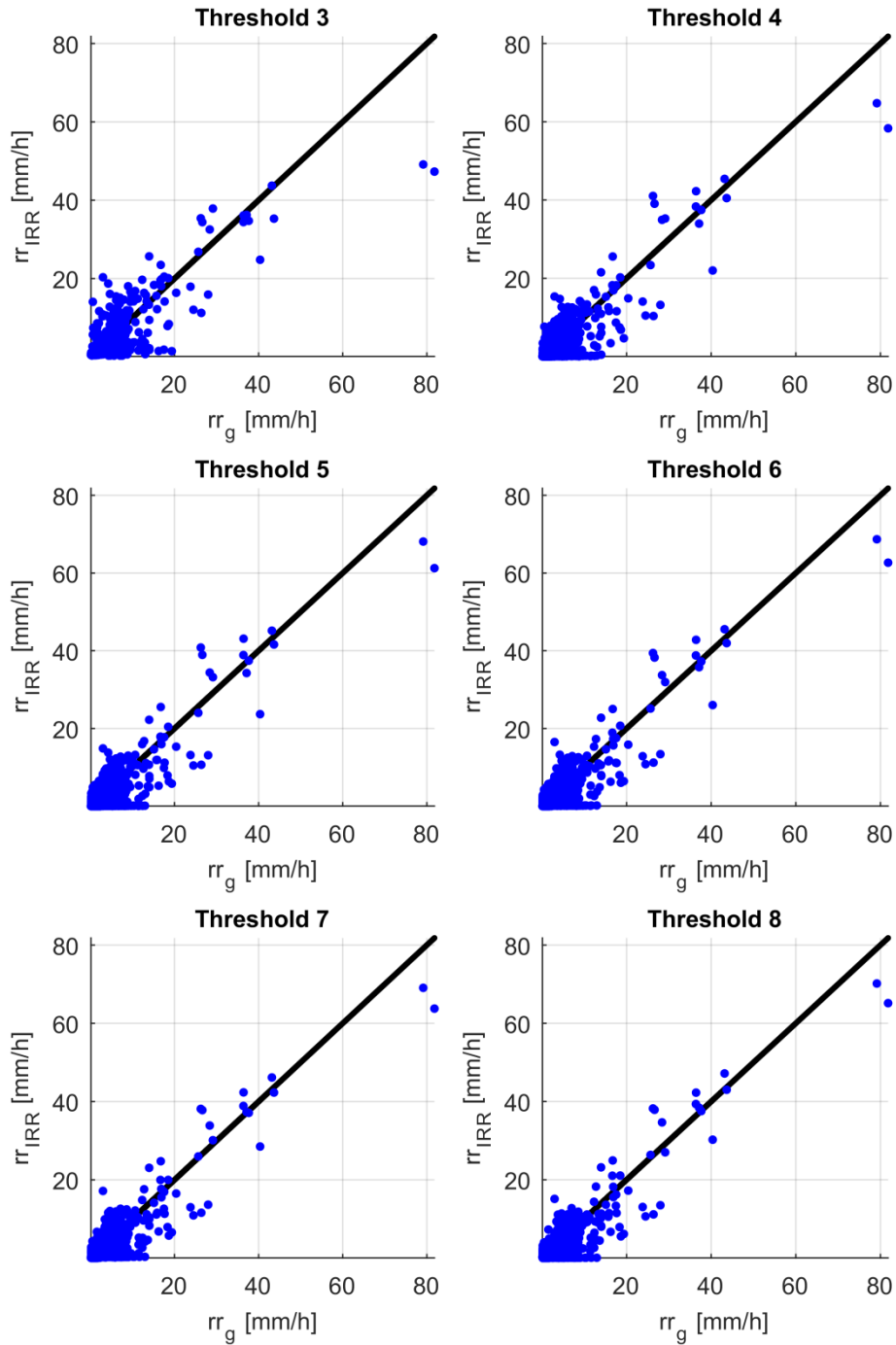
Figure 5.6 - Comparison between the rain gauge measurements and the ones obtained adopting the IR2 method for thresholds 3-to-8
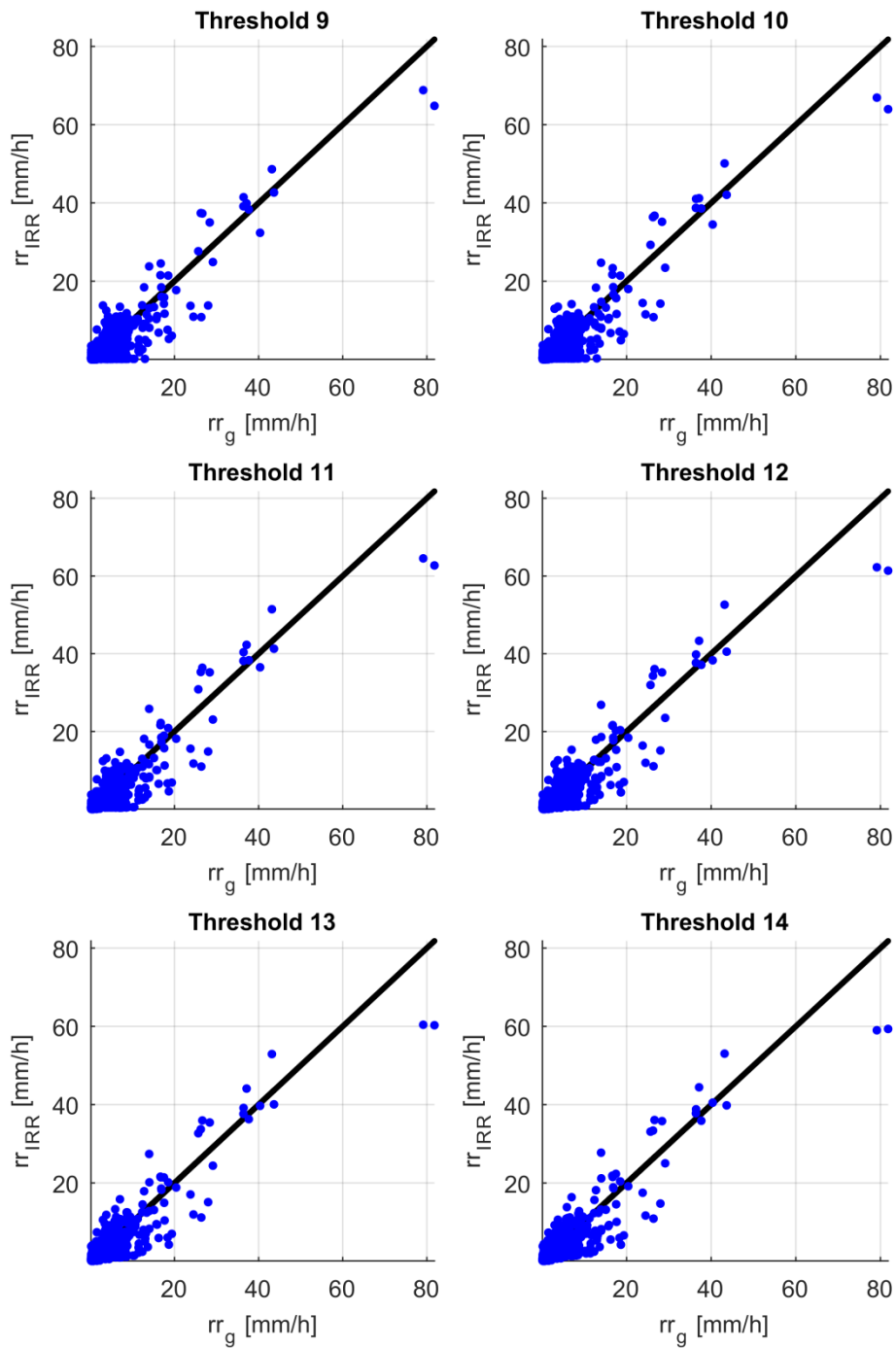
Figure 5.7 - Comparison between the rain gauge measurements and the ones obtained adopting the IR2 method for thresholds 9-to-14
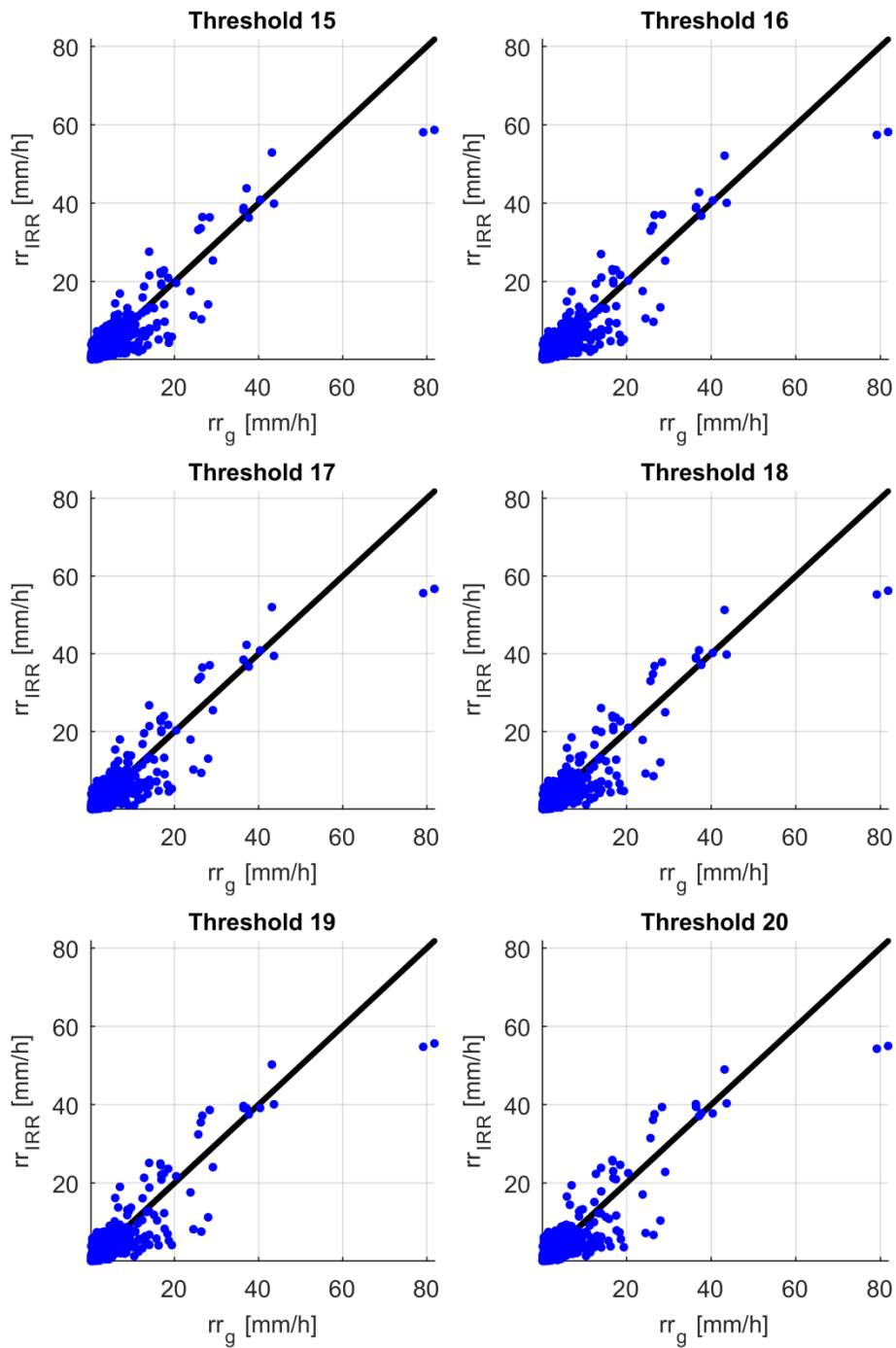
Figure 5.8 - Comparison between the rain gauge measurements and the ones obtained adopting the IR2 method for thresholds 15-to-20

Observations related to measurements accuracy are confirmed by the error statistics represented in Figure 5.9.

The statistics trend shows that the optimal thresholds is $S_1 = 15$, for the sequence 15, 16, 17, 18, and 19. In this case the average absolute error is 1.35 mm/h, which can be translated as an average percentage error of 61%. This error is explained by the presence of a high amount of minutes which are characterized by an extremely low rainfall intensity, which causes the rain gauge's accuracy to be strongly decreased and the differences between the proposed method more visible. Moreover, differently from the sample on which the methods have been tested, the photos acquired with this application have a greater variability in terms of light of the framed scene, which is something that at times makes it more difficult to see the smaller drops. The RMSE of the sample referred to the threshold $S_1 = 15$ is 2.42 mm/h. Given the amount of variability of the rainfall measured by the rain gauge ($0 \div 80$ mm/h), this value supports the good performance of the IR^2 method. Such a threshold appears to be the best one also with regard to *Bias*, which in this specific situation has a value of -0.17, even though at thresholds $S_1 = 14$ and $S_1 = 20$ the sample's distortion remains almost the same.
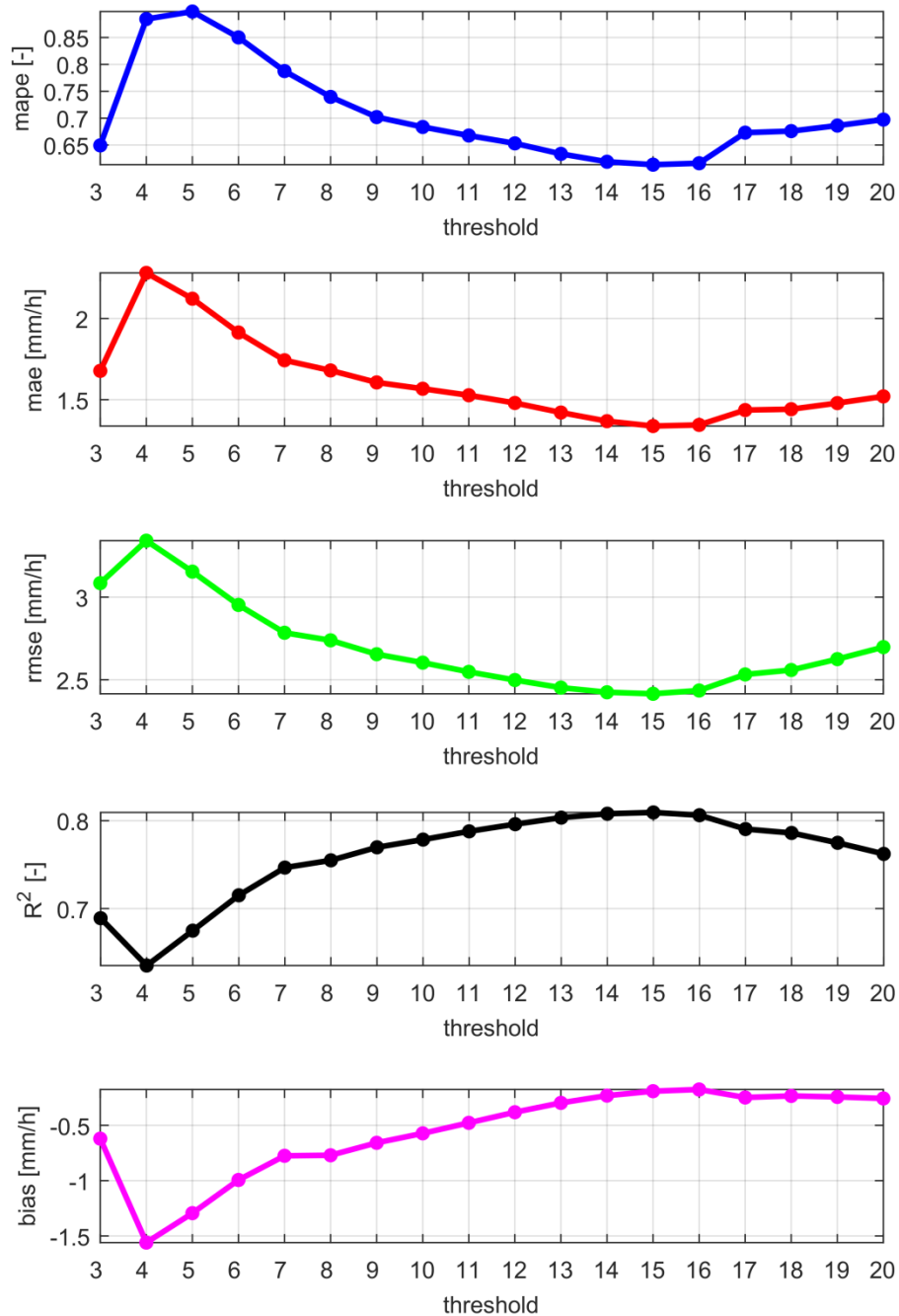
Figure 5.9 - Error statistics as sunctions of the S_1 thresholds

To achieve better detail, Figure 5.10 only reports the results for threshold 15, i.e. the best performing one. It is possible to see that, where the rain gauge measured maximum intensity, there are some underestimates due to the issues in recognizing the drops. Two are the causes of error in this occasion, which are

evident when looking at Figure 5.11. The picture in the figure was taken at 16:25 on the 14/05/2016, when the maximum rainfall was happening (rr_g = 81.8 mm/h) and is characterized by the presence of numerous drops, which have the tendency to overlap. A further added difficulty was to construct a median background without the rain signal because of the high probability of having pixels characterized by the presence of a drop in most of the images. The combination of these two phenomena meant that a non-negligible amount of the drops in the picture had been deleted, therefore causing an underestimation in the rainfall intensity.
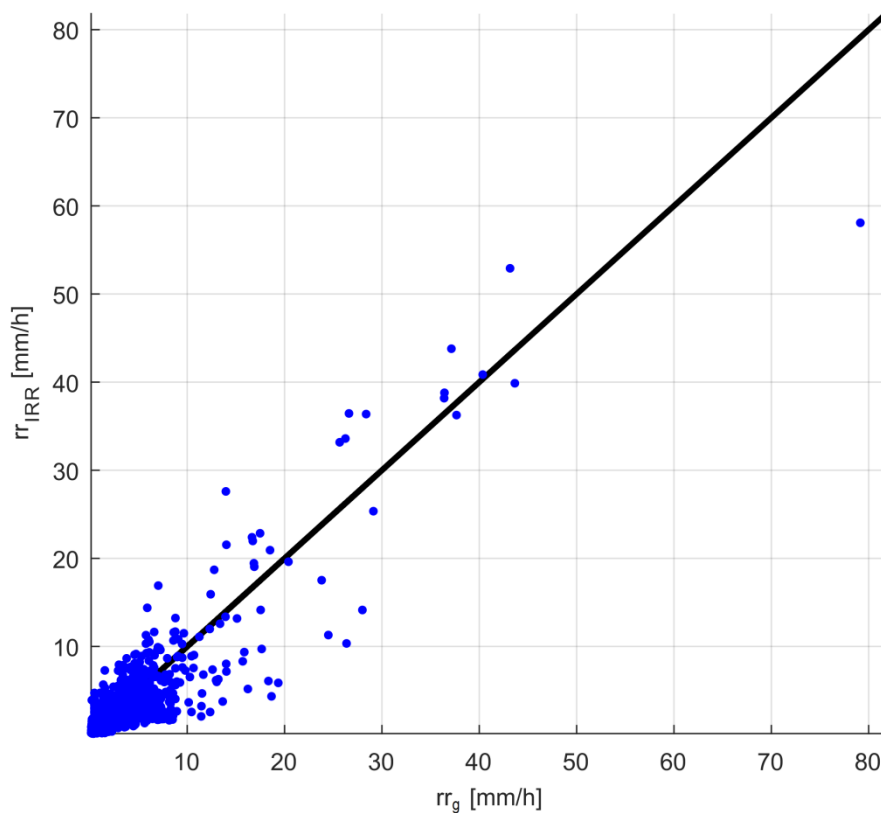
Figure 5.10 - Comparison between the intensity measured by the rain gauge and those obtained with the IR^2 methods, applying a threshold of S_1=15

Figure 5.11 - Image acquired at 16:25 on 14/05/2016 in correspondence with the peak of intensity of the event. The presence of overlaped drops causes the missed recognition and, as a consequence, an underestimate of the rainfall intensity

Keeping the threshold $S_1 = 15$ as fixed, Figure 5.12 reports the comparison between the historical series measured by the rain gauge (i.e., blue histogram) and the one constructed based on the acquired images (i.e., red line). The two curved lines show a good correspondence, if only for some underestimates as the one described above. In particular, it is possible to see how on the event of May 14th (between epoch 100 and period 230 circa) there is only an underestimate in correspondence of the intensity peak (on period 156), while the other minutes only present minor differences between the two estimates. This is confirmed by Figure 5.13, which reports the trend of the rainfall height which was accumulated and measured by the rain gauge (blue line) and by the IR[2] technology (red line). This clearly shows how in the time span between epoch 100 and 230 as above, the two curves overlap well.
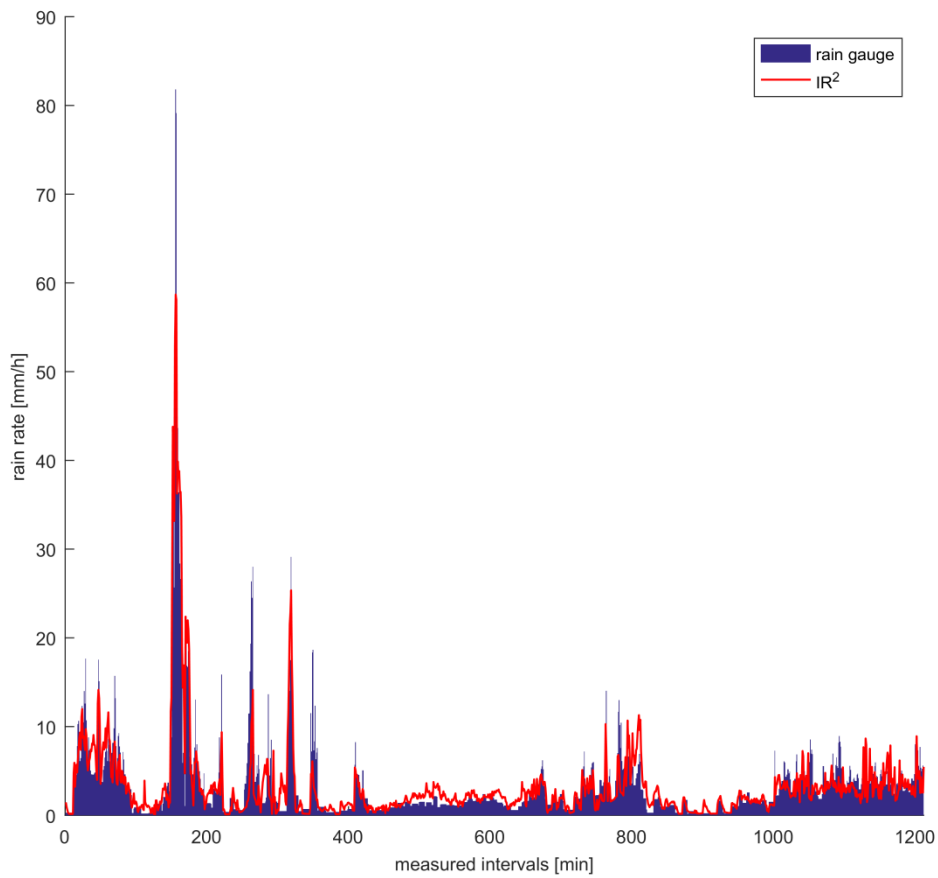
Figure 5.12 - Comparison between the historical series of intensity measured by the rain gauge (blue) and by the IR^2 technology (red), applying a threshold of $S_1 = 15$. To allow for clearer display, those minutes with no rainfall were excluded
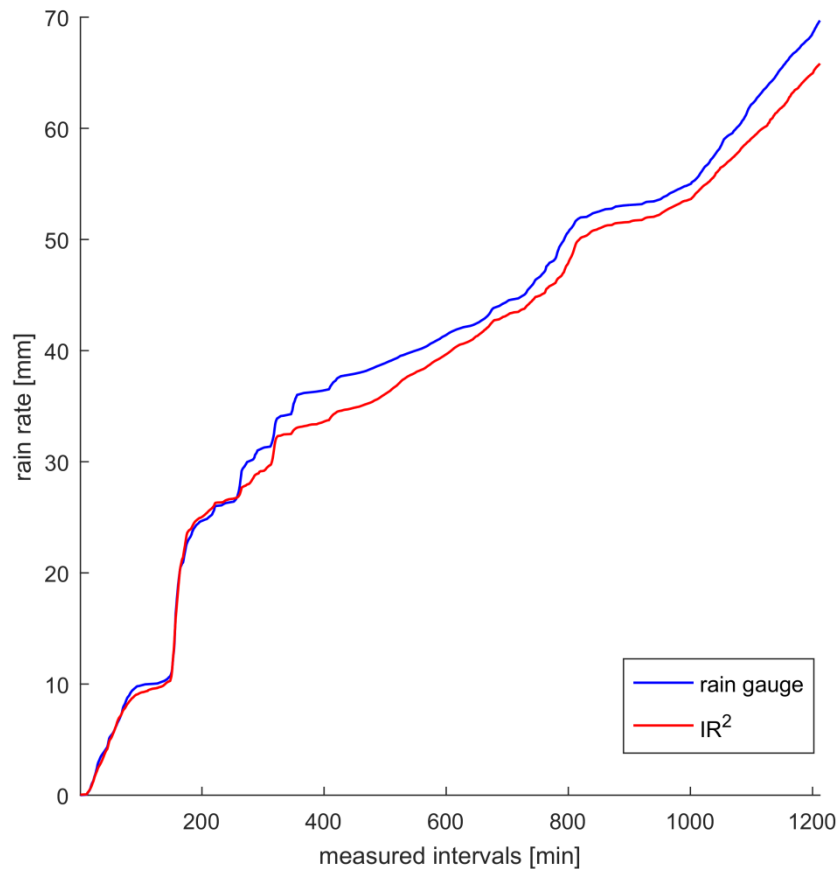
Figure 5.13 - Comparison between the cumulative rainfall height as measured by the rain gauge (blu line) and by the IR^2 (red line), applying a threshold $S_1 = 15$ for the whole sample of time

The only real difference, which extends until the end of the sample, happens at epoch 260. Such a deviation depends upon an underestimate caused by a rain outburst characterized by a relevant intensity ($rr_g > 25$ mm/h, see Figure 5.12) in conditions of low light. That event, which took place on the 16/06/2016 between 18:10 and 20:30 recorded its peak intensity of 28 mm/h at 18:42 local time. Figure 5.14 reports an image extracted from the maximum intensity minute from which it is possible to notice the difficulties in individuating the drops. Because of the peculiar light conditions of the scene, the algorithm used to recognize the drops was not able to identify a sufficient amount of drops in order to reach a correct estimation of rain intensity. The event was also terminated because of sunset, which on June 16th in Turin happened at 21:20. This resulted in an anticipated termination of the analyzed window for pictures, 1.5 hours earlier than sunset, therefore the event ended at 19:50.

Figure 5.14 - Image acquired on 16/06/2016 at 18:42 at the event peak time. The low light condition of the image prevented from the correct recognitions of the drops, with an underestimation of the rainfall intensity

5.5 DISCUSSION

The analysis described in the present Chapter highlighted a good response of the method and the ability to accurately describe events of real rain both in the event scale and in the long-term. The absence of an analogue algorithm which allowed working at night time with low light conditions, as shown, means that the method is sensitive to variation of light of the framed scene. As a consequence, there are some underestimates which are mainly due to the difficulty in detecting rain drops. In the same measurement station described in this Chapter, a luminosity sensor connected with the control unit (Raspberry Pi) has been recently installed (March 2017), with the aim of evaluating the environmental light conditions. This information will be used, in mid-light conditions, to: (a) increase or decrease drops' visibility in images during the post-processing phase; (b) directly increase or decrease the intensity of the estimated rain, modifying one or more acquisition parameters in order to increase the amount of light received by the sensor.

Nonetheless, only a series of test and experiments specifically designed will be able to determine the best solution which will then need to be evaluated in terms of accuracy of the intensity measurement, speed of processing, and minimum requisites of the machine needed for the elaboration.

Chapter 6

Technology transfer: from research to business

The methodology described hereinafter is the object of the value proposition of an emerging start-up company, whose core activity is based on the main results of the work performed during the PhD.

The path leading from an idea or knowledge to its practical implantation has ancient roots: human beings have always put into practice what they have experienced and learned, to maximize the resulting benefits, even from an economic perspective.

Over the centuries, this mechanism has been subject to changes: today the invention activity asks for several expertises and competences, generally owned by more than one organization. The resulting overall process is even more complex and structured and it requires new tools and models to manage it. Therefore, enterprises need to face the challenge of optimize their expenses for Research&Development of new products.

6.1   RESEARCH SUPPORT AND TECHNOLOGY TRANSFER

In recent years, the university system has been facing major changes, which have led to redefine roles and relationships between the academic and the business world. This mutation has contributed to strengthen the relation with the external

environment, aiming to promote the academic image, as well as its researches and products. To this end, the university system has improved its connection with local communities and, specially, with Small and Medium Enterprises (SMEs), to enhance their involvement in new products and projects investments.

The academic third mission covers all the necessary activities, enabling universities to deeply understand the whole Society and its requirements and to detect proper solutions to meet its specific needs, thus making the business-university axis more competitive and contributing to the Country's socio-economic growth.

Although education and research represent the core activities, to meet its mission the academic world needs to identify external contexts for the practical implementation of the main outcomes resulting from the research activity. To this end, most of the Italian universities and research centers created a Technology Transfer Office (TTO), also known as Industrial Liaison Office (ILO), to properly protect and promote the intellectual property resulting from the human inventiveness and belonging to the academic community, and to foster its transfer into the business context, encouraging the linkage between university and the local entrepreneurial world. The TTOs also provide patent services to researchers to correctly address all issues related to the technological transfer and research exploitation.

The technology transfer is a non-linear process, with various implementation procedures; it directly involves more subjects, expertises and competences, with the aim to provide services and ad hoc structures to the inventors and the end users of the technology. It aims also to encourage patenting, licensing as well as the creation of start-up and spin-off companies, ensuring for the dissemination of knowledge to all the local stakeholders (Bozeman, 2000).

6.2   INCUBATORS OF ENTERPRISES

Newly founded companies, whether start-up or academic spin-off, can count on support from the Incubators of Enterprises, in addition to the wide range of services and benefits arising from the academic networks and to the technology transfer centers.

The Incubator offers specific competences and consultancy services, to assist new companies in creating their own business, in a highly stimulating environment, which contributes to create synergies among the incubated companies and to increase their visibility to the external context and the reference market. The main purpose of the Incubators is to support young entrepreneurs in the development

and commercialization of their knowledge, as well as in the acquisition of proper technology, to minimize the uncertainty factors related to highly discriminating processes (Lanza, 2002).

In the complex technology transfer ecosystem, the incubators are usually located closed to universities and research centers, representing clusters of companies with high Research & Development capabilities.

6.3 START-UP

The term start-up is mainly used to identify a company (even not related to the university system, as the spin-off) at the first stage of activity, generally with a fast growing business, due to its repeatable and scalable business model.

A startup company (or simply start-up) is usually a newly founded or emerged company, characterized by an organizational process still ongoing. It is interesting to point out that, in economy, the term start-up has mainly a temporal value and it can also be applied to a new business unit in existing companies. In any cases, it doesn't ever refer to a specific business category.

In this first stage, start-up may need: i) to acquire new resources, skills, know-how and techniques, ii) to define internal hierarchies and proper production methods and iii) to recruit (other) qualified personnel. During the start-up phase, the company needs to carry out a market feasibility analysis to properly identify its target market segments and related requirements and, hence, the company's strategies and activities.

During its lifetime, an enterprise faces a sequence of stages, needing to implement different business strategies, according to the characteristics of the stadium itself. The typical start-up development phases are the following:

1. *Vision*: the entrepreneur sees an opportunity that others do not; the long term business vision is to be defined (5/10 years);
2. *Business idea*: the opportunity must become a winning idea, where time is a crucial factor for the competitive advantage;
3. *Start up*: the entrepreneur handles every managerial responsibility within the organization, addressing all the emerging problems. At this stage, the entrepreneur needs to define several plans (marketing&communication, financial, business, …) covering at least the following three years;
4. *Early stage*: it is a crucial phase for the company's fate, sizing its future business. The company is usually still a small entity with few customers;

5. *Growth stage*: the company increases its customers' portfolio and sales, new personnel is needed to delegate responsibilities, according to the company size and strategy;
6. *Rapid growth stage*: this stage may not exist, depending on board's capabilities and on company's ambitions; the entrepreneur is responsible for the long term strategic planning and for the financial control;
7. *Maturity stage*: the business model is tested with a defined target market and established customers; now the main challenges faced by the company are related to the identification of new market segments, trying to meet emerging requirements;
8. *Innovation stage/decline stage*: changes in the company's context call for a choice: modernize or pay off.

The company may add new products and/or services, as well as acquire other companies and business, with the aim to renew itself: the entrepreneur is responsible to inspire the efforts of the innovation stage.

Crowdfunding is the driving factor of the whole company's life and stages, in terms of duration, performance and being successful. It can take place at different stages in the life cycle of the company and for various reasons, but the most decisive one is done at the earliest stages.
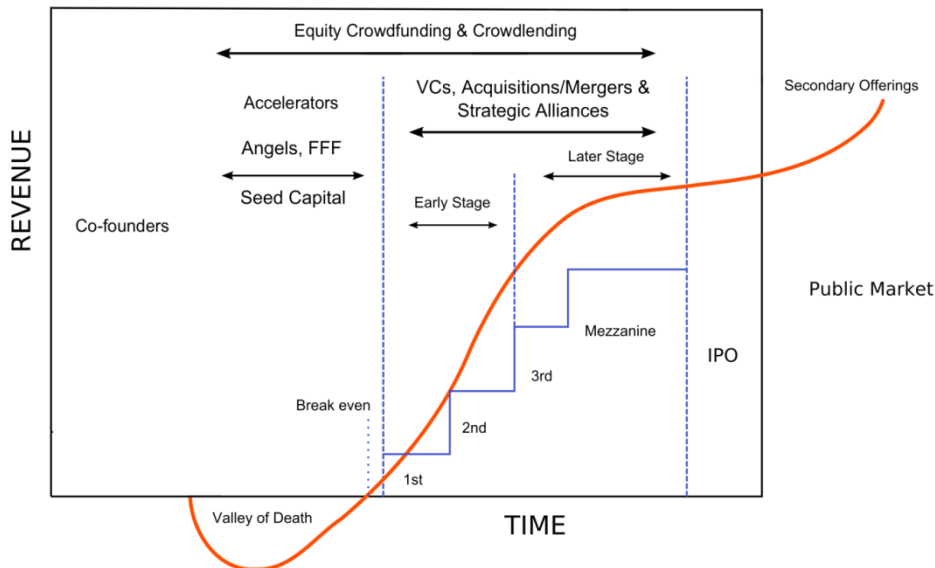
Figure 6.1 - Diagram of the typical financing cycle for a startup company
(https://en.wikipedia.org/wiki/Startup_company)

The diagram in Figure 6.1 shows the typical trend of two crucial factors in determining the evolution (and success) of a startup company: financing (light blue line) and revenue (red line); it also indicates the subjects responsible for such

investments, that can be more or less onerous. The funding stages can be summarized as follows:

- *Seed capital*: represents the "investment" done in the very early phase, when the company doesn't still have a business; it is used to further investigate the business model and its financial perspective. The seed capital is not a loan, but more a stock opt (even done as ownership shares). This stage lasts until new investment rounds are done or the company is able to finance itself. At this stage, the start-up is financed by two categories of investors: Business Angels (acronym BA) and Friends, Family and Fools (FFF). A Business Angel is usually a wealthy individual, who provides capital and expertise to a start-up company, aiming for a monetary return. The second ones are those willing to invest a "significant amount", without any specific know-how or expectation. Generally, the first stage investments have a high return rate, typically 10 times (or more) the capital invested;
- *Early stage financing* and *later stage financing* (the following rounds of investments): the first capital raised aims to allow the implementation of the company's business model, even through the acquisition of the necessary resources (raw materials, personnel, real estate) and competences. Later rounds of investment are intended to expand the company's business: the break-even point is still far away. The major investors at these stages are Venture Capitalists (acronym VC) or their union into financing company, having at portfolio several companies to finance. The investors seek for an economic return in the later stages of the company life cycle;
- Public market: excluding recapitalization, the public market is the last stage of the startup finance. To maximize the economic return, the company may opt for:
  - Total (exit) or partial sale to other companies or owners;
  - Initial public offering (IPO) or stock market lunch: the company sells its participation shares (shareholdings) at the nominal price collected by the old property (entrepreneur, BA, FFF,VC). The IPO is commonly used to raise new capital for expansion and to monetize early investors' investments. The new investors have the right for future allocation of dividend or, in case of liquidation, for the company's capital stock.

The university system is, therefore, the main actor in displacing the academic innovations from the research activity into the business context. Technological

innovation is a complex process, involving multiple actors and levels; it arise from various mechanisms which take place in different ways and variable times.

According to the object, innovation can be classified in:

- product innovation, related to a new product or service;
- process innovation refers to a new method of production or delivery (Schumpeter, 1934).
- according to the novelty level, it can be classified in:
- incremental innovation, representing an improvement or adaptation of existing technology;
- radical innovation, resulting in a totally new technology or a new method to exploit an existing one.

6.4 WATERVIEW

WaterView is a young and dynamic start-up company, founded in February 2015 as a spin-off of the Politecnico di Torino; it is currently host by I3P, the Innovative Enterprise Incubator of the Politecnico itself.

WaterView develops services in the field of hydro-meteorology, chasing the dream of making the technology presented in this thesis succeed. A patent application, currently being extended internationally, has been filed by Politecnico of Torino for the algorithm on which the technology is based and WaterView (as a spin-off company) is the exclusive licensee of the patent.

WaterView introduces a highly innovative solution for the real time monitoring and measurement of atmospheric events which can be rapidly disseminated; it focuses on efficacy and cost-effectiveness in the generation of data thanks to the use of existing infrastructures.

The technology, whose functioning is summarized in the following Figure 6.2, is based on the work performed during the PhD and described hereinafter.
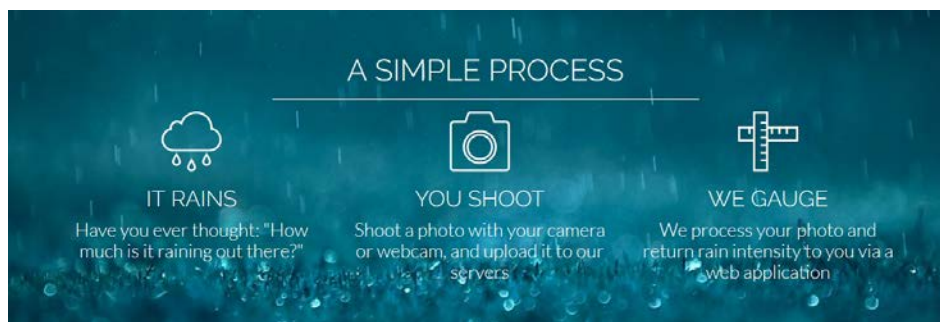
Figure 6.2 - WaterView technology, a practical example of innovative product

The technology, implemented in the form of a cloud service, is compliant with the vast majority of devices equipped with a camera, opening the way to the collection of an enormous amount of rain observations deliverable to end users at a previously unimaginable speed. Images shot during rain events, from fixed (non) dedicated camera and personal devices, can thus been processed to infer and communicate to end users (through a web portal) rain intensity in real time, thus disrupting the current panorama of data acquisition rainstorm sensing.

The team consists of the three founding members (engineers of the civil-environmental sector), who are also the inventors of the technology, supported by a group of coders and developers, a scientific advisor and a business strategy mentor.

6.4.1 Fundraising

In July 2016, WaterView received a first round of investment from the Club degli Investitori di Torino, a BA network of entrepreneurs, professionals and managers, aiming to invest in new and recent companies with innovative products/services and high potential.

The Seed capital raised (for a total amount of € 475.000,00) aims to allow the company to give an acceleration to its business, with respect to the development and commercialization of its solution.

The investment was preceded by an initial phase during which WaterView presented to the Club its founders, technology and a go-to-market business plan. Once decided for the investment, the Club appointed a Champion among its member, a link between the startup team and the investors network.

Since its foundation WaterView has been searching for other forms of investment, specially public funds. To this end, it has been participating at several National and International projects: in May 2016, the startup won a EU SME Instrument Phase 1 grant, under the Horizon 2020 program for a total amount of €50.000,00. The project, presented in the "New business models for inclusive, innovative and reflective societies" topic, aimed at outline the technical features of WaterView breakthrough innovation and defining effective marketing strategies, based on the outcomes of market surveys and customers/end users analyses.

6.4.2 Business opportunity

The technology and the proposed solution, based on the main outcomes of this thesis, allows for the collection of diffuse real-time rainfall data, with a higher

spatial and temporal resolution than the existing technologies (mainly weather radar, satellites, at-ground sensors).

The high potential of WaterView success is demonstrated by the magnitude of the entire weather-related industry, estimated at 30 G€, with a global growth rate of more than 10%. At the end of 2015 IBM acquired most of The Weather Company for over 2 G$.

The weather sensor market accounts for 1.8 G€, while the one related to at-ground rain gauging systems is estimable in about 300 M€, a fifth of which is attributable to the European market.

The high spatial and temporal resolution of WaterView data allow one to identify several potential market segments of the technology, listed in the following paragraphs.

The need for widespread rainfall measurements emerges from the agricultural segment, recently shifting into a smart farming model.

Figure 6.3 - Precision and Smart farming represent the future of the agricultural sector and rational use of water resource and selective application of phytosanitary products are key points for their development. To optimize production, everithing is connected and sends data to the cloud so that the best actions can be planned

The smart farm and the smart farming practices (see Figure 6.3) are collecting a wide and strong interest of the National, European and International communities (Sundmaeker et al., 2016; https://www.smart-akis.com). The collection of real time rain rate measures, as well as more precise weather forecasts, enhances the sustainability of agricultural practices, promoting a rational use of water resource and a selective and parsimonious application of phytosanitary products.

In the security field, the technology may provide public administrations in charge of civil protection duties a tool for a better emergency planning and management, especially for extreme events occurring in basins with short response time or in urban environment. In such cases, a real time measure as the one proposed by the Company is crucial to trigger the intervention of civil protection, law enforcement, to promptly issue alarms and alerts. A reliable and diffuse measure of rainfall intensity, combined with a proper management of emergencies will lead to a reduction of costs in term of damages to people and property, false alarms and missed alerts.

Figure 6.4 - The surveillance cameras detect rain and send a message to the (connected) cars. The users can adapt their driving behaviour in advance, avoiding crashes and casualties

At the same time, road management administrations can benefit from the technology, by promptly adapting the road management practices to real time weather conditions, thus ensuring higher safety conditions to end users. The relevance of improving road safety, even though specific programs and goals, have been pointed out by the European Commission in the 2011 Transport White Paper stating a goal of "move close to zero fatalities in road transport" by 2050 and "halving road casualties by 2020" (Figure 6.4).

Weather forecasters aim to provide more local and customized nowcasts and forecasts, to respond to the emerging needs of end users. Currently now/forecasts are mainly based on satellites, weather radars as well as on terrestrial sensors networks; those sources need to be integrated with a more diffuse one (like the one provided by WaterView) to allow for more precise weather forecasts. The integration of all these data would allow for a more accurate input into the predictive models and, thus, to improve their quality and accuracy.

Another market segment of the technology is the one related to sport. Real time monitoring of rainfall enable sportsmen and teams to adapt their strategies and improve performances and security conditions. Car and bike racing, cycling, sailing and other outdoor sports are affected by weather. More precise weather nowcasts and forecasts will allow the sport teams to promptly respond to weather changes (Figure 6.5), adapting the competition strategy (for example, mounting the right tires, adapting the speed, etc.) and reducing the risks for athletes and the audience along the race path.

Figure 6.5 - Example of an heavy rain event during a F1 GranPrix. The knowledge of track condition are crucial to determine the strategy

The last main possible application involve people as moving raingauges. In fact, by exporting the technology on mobile phones, which have all the requirements (in term of image quality, processing capabilities, connection, etc.) to be a measuring instument, we can obtain rain informations from everywhere in real-time. This could allow us to collect data for everyone of the abovementioned markets and most of all, to improve self awareness of people itself. In many cases, in fact, during heavy rain events and floods, the greatest danger for people's lives are the wrong choiches that are made by themselves (see Figure 6.6). This issue is strongly related to the lack of knowledge of rain and its interaction with the environment.

Figure 6.6 - An example of bad behaviour of people during rain events. The urge to save tangible goods and properties drives peoples to do irrational things

The common aspect of all the market segments described are the rain data collection. These data, in a world where IOT paradigm asks for an ever-increasing amount of data, are the real core business for a company as WaterView. All the measures, collected for each of the previous applications can be stored and sold to weather providers in order to have better input data for their forecasting models. This would lead to better performance of the models and a higher reliability of the forecasts.

6.4.3   Explored markets

In the last year, WaterView worked hard on the development of different products to access the markets described in the previous section. In particular it is working on the definition of a partnership agreement with one of the biggest camera producers (Axis Communications) to develop a plug-in which can transform each surveillance camera in a measurement point.

At the same time business activities have been foreseen with:

- some big players of agricultural market in the field of sugar cane, coffee and wheat production;
- an high level team in motorsport and the organizing committee for motorcycling events;
- some realities connected to civil protection and road safety;
- driverless cars producers;
- weather providers

These companies and organizations cannot be openly mentioned because of existing non-disclosure agreements (NDA).

Chapter 7

Conclusions

The comparison between the two technologies, IR^2 methodology (as described in Chapter 5) and rain gauge, even if the first one is still under development, puts IR^2 technology in a better position from many points of view.

Complexity and cost. The rain gauge, in its latest technological variants, can be a complex tool and the maintenance costs are not indifferent. The IR^2 technology, by contrast, is easy to manage, maintain and use because the devices consist in a photo sensor and a processor capable of processing the captured images. As well as lower costs, it shows greater availability and an easier implementation as part of a wider number of users.

Spatial resolution. The rain gauge network is still quite poor. In fact, the total number of rain gauges on the Earth's surface ranges from a few thousand to hundreds of thousands including amateur instruments. It is well known that while imagining, for each rain gauge, a circular region of influence of 5 km radius (definitely abundant value as precipitations, especially for short durations, have more restrictive spatial variability), one could describe less than 1% of the earth's surface (Kidd et al., 2014). In case of short duration events spatial resolutions of about 2 km would be needed (Berne et al., 2004).

This methodology, conversely, can greatly improve the density of the ground measurements, thanks to the low cost and ease of use and implementation. IR^2 technology can be easily exported on smartphones and portable rooms, offering the possibility of creating a dense and spatially accurate network of measuring. To

this aim the installation of rain gauges in moving vehicles has been proposed (Cord and Aubert, 2011). Studies on non-conventional networks (Rabiei et al., 2013) show that the precipitation estimates are more reliable if you have a large distribution of tools, although less accurate than conventional ones.

Temporal resolution. The rain gauge measures due to strictly technological issues have limited temporal resolution. In the most favourable cases of rain gauge action frame, as mentioned, it tends to be used measurements with a temporal resolution of minutes. It is, however, well known that the accuracy of the pluviometric measurement decreases with the rate of acquisition (Habib et al., 2001). The proposed methodology can estimate the intensity with much higher resolutions, e.g., 30 per minute, capturing temporal variability that cannot be observed by the rain gauge. More robust values can be determined by averaging the measurements.

The aim of this work was not to compete with standard instruments as rain gauge or disdrometers, but the comparison with their performance is the only available way to determine the reliability of the proposed technology. The best alternative to the comparison with the rain gauge should be testing the IR^2 technology with artificial rain, generated under controlled conditions. The main limitation about this kind of approach lies in the construction cost of such an infrastructure. In the world there are few large scale rain simulator an their cost is about 100÷500 k€ This price depends on the size of the simulator, the reliability and the repeatability of the designed rain.

The main objective was to develop a new instrument able to reach a higher spatial diffusion (compared to the actual sparseness of the gauging networks) with a real-time response granting an accuracy comparable with the one provided by the standard instruments.

In order to proceed in this direction the foreseen improvements in the method that we will explore, include further investigation on:

- the sensitivity of the method to the background brightness and the features that compose the background;
- non-stationary background, i.e. moving cameras, fixed cameras on moving objects (e.g., cars), smartphones;
- the reliability of the method to the use of different camera models and low cost cameras;
- extending the method to pictures taken in night-time or low light conditions.

References

1. Adami, A., & Da Deppo, L. (1986). On the systematic errors of tipping-bucket recording rain gauges. Instruments and Observing Methods Report, 25, 27-30.

2. AghaKouchak A., E. Habib and A. Bárdossy (2010), Modeling Radar Rainfall Estimation Uncertainties: Random Error Model, Journal of Hydrologic Engineering, 15 (4), 265-274, doi: 10.1175/2010JAS3706.1.

3. Alawi M. A., Khalifa O. O. and Islam M.D. R. "Performance Comparison of Background Estimation Algorithms for Detecting Moving Vehicle". In World Applied Sciences Journal 21 (Mathematical Applications in Engineering), (2013), DOI: 10.5829/idosi.wasj.2013.21.mae.99934, 109-114.

4. Allamano, P., Croci, A., & Laio, F. (2015). Toward the camera rain gauge. Water Resources Research, 51(3), 1744-1757. doi:10.1002/2014WR016298.

5. Battan, L. "Radar Observation of the Atmosphere". University of Chicago Press: Chicago, IL, USA, 1973. ISBN: 9780226039190.

6. Beard K.V. (1976), Terminal velocity of cloud and precipitation drops aloft. J. Atmos. Sci., 33, 851–864, doi: 10.1175/1520-0469(1976)033<0851:TVASOC>2.0.CO;2.

7. Beard K.V., V.N. Bringi and Thurai M. (2010), A new understanding of raindrop shape, Atmospheric Research, 97 (4), 396-415, doi: 10.1016/j.atmosres.2010.02.001.

8. Benjamin C.A, and J.R., Cornell (1970), Probability, statistics, and decision for civil engineers, McGraw-Hill Book Company, ISBN: 978-0070045491, p. 310-311.

9. Berne, A., Delrieu G., Creutin J.-D., and Obled C. (2004), Temporal and spatial resolution of rainfall measurements required for urban hydrology. J. Hydrol., 299, 166–179, doi: 10.1016/j.jhydrol.2004.08.002.

10. Bossu, J., Hautière, N., & Tarel, J. P. "Rain or snow detection in image sequences through use of a histogram of orientation of streaks". In International Journal of Computer Vision, (2011) 93(3), 348-367.

11. Bozeman, B. "Technology transfer and public policy: a review of research and theory". Research policy, 29(4), 627-655, 2000.

12. Bringi, V., V. Chandrasekar, J. Hubbert, E. Gorgucci, W. Randeu, and M. Schoenhuber. "Raindrop size distribution in different climatic regimes from disdrometer and dual-polarized radar analysis". In: J. Atmos. Sci. 60.2 (2003), pp. 354–365.

13. Brocca L., L. Ciabatta, C. Massari, T. Moramarco, S. Hahn, S. Hasenauer, R. Kidd, W. Dorigo, W. Wagner, V. Levizzani (2014), Soil as a natural rain gauge: Estimating global rainfall from satellite soil moisture data, Journal Of Geophysical Research-Atmospheres, 119 (9), 5128-5141, doi: 10.1002/2014JD021489.

14. Chapon, B., G. Delrieu, M. Gosset, and B. Boudevillain. "Variability of rain drop size distribution and its effect on the Z-R relationship: A case study for intense Mediterranean rainfall". In: Atmos. Res. 87.1 (2008), pp. 52-6.

15. Cord A. and D. Aubert (2011), Towards rain detection through use of in-vehicle multipurpose cameras, IEEE Intelligent Vehicles Symposium IV, 833-838.

16. Doviak, R. J. and D. S. Zrnic. "Doppler Radar and Weather Observations". 2nd ed. Dover Publication: Dover, Uk, 2006.

17. Friedman, N., & Russel, S. (1997). Image segmentation in video sequences: a probabilistic approach. Proceedings Thirteenth Conference on uncertainty in Artificial Intelligence, (p. 175-181).

18. Garg K. and S.K. Nayar (2007), Vision and rain, Int. Journal of Computer Vision, 75(1), 3-27, doi: 10.1007/s11263-006-0028-6.

19. Gayathri R., Sabeenian R.S., "A Survey on Image Denoising Algorithms (IDA)". In International Journal of Advanced Research in Electrical, Electronics and Instrumentation Engineering Vol. 1, Issue 5, November 2012.

20. Gopinath Kathiravelu, Terry Lucke and Peter Nichols. "Rain Drop Measurement Techniques: A Review". In Water (2016), 8(1), 29; doi:10.3390/w8010029.

21. Habib E., Krajewski W.F., Kruger A., (2001), Sampling errors of tipping-bucket rain gauge measurements, J. Hydrol., 6 (2), 159-166, doi: 10.1061/(ASCE)1084-0699(2001)6:2(159).

22. Harmanciogammalu N.B., S.D. Ozkul, O. Fistikoglu, Paul Geerders (2003), Integrated Technologies for Environmental Monitoring and Information Production, Nato Science Series: IV, ISBN: 978-1402013997.

23. Hobbs P.V. and Rangno A.L. (2004), Super-large raindrops, Geophys. Res. Lett., 31, L13102, doi:10.1029/2004GL020167.

24. https://en.wikipedia.org/wiki/Startup_company

25. https://www.smart-akis.com

26. Huffman, G. J., Bolvin, D. T. and Nelkin, E. J. (2015), Integrated Multi-satellitE Retrievals for GPM (IMERG) technical documentation. NASA/GSFC Code 612(2015): 47.

27. Humphrey, M., Istok, J., Lee, J., Hevesi, J., & Flint, A. (1997). A new method for automated dynamic calibration of tipping-bucket raingauges. Journal of Atmospheric and Oceanic Technology, 14(6), 1513-1519.

28. Jones D.M.A. (1992), Raindrop spectra at the ground. J. Appl. Meteor., 31, 1219–1225.

29. Jones D.M.A. and Dean L.A. (1953), A raindrop camera, Illinois State Water Survey, Champaign, Research Report No. 3, 20 p., available at http://www.isws.illinois.edu/pubs/pubdetail.asp?CallNumber=ISWS+CR-5.

30. Joss, J. and A. Waldwogel. "A method to improve the accuracy of radarmeasured amounts of precipitation." In: In Proceedings of 14th Conference of Radar Meteorology, Tucson, AZ, USA. 1970, pp. 237–238.

31. Kidd C. , G.J. Huffman, D. B. Kirschbaum, G. S. Jackson, P. Joe, C.L Muller (2014), So, how much of the Earth is covered by rain gauges?, Geophysical Research Abstracts, 16, EGU2014-10300.

32. Kostinski, A. B., Jameson A. R. (1999), Fluctuation properties of precipitation. Part III: On the ubiquity and emergence of the exponential drop size spectra. J. Atmos. Sci., 56, 111 – 121, doi: 10.1175/1520-0469(1999)056<0111:FPOPPI>2.0.CO;2.

33. Lanza, A. "Imprenditorialità e capitale sociale: I sistemi di imprese tra mercato e istituzioni". Carocci, 2002.

34. Lee, G. W. and I. Zawadzki. "Variability of drop size distributions: Timescale dependence of the variability and its effects on rain estimation". In: J. Appl. Meteorol. 44.2 (2005), pp. 241–255.

35. Leijnse H., and Uijlenhoet R. (2010), The effect of reported high-velocity small raindrops on inferred drop size distributions and derived power laws. Atmos. Chem. Phys., 10, 6807– 6818, doi:10.5194/acp-10-6807-2010.

36. Leijnse, H., Uijlenhoet R., and Stricker J.N.M. (2007), Rainfall measurement using radio links from cellular communication networks, Water Resour. Res., 43, W03201, doi: 10.1126/science.1120034.

37. Lorenz, C. and Kunstmann H. (2012), The hydrological cycle in three state-of-the-art reanalyses: Intercomparison and performance analysis. J. Hydrometeor., 13, 1397–1420, doi: 10.1175/JHM-D-11-088.1.

38. Marshall J.S. and W.M. Palmer (1948), The distribution of raindrops with size, J. Meteorol., 5, 165-166

39. Marshall, J. S. and W. M. K. Palmer. "The distribution of raindrops with size". In: J. Metorol. 5.4 (1948), pp. 165–166.

40. Messer, H., Zinevich A., and Alpert P. [2006], Environmental monitoring by wireless communication networks. Science, 312, 713, doi: 10.1126/science.1120034.

41. Montanari A., G. Young, H.H.G. Savenije, D. Hughes, T. Wagener, L.L. Ren, D. Koutsoyiannis, C. Cudennec, E. Toth, S. Grimaldi, G. Blöschl, M. Sivapalan, K. Beven, H. Gupta, M. Hipsey, B. Schaefli, B. Arheimer, E. Boegh, S.J. Schymanski, G. Di Baldassarre, B. Yu, P. Hubert, Y. Huang, A. Schumann, D.A. Post, V. Srinivasan, C. Harman, S. Thompson, M. Rogger, A. Viglione, H. McMillan, G. Characklis, Z. Pang and V. Belyaev (2013), "Panta Rhei - Everything Flows": Change in hydrology and

society - The IAHS Scientific Decade 2013 – 2022, Hydrological Sciences Journal, 58 (6), 1256-1275, doi: 10.1080/02626667.2013.809088.

42. Montero-Martinez G., A.B.Kostinski, R.A.Shaw, and F. Garcia-Garcia (2009), Do all raindrops fall at terminal speed?, Geophys. Res. Lett., 36, L11818, doi: 10.1029/2008GL037111.

43. Nešpor, Vladislav, and Boris Sevruk. "Estimation of wind-induced error of rainfall gauge measurements using a numerical simulation". In Journal of Atmospheric and Oceanic Technology 16.4 (1999): 450-464.

44. Nystuen, J., & Proni, J., Black, P., Wilkerson, J. (1995). A comparison of automatic rain gauges. Journal of atmospheric and oceanic technology.

45. Overeem A., H.Leijnse, R. Uijlenhoet (2013a), Country-wide rainfall maps from cellular communication networks, Proceedings of the National Academy of Science (PNAS), 110 (8), 2741-2745, doi: 10.1073/pnas.1217961110.

46. Overeem A., J.C.R. Robinson, H. Leijnse, G.J. Steeneveld, B.K.P. Horn, R. Uijlenhoet (2013b), Crowdsourcing urban air temperatures from smartphone battery temperatures, Geophys. Res. Lett., 40, 4081-4085, doi: 10.1002/grl.50786.

47. Parajka J., P. Haas, R. Kirnbauer, J. Jansa, G. Bloschl (2012), Potential of time-lapse photography of snow for hydrological purposes at the small catchment scale, Hydrological Processes, 26 (22), 3327-3337, doi: 10.1002/hyp.8389.

48. Rabiei E., U. Haberlandt, S. Sester and D. Fitzner (2013), Rainfall estimation using moving cars as rain gauges – laboratory experiments, HESS, 17 (11), 4701-4712, doi: 10.5194/hess-17-4701-2013.

49. Rabiei, E., Haberlandt, U., Sester, M., & Fitzner, D. (2013). Rainfall estimation using moving cars as rain gauges - laboratory experiments. HESS, 17(11), 4701-4712. doi:10.5194/hess-17-4701-2013.

50. Raghavan, S. "Radar Meteorology". Kluwer Academic Publisher: Dordrecht, The Netherlands, 2003. ISBN: 1402016042.

51. Schmidt J.M., P.J. Flatau, P.R. Harasti, R.D. Yates; R. Littleton, M.S. Pritchard, J.M. Fischer, E.J. Fischer, W.J. Kohri, J.R. Vetter, S. Richman, D.B. Baranowski, M.J. Anderson, E. Fletcher, D.W. Lando (2012), Radar observations of individual rain drops in the free atmosphere, Proceedings of the National Academy of Science (PNAS), 109 (24), 9293-9298, doi: 10.1073/pnas.1117776109.

52. Schneider U., A. Becker, P. Finger, A. Meyer-Christoffer, M. Ziese, B. Rudolf (2014), GPCC's new land surface precipitation climatology based on quality-controlled in situ data and its role in quantifying the global water cycle, Theoretical and applied climatology, 115 (1-2), 15-40, doi: 10.1007/s00704-013-0860-x.

53. Schumpeter, J. A. "The theory of economic development: An inquiry into profits, capital, credit, interest and the business cycle". (Vol. 55), Transaction publishers, 1934.

54. Sene, K. (2013). Precipitation Measurement. In K. Sene, Flash Floods: Forecasting and Warning (p. 33-70). Springer Netherlands. doi:10.1007/978-94-007-5164-4.

55. Seo H. J., Chatterjee P., Takeda H., "A comparison of some state of the art image denoising methods". In Conference Record of the Forty-First Asilomar Conference on Signals, Systems and Computers, 2007, ACSSC 2007, pp. 518-522.

56. Sevruk, B., & Klemm, S. (1989). Catalogue of national standard precipitation gauges. Instrument and observing methods report, 39.

57. Smith, J. A. and W. F. Krajewski. "A modeling study of rainfall rate-reflectivity relationships". In: Water Resour. Res. 29.8 (1993), pp. 2505-2514.

58. Stauffer, C., & Grimson, W. (1999). Adaptive background mixture models for real-time tracking. Computer Society Proceedings IEEE Conference on Computer Vision and Pattern Recognition. 2, p. 246-252. Fort Collins, CO: IEEE. doi:10.1109/CVPR.1999.784637.

59. Strangeways, I. (2010). A history of rain gauges. Weather, 65(5), 133-138. doi:10.1002/wea.548.

60. Sundmaeker H., Verdouw C.N., Wolfert S., Freire L.P. "Internet of Food and Farm 2020". 2016.

61. Tapiador F. J., R. Checa and M. de Castro (2010), An experiment to measure the spatial variability of rain drop size distribution using sixteen laser disdrometers, Geophysical Research Letters, 37, L16803, doi:10.1029/2010GL044120.

62. Testik F.Y., A.P. Barros and L.F. Bliven (2011), Toward a Physical Characterization of Raindrop Collision Outcome Regimes, Journal of the Atmospheric Sciences, 68, 1097-1113, doi: 10.1175/2010JAS3706.1.

63. Tokay, A. and D. A. Short. "Evidence from tropical raindrop spectra of the origin of rain from stratiform versus convective clouds". In: J. Appl. Meteorol. 35.3 (1996), pp. 355–371.

64. UK Environment Agency. (2004). Evaluation of tipping bucket rain gauge performance and data quality.

65. Ulbrich C.W. (1983), Natural variations in the analytical form of the raindrop size distribution, Journal of Climate and Applied Meteorology, 22 (10), 1764-1775.

66. Upton, G., Brawn, D. "An investigation of factors affecting the accuracy of Thies disdrometers". In Proceedings of World Meterological Organization Technical Conference on Instruments and Methods of Observation (TECO-2008), St. Petersburg, Russian Federation, 27–29 November 2008; pp. 27–29.

67. Van Djik A.I.J.M, Bruijnzeel, L.A. and Rosewell, C.J. (2002), Rainfall intensity-kinetic energy relationships: a critical literature appraisal, Journal of Hydrology, 261 (1-4), 1-23, doi: 10.1016/S0022-1694(02)00020-3.

68. Villermaux E. and B. Bossa (2009), Single-drop fragmentation determines size distribution of raindrops, Nature Physics, 5 (9), 697-70, doi: 10.1038/NPHYS1340.

69. Villermaux, E., & Eloi, F. (2011). The distribution of raindrops speeds. Geophysical Research Letters, 38(19), L19805. doi:10.1029/2011GL04886.

70. World Meteorological Organization. "Operational Measurement Uncertainty Requirements and Instrument Performance". Annex 1.D of Chapter 1, Part I. Measurement of Meteorological Variables, (2008) I.1-35.

71. www.ericsson.com/mobility-report

72. Zivkovic, Z., & van der Heijden, F. (2006). Efficient adaptive density estimation per image pixel for the task of background subtraction. Pattern Recognition Letters, 27, 773-780. doi:10.1016/j.patrec.2005.11.005.

Appendix A

Table A.1 - Camera parameters for picture acquisition (focal length f, F-number, exposure time te, focus distance z0, sampled volume V). Each row in the table refers to a one-minute time interval, i.e. to 30 pictures. For each interval reported are: the average brightness over the 30 images, the rain rate measured by the tipping bucket rain gauge (rr_g), the optimal rain rate estimate obtained with our image processing algorithm ($rr_{IRR,opt}$), the best performing brightness threshold over the interval ($S_{1,opt}$) and the rain rate estimate for the best global threshold ($rr_{IRR,S1=5}$). Grey rows indicate the best performing sample to which Figure 3.11 refers. The sensor height of the camera is h = 14.9 mm and the image height is H_P = 3456 pixels

| Event | Interval | Parameters | | | | | Avg brightness | rr_g [mm] | $rr_{IRR,opt}$ [mm] | $S_{1,opt}$ | $rr_{IRR,S1=5}$ [mm] |
		f [mm]	F-number	t_e [s]	z_0 [m]	V [m^3]					
04/11/2014	1	55	5.6	1/160	1.5	0.9	69.9	14.0	3.0	3	0.5
	2	55	5.6	1/160	1.5	0.9	72.1	14.0	3.6	3	1.1
	3	55	5.6	1/160	1.5	0.9	92.7	9.8	9.3	3	2.9
	4	55	5.6	1/160	1.5	0.9	111.9	7.8	8.2	4	4.3
	5	55	5.6	1/160	1.5	0.9	119.3	7.8	8.6	4	5.1
	6	55	5.6	1/200	1.5	0.9	109.7	7.2	8.0	4	4.9
	7	55	5.6	1/200	1.5	0.9	100.3	4.5	4.5	6	6.6
	8	55	5.6	1/200	1.5	0.9	85.0	4.5	4.4	6	6.4
	9	55	5.6	1/250	1.5	0.9	69.5	6.3	4.0	4	1.7

	10	55	5.6	1/250	1.5	0.9	71.6	6.3	3.8	4	1.5
	11	55	5.6	1/250	1.5	0.9	64.5	4.5	4.4	3	0.5
	12	55	6.3	1/160	1.5	0.9	51.3	7.3	4.0	3	1.4
	13	55	6.3	1/160	1.5	0.9	54.9	6.8	3.4	3	0.6
	14	55	6.3	1/160	1.5	0.9	64.0	13.2	3.1	3	1.4
	15	55	6.3	1/200	1.5	0.9	59.1	4.3	3.6	5	3.6
	16	55	6.3	1/200	1.5	0.9	60.2	7.8	6.6	3	3.8
	17	55	6.3	1/200	1.5	0.9	65.0	8.5	4.2	3	2.3
	18	55	6.3	1/250	1.5	0.9	67.1	6.7	3.6	3	1.7
	19	55	6.3	1/250	1.5	0.9	81.9	4.0	4.0	3	2.7
	20	55	6.3	1/250	1.5	0.9	82.7	4.0	4.1	3	2.4
	21	55	6.3	1/250	1.5	0.9	78.9	3.3	3.1	4	2.5
	22	55	7.1	1/160	1.5	0.9	57.0	3.2	1.2	3	0.3
	23	55	7.1	1/160	1.5	0.9	53.9	3.2	1.7	3	0.5
	24	55	7.1	1/160	1.5	0.9	53.3	3.2	1.1	3	0.1
	25	55	7.1	1/200	1.5	0.9	45.0	3.2	1.7	3	0.7
	26	55	7.1	1/200	1.5	0.9	46.1	2.5	1.9	3	0.4
	27	55	7.1	1/200	1.5	0.9	47.6	2.5	1.1	3	0.5
	28	55	7.1	1/250	1.5	0.9	38.8	2.3	1.8	3	0.5
	29	55	7.1	1/250	1.5	0.9	37.6	5.2	1.5	3	0.4
	30	55	7.1	1/250	1.5	0.9	35.7	5.2	1.0	3	0.2
	31	55	5.6	1/160	2	2.1	79.0	3.3	1.8	3	0.3
	32	55	5.6	1/160	2	2.1	80.1	3.3	2.7	3	0.6
	33	55	5.6	1/160	2	2.1	81.5	3.3	2.5	3	0.8
	34	55	5.6	1/200	2	2.1	62.4	3.0	2.6	3	0.5
	35	55	5.6	1/200	2	2.1	63.2	2.3	3.0	3	0.6
	36	55	5.6	1/200	2	2.1	63.1	2.3	2.8	3	0.6
	37	55	5.6	1/250	2	2.1	92.8	4.8	5.3	5	5.3
	38	55	5.6	1/250	2	2.1	92.7	4.8	4.1	6	5.8
	39	55	5.6	1/250	2	2.1	92.4	6.2	6.3	4	4.7
11/11/2014	40	55	6.3	1/160	2	2.1	114.1	4.2	4.4	5	4.4
	41	55	6.3	1/160	2	2.1	115.5	4.2	3.9	6	5.3
	42	55	6.3	1/160	2	2.1	117.2	7.0	6.5	4	4.5
	43	55	6.3	1/200	2	2.1	106.2	6.8	7.0	4	5.2
	44	55	6.3	1/200	2	2.1	107.4	4.0	4.1	5	4.1

	45	55	6.3	1/200	2	2.1	108.1	3.0	2.7	7	5.2
	46	55	6.3	1/250	2	2.1	94.6	2.8	2.8	8	5.0
	47	55	6.3	1/250	2	2.1	94.5	4.0	3.5	6	4.8
	48	55	6.3	1/250	2	2.1	93.4	4.0	3.8	4	2.9
	49	55	7.1	1/160	2	2.1	111.5	2.8	3.1	4	2.2
	50	55	7.1	1/160	2	2.1	113.0	2.3	2.9	4	1.7
	51	55	7.1	1/160	2	2.1	114.9	1.8	1.9	5	1.9
17/11/2014	52	55	7.1	1/200	2	2.1	40.6	2.5	2.0	3	0.3
	53	55	7.1	1/200	2	2.1	41.2	6.0	0.5	3	0.0
	54	55	7.1	1/200	2	2.1	41.1	6.0	0.5	3	0.0
	55	55	7.1	1/250	2	2.1	31.4	3.8	0.8	3	0.1
	56	55	7.1	1/250	2	2.1	30.7	2.7	0.5	3	0.0
	57	55	7.1	1/250	2	2.1	29.9	2.7	0.7	3	0.1
	58	55	5.6	1/160	1.5	0.9	108.5	3.0	2.5	3	1.1
	59	55	5.6	1/160	1.5	0.9	117.9	3.0	3.4	4	2.2
	60	55	5.6	1/160	1.5	0.9	119.5	3.0	2.4	4	2.0
	61	55	5.6	1/200	1.5	0.9	106.2	2.3	2.0	4	1.9
	62	55	5.6	1/200	1.5	0.9	106.4	2.3	2.3	4	1.7
	63	55	5.6	1/200	1.5	0.9	107.7	2.0	2.1	4	1.4
	64	55	5.6	1/250	1.5	0.9	97.9	2.0	1.6	4	1.0
	65	55	5.6	1/250	1.5	0.9	99.9	2.0	1.9	4	1.7
	66	55	5.6	1/250	1.5	0.9	103.6	2.0	1.8	3	1.2
	67	55	6.3	1/160	1.5	0.9	128.7	1.8	2.2	3	0.7
	68	55	6.3	1/160	1.5	0.9	127.4	1.5	1.2	3	0.4
	69	55	6.3	1/160	1.5	0.9	121.4	1.3	1.0	3	0.2
01/12/2014	70	55	5.6	1/200	2	2.1	120.7	5.5	3.6	3	0.6
	71	55	5.6	1/200	2	2.1	119.8	4.3	3.3	4	1.8
	72	55	5.6	1/200	2	2.1	120.9	4.3	4.7	5	4.7
	73	55	5.6	1/200	2	2.1	119.7	3.2	3.3	7	6.9
	74	55	5.6	1/200	2	2.1	116.9	5.0	4.3	6	6.5
	75	55	5.6	1/160	2	2.1	132.3	5.0	5.4	6	6.9
	76	55	5.6	1/160	2	2.1	131.2	6.0	5.4	6	6.6
	77	55	5.6	1/160	2	2.1	131.1	6.0	5.0	5	5.0
	78	55	5.6	1/160	2	2.1	133.1	6.0	5.2	6	7.3
	79	55	5.6	1/160	2	2.1	135.7	7.2	7.0	4	4.9

80	55	6.3	1/160	2	2.1	135.2	7.2	6.0	5	6.0
81	55	6.3	1/160	2	2.1	133.8	9.2	11.7	3	4.4
82	55	6.3	1/200	2	2.1	117.1	7.8	9.1	3	4.8
83	55	6.3	1/200	2	2.1	114.7	7.8	7.3	3	3.5
84	55	6.3	1/200	2	2.1	114.8	5.2	6.1	3	2.4
85	55	6.3	1/200	2	2.1	117.7	4.5	4.0	5	4.0
86	55	5.6	1/250	2	2.1	113.8	4.5	4.2	6	4.9
87	55	5.6	1/250	2	2.1	117.0	4.0	3.4	8	8.8
88	55	5.6	1/250	2	2.1	115.9	5.0	5.6	6	8.0
89	55	5.6	1/160	2	2.1	119.7	17.3	15.9	4	10.5
90	55	5.6	1/160	2	2.1	125.4	13.8	12.0	6	16.3
91	55	5.6	1/160	2	2.1	129.0	21.2	23.9	5	23.9
92	55	5.6	1/160	2	2.1	128.8	30.2	27.9	4	22.3
93	55	5.6	1/200	2	2.1	106.7	38.2	35.4	3	20.1
94	55	5.6	1/200	2	2.1	105.9	27.7	29.9	3	14.1
95	55	5.6	1/200	2	2.1	101.1	17.3	16.4	3	6.4
96	55	5.6	1/250	2	2.1	77.6	15.7	11.3	3	3.1
97	55	5.6	1/250	2	2.1	64.7	6.3	4.6	4	1.9
98	55	5.6	1/250	2	2.1	75.2	3.8	5.0	4	2.6
99	55	6.3	1/160	2	2.1	110.9	3.8	3.4	5	3.4
100	55	6.3	1/160	2	2.1	115.6	5.3	3.8	4	1.9
101	55	6.3	1/160	2	2.1	121.7	5.3	6.0	4	3.4
102	55	6.3	1/200	2	2.1	108.1	4.7	4.4	6	7.0
103	55	6.3	1/200	2	2.1	103.3	3.2	3.6	4	1.6
104	55	6.3	1/200	2	2.1	100.6	3.2	2.4	3	0.6